OCO D-65488

OCO (Orbiting Carbon Observatory) - 2

Level 2 Full Physics Retrieval Algorithm Theoretical Basis

Version 1.0 Rev 4
November 10, 2010

National Aeronautics and
Space Administration

JPL

Jet Propulsion Laboratory
California Institute of Technology
Pasadena, California

ORBITING CARBON OBSERVATORY (OCO) -2

LEVEL 2 FULL PHYSICS ALGORITHM

Theoretical Basis Document

David Crisp	Jet Propulsion Laboratory
Hartmut Boesch	University of Leicester
Linda Brown	Jet Propulsion Laboratory
Rebecca Castano	Jet Propulsion Laboratory
Mathew Christi	Colorado State University
Brian Connor	BC Consulting Limited
Christian Frankenberg	Jet Propulsion Laboratory
James McDuffie	Jet Propulsion Laboratory
Charles Miller	Jet Propulsion Laboratory
Vijay Natraj	Jet Propulsion Laboratory
Chris O'Dell	Colorado State University
Denis O'Brien	Colorado State University
Igor Polonski	Colorado State University
Fabiano Oyafuso	Jet Propulsion Laboratory
David Thompson	Jet Propulsion Laboratory
Geoff Toon	Jet Propulsion Laboratory
Rob Spurr	RT Solutions Inc.

Approved by:

Version 1.0
November 10, 2010

Jet Propulsion Laboratory
California Institute of Technology
Pasadena, California

Document History:

Version	Revision	Date	Description/Comments
1.0	1		Initial Version of OCO ATBD
1.0	2	4/18/2009	Final Version of OCO ATBD
1.0	3	10/15/2010	First Version of OCO-2 ATBD
1.0	4	11/10/2010	Final pre-external review version, minor fixes

The research described in this document was carried out at the Jet Propulsion Laboratory, California Institute of Technology, under a contract with the National Aeronautics and Space Administration.

TABLE OF CONTENTS

LIST OF FIGURES

LIST OF TABLES

1. Introduction

1.1 Purpose

This Algorithm Theoretical Basis (ATB) document describes the algorithm used to retrieve the column averaged dry air mole fraction, X_{CO2}, and other quantities included in the Level 2 Product from the spectra collected by OCO-2. In particular, this document identifies sources of input data, which are required for retrievals; provides the physical theory and mathematical background underlying the use of this information in the retrievals; includes implementation details; and describes assumptions and limitations of the adopted approach.

1.2 Scope

This document covers the algorithm theoretical basis for the parameters of the Full Physics Product that are to be routinely retrieved at the OCO-2 Science Data Operations System. Specialized products or parameters are not discussed. Section 1 describes the purpose and scope of the document. Section 2 provides a brief overview of the mission and instrument. The processing concept and algorithm description are presented in Section 3. References for publications cited in the text are given in Section 4.

2. Experiment Overview

2.1 Objectives

The Orbiting Carbon Observatory (OCO) is the first National Aeronautics and Space Administration (NASA) mission designed to collect space-based measurements of atmospheric carbon dioxide (CO_2) with the precision, resolution, and coverage needed to characterize the processes controlling its buildup in the atmosphere [Crisp et al. 2004; 2007]**.** After a launch mishap, which prevented the original OCO mission from reaching orbit, the Orbiting Carbon Observatory-2 (OCO-2) mission was formulated to meet the original OCO objectives.

Fossil fuel combustion and other human activities are now emitting more than 30 billion tons of carbon dioxide (CO_2) into the atmosphere every year. Atmospheric CO_2 measurements currently being collected by a global network of surface stations indicate that less than half of the CO_2 is accumulating in the atmosphere. The remainder is apparently being absorbed by CO_2 "sinks" in the ocean and the terrestrial biosphere [c.f. Canadell et al. 2007]. While the existing surface greenhouse gas monitoring network has expanded continuously over the past 50 years and now provides the accuracy and coverage needed to quantify the abundance of this gas on global scales, it still lacks the spatial and temporal resolution and coverage needed to identify and quantify CO_2 sources and sinks on regional scales or to quantify emissions from discrete point sources.

One way to improve the coverage and resolution of these measurements is to collect spatially-resolved, global measurements of the column-averaged CO_2 dry air mole fraction, X_{CO2}, from space [Rayner and O'Brien, 2001]. Although natural processes and human emissions can change the atmospheric CO_2 mixing ratio by as much as 8% near the surface (>30 ppm out of the ~385 ppm background), the amplitude of these variations decreases rapidly with altitude, such that X_{CO2} variations rarely exceed 2% (8 ppm) on regional to global scales. East-west variations are typically no larger than 0.3 to 0.5%. Because of this, modeling studies show that space based measurements of X_{CO2} can substantially improve our understanding of surface fluxes only if they have the accuracy, precision, coverage, spatial resolution, and temporal sampling needed to describe X_{CO2} variations with amplitudes no larger than 0.3 to 0.5 % (1 to 2 ppm) on scales ranging from < 100 km over continents, to ~1000 km over the ocean [Rayner and O'Brien, 2001].

Systematic biases with amplitudes larger than 0.3% on spatial scales of 100 to 1000 km will introduce spurious X_{CO2} gradients that would be indistinguishable from those produced by true CO_2 sources or sinks. Absolute X_{CO2} accuracies better than 0.3% on these scales are therefore essential for retrieving CO_2 fluxes. Truly global biases are less of a concern because they will not introduce spurious X_{CO2} gradients. However, such biases could compromise validation of the space based measurements against other standards, such as the World Meteorological Organization (WMO) standard for atmospheric CO_2.

Space based measurements of X_{CO2} are likely to make their most significant contributions to our understanding of the carbon cycle over the ocean and over tropical land masses, because these regions are poorly sampled by the existing ground-based network. X_{CO2} estimates over the ocean are needed to quantify their large natural CO_2 sources and sinks and to facilitate the tracking of CO_2 emissions transported over the ocean by the prevailing winds. X_{CO2} measurements must also be collected over nearly the full range of latitudes on the sunlit hemisphere to avoid uncertainties introduced by the transport of air in and out of the field of regard.

To resolve CO_2 fluxes on spatial scales ranging from <100 to ~1000 km, data must be collected at higher resolution to discriminate natural sinks from nearby sources. A small sampling footprint also helps to ensure that some cloud-free soundings can be obtained even in partially cloudy regions, since the probability of measuring a cloud free scene is inversely proportional to footprint size. A small sounding footprint is also needed to quantify CO_2 emissions from discrete point sources, such as individual power plants or cities because the minimum detection limit (measured in kg of CO_2) associated with a given concentration change (e.g. a 1 ppm variation in X_{CO2}) is inversely proportional to the area of the footprint.

The natural processes responsible for the uptake and release of CO_2 are driven primarily by photosynthesis and respiration on land and by the solubility of CO_2 in the ocean. The efficiency of these natural processes varies on diurnal, seasonal and interannual time scales. CO_2 emissions from human activities also vary on these time scales. Existing ground-based measurements indicate that while diurnal CO_2 variations in the vicinity of local sources and sinks can be large (>10 ppm), these variations are confined near the surface, and rarely contribute to X_{CO2} variations larger than 0.3%. While these small differences would be difficult to detect from space, X_{CO2} should be estimated from measurements acquired at the same, fixed time of day everywhere on Earth to avoid introducing a spatially varying diurnal bias. Global measurements are needed at on semi-monthly intervals over a complete annual cycle to identify changes in the natural and human contributions to atmospheric CO_2 over the seasonal cycle. More than one seasonal cycle must be observed to resolve the relative contributions of seasonal and interannual variability to the atmospheric CO_2 buildup.

2.2 Measurement Approach

To meet these objectives, OCO-2 employs a dedicated spacecraft with a single instrument that will be launched into a near-polar orbit on an expendable launch vehicle [Crisp et al., 2007]. The Observatory will fly in a loose formation with the Earth Observing System Afternoon Constellation (EOS A-Train). This 705 km altitude, sun synchronous orbit follows the World Reference System-2 (WRS-2) ground track, yielding 233 orbits over its 16-day ground track repeat cycle. The orbit's 1:30 PM mean local time is well suited for acquiring observations of the absorption of reflected sunlight by CO_2 and O_2 because the sun is high, maximizing the available signal. It also facilitates coordinated calibration and validation campaigns with other A-Train instruments, and synergistic use of OCO-2 data with that from other A-Train platforms

The OCO-2 instrument incorporates three high resolution spectrometers that make coincident measurements of reflected sunlight in the near-infrared CO_2 near 1.61 and 2.06 μm and in molecular oxygen (O_2) A-Band at 0.76 μm [Crisp et al. 2007]. Simultaneous, co-boresighted measurements from these 3 spectral regions are combined to define a single "sounding." Each sounding is analyzed with remote sensing retrieval algorithms to produce an estimate of X_{CO2} for the atmospheric path between the sun, the reflecting surface and the OCO-2 instrument. Because the dry air mole fraction of O_2 is well known and essentially constant, measurements of O_2 A-band absorption provide direct constraints on the surface pressure and uncertainties in the atmospheric optical path length introduced by cloud and aerosol scattering and pointing errors. Measurements of absorption by the weak and strong CO_2 absorption bands near 1.61 and 2.06 μm, respectively, provide information about both the CO_2 column abundance and the wavelength-dependent scattering by aerosols along the same optical path.

The OCO-2 instrument must measure CO_2 and O_2 absorption with adequate precision to yield X_{CO2} estimates with a precision better than 0.3% on spatial scales smaller than 100 km over continents and 1000 km over the ocean over more than 90% of range of latitudes on the on the sunlit hemisphere of the Earth. To meet these objectives, the instrument must have a high sensitivity and a high signal-to-noise ratio (SNR) over a wide dynamic range [Crisp et al. 2007; Crisp 2008]. A high spectral resolving power ($\lambda/\delta\lambda > 20{,}000$) is needed to resolve the CO_2 and O_2 lines from the adjacent continuum to maximize the sensitivity to small (<0.3%) variations in $X_{CO2.}$ Measurements across the entire O_2 or CO_2 band are needed at high SNR because a 0.3% variation in X_{CO2} must be inferred from substantially smaller variations in O_2 and CO_2 absorption strength. The retrieval algorithm must then perform a least squares fit to dozens of lines within each band to yield X_{CO2} retrievals with precisions near 0.3%. A wide dynamic range is needed because the contrast between line cores and the adjacent continuum can exceed 100:1, and because the signal level depends on the intensity of the sunlight reflected from the surface, which decreases with increasing solar zenith angle (latitude) and decreasing surface reflectance.

The OCO-2 instrument will collect 4 to 8 soundings over its 0.8-degree wide swath every 0.333 seconds, yielding surface footprints with downtrack dimensions < 2.25 km and cross-track dimensions that vary from 0.1 to 1.3 km at nadir [Crisp et al., 2007]. The high spatial resolution will facilitate the discrimination of natural sinks from nearby sources and enhance the coverage by increasing the probability of collecting some cloud free soundings even in partially cloudy conditions. The high sampling rate will provide dozens to hundreds of samples over downtrack distances that are small compared to those that characterize the spatial variability of X_{CO2} over continents (<100 km) and ocean (1000 km), even when less than 10% of samples are sufficiently cloud free to yield full-column X_{CO2} measurements. X_{CO2} estimates from these soundings can therefore be averaged to improve the precision. While the rapid downtrack sampling yields high spatial resolution along the orbit tracks; the east-west (left/right of ground track) resolution is largely determined by the distance between orbit tracks. The 98.8 minute orbit period, yields ~14.56 orbits each day that are separated by ~24.7° of longitude. The orbit track spacing decreases to ~13° after 2 days, and to 1.5°after a full 16-day repeat cycle.

To ensure their accuracy, the space based X_{CO2} estimates are validated through comparisons with near-simultaneous measurements of X_{CO2} acquired by ground-based Fourier Transform Spectrometers in the Total Carbon Column Observing Network (TCCON) [Washenfelder et al. 2006; Wunch et al. 2010]. This network currently includes over a dozen stations, distributed over a range of latitudes ranging from Lauder New Zealand to Ny Alesund, Norway, and is continuing to add new facilities. To relate TCCON measurements to the WMO CO_2 standard, aircraft observations have been collected over several stations, using in situ CO_2 measurement approaches used to define that standard. OCO-2 will target a TCCON site as often as once each day, acquiring thousands of measurements as it flies overhead. These measurements will be analyzed to reduce biases below 0.1% (0.3 ppm) at these sites. The space-based X_{CO2} estimates will be further validated through comparisons with CO_2 and surface pressure measurements from ground based sites with the aid of data assimilation models to provide a more complete global assessment of measurement accuracy.

2.3 Instrument Characteristics

The Observatory carries and points a single instrument that incorporates three, co-boresighted, long-slit, imaging grating spectrometers optimized for the O_2 A-band at 0.765 µm and the CO_2 bands at 1.61 and 2.06 µm (Figure 2-1) [Crisp et al. 2007; Crisp 2008]. The instrument mass is ~140 kg, and its average power consumption is ~100 Watts. The 3 spectrometers use similar optical designs and are integrated into a common structure to improve system rigidity and thermal stability. They share a common housing and a common F/1.8 Cassegrain telescope. The light path is illustrated in Figure 2-1. Light entering the telescope is focused at a field stop and then recollimated before entering a relay optics assembly. There, it is directed to one of the three spectrometers by a dichroic beam splitter, and then transmitted through a narrowband pre-disperser filter. The pre-disperser filter for each spectral range transmits light with wavelengths within ~±1% of the central wavelength of the CO_2 or O_2 band of interest and rejects the rest. The light is then refocused on the spectrometer slits by a reverse Newtonian telescope. Each spectrometer slit is ~3 mm long and ~25 µm wide. These long, narrow slits are aligned to produce co-boresighted fields of view that are ~0.0001 radians wide by ~0.0146 radians long. Because the diffraction gratings efficiently disperse light that is polarized in the direction parallel to the slit, a polarizer was included in front of the slit to reject the unwanted polarization before it enters the spectrometer, where it could contribute to the scattered light background.

Once the light enters a spectrometer slit, it is collimated by a 2-element refractive collimator, dispersed by a reflective planar holographic diffraction grating, and then focused by a 2-element camera lens on a 2-dimensional focal plane array (FPA), after traversing a second, narrowband filter. The narrowband filter just above the FPA is cooled to ~180K to reject thermal emission from the instrument.

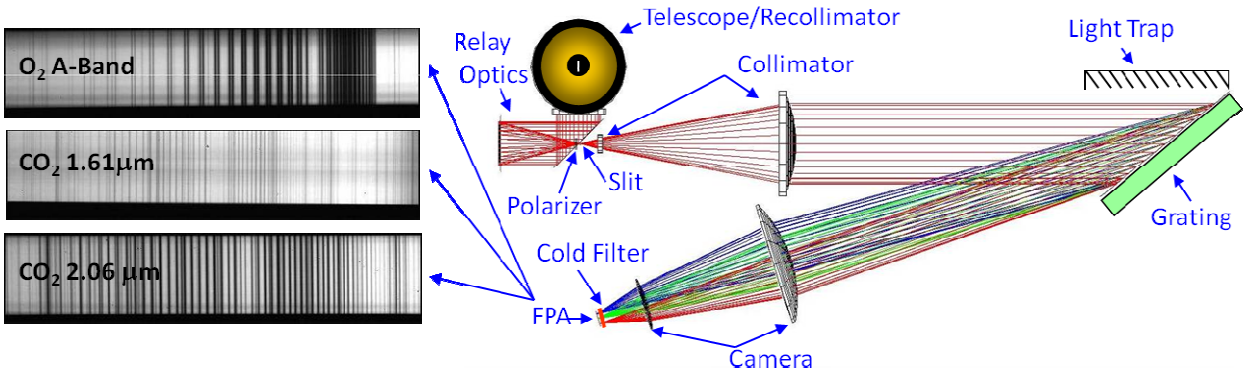

Figure 2-1 The OCO-2 instrument showing the major optical components and optical path (right) and images of spectra recorded by the FPA in the 3 spectral channels (left).

The spectral range and resolving power of each channel includes the complete molecular absorption band as well as some nearby continuum to provide constraints on the optical properties of the surface and aerosols as well as absorbing gases. To meet these requirements, the O_2 A-band channel covers 0.758 to 0.772 µm with a resolving power of >17,000, while the 1.61 and 2.06 µm CO_2 channel cover 1.594 to 1.619 µm and 2.042 to 2.082 µm, respectively with a resolving power > 20,000 [Crisp et al. 2007; Crisp 2008].

The gratings disperse the light onto the FPAs in the direction orthogonal to the long dimension of the slit (Figure 2-2). The field of view is resolved spatially along the slit. The FPAs are 1024 x

1024 pixel arrays with 18 µm by 18 µm pixels that have a 100% fill factor (i.e. there are no spatial or spectral gaps between the pixels). The slit is imaged on the FPA, which samples its full-width at half maximum (FWHM) with 2 to 3 pixels. The quantum efficiency of the FPA's is between 75 and 90%, and the read noise is < 20 electrons/pixel/exposure. The FPA temperatures are maintained at <120 K by a pulse-tube cryocooler that is thermally coupled to an external radiator though variable conductance heat pipes. At this temperature, thermal noise from the FPA's is negligible during the short exposure time (0.333 seconds) . The optical bench is maintained at -5° C by a thermal radiative shroud that is coupled to an external radiator by variable conductance heat pipes.

The spectrum produced by each channel is dispersed to illuminate all 1024 pixels in spectral dimension on each FPA. The length of the slit limits spatial field of view to only ~190 pixels in the spatial dimension (Figure 2-2a). OCO-2 soundings use an along-slit field of view is defined by ~160 of these 190 pixels. In normal science operations, the FPA's are continuously read out at 3 Hz. To reduce the downlink data rate and increase the SNR, 20 adjacent pixels in the FPA dimension parallel to the slit (ie. the "Spatial Direction" in Figure 2-2a) are summed on board to produce up to 8 spatially-averaged spectra (Figure 2-2b). The along-slit angular field of view of each of these spatially-averaged "super-pixels: is ~1.8 mrad (0.1° or ~1.3 km at nadir from a 705 km orbit). The angular width of the narrow dimension of the slit is only 0.14 mrad, but the telescope focus was purposely softened to increase the effective full width at half maximum of each slit to ~0.6 mrad to simplify the boresight alignment among the 3 spectrometer slits.

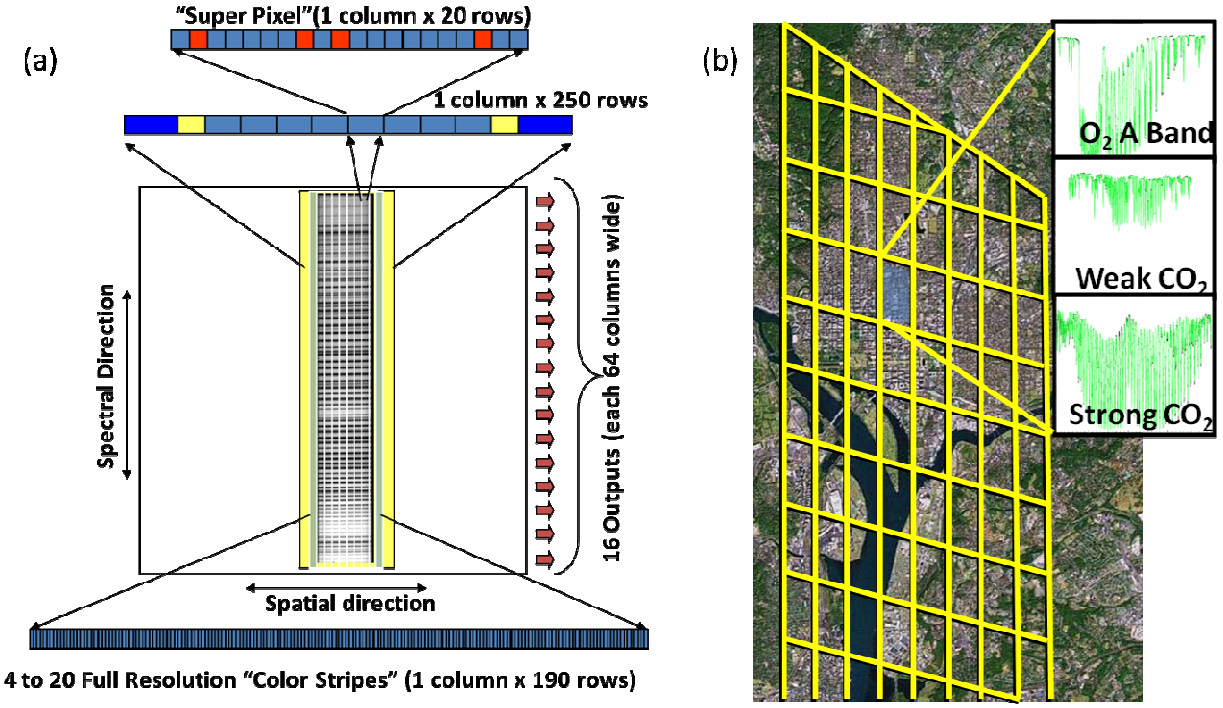

Figure 2-2. (a) The illumination and readout scheme used for the OCO-2 Focal Plain Arrays. (b) Spatial layout of 8 cross-track footprints for nadir observations over Washington DC.

In addition to the 8 spatially-binned, 1024-element spectra, each spectrometer also returns 4 to 20 spectral samples without on-board spatial binning to provide the full along-slit spatial resolution. Each of these full-resolution "color stripes" covers a 220 pixel wide region of the

FPA that includes the full length of the slit (190 pixels) as well as a few pixels beyond the ends of the slit (Figure 2-2). These full-spatial-resolution color stripes are used to detect spatial variability within each of the spatially summed super pixels and to monitor the thermal emission and scattered light within the instrument.

2.3.1 Observing Modes

The spacecraft bus orients the instrument to collect science observations in Nadir, Glint, and Target modes (Figure 2-3) [Crisp et al. 2007; Crisp 2008]. In Nadir mode, the satellite points the instrument aperture to the local nadir, so that data can be collected along the ground track just below the spacecraft. In Glint mode, the ACS is programmed to point the instrument aperture toward the bright "glint" spot. In Target mode, the ACS points the instrument's aperture at specific stationary surface targets as the satellite flies overhead. To ensure that the target is not missed, the ACS superimposes a small amplitude sinusoidal oscillation (±0.23° about the spacecraft y axis) in the direction perpendicular to the long dimension of the spectrometer slit, to scan the slits over a region centered on the nominal target location Figure 2-3 (c). This "Target scan", combined with the instruments 0.8° wide field of view, creates a 0.46° by 0.8° viewing box around the target. The period of this sinusoidal oscillation will be less than 24 seconds, such that the slit is scanned over the target >20 times in a 9-minute Target observation.

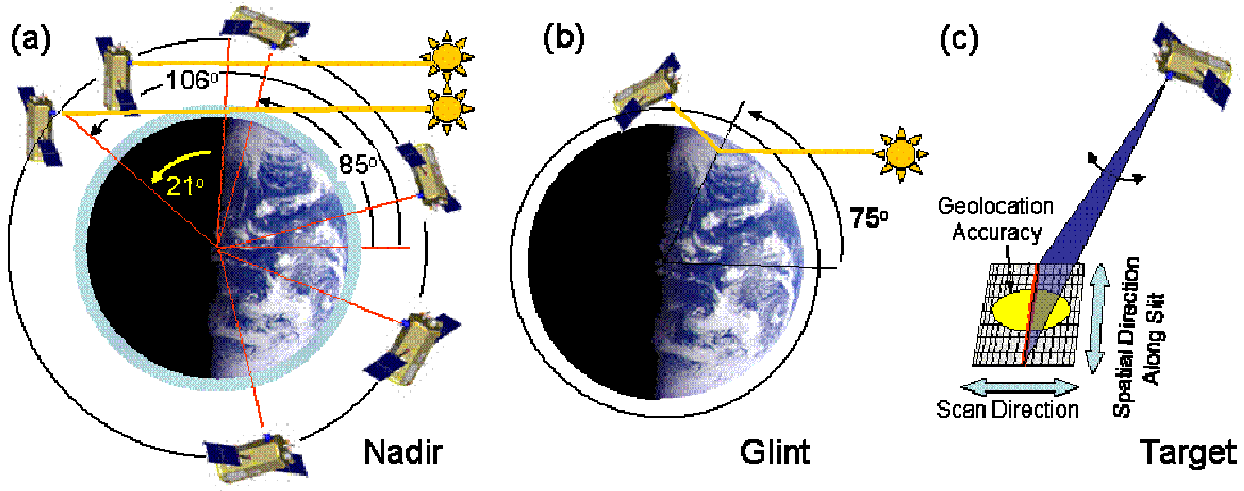

Figure 2-3. Nadir, Glint, and Target observations. (a) Nadir observations are acquired over the sunlit hemisphere at latitudes where the surface solar zenith angle is <85°. On all orbits except downlink orbits, as the Observatory passes over the northern terminator, it pitches up to point the instrument aperture at the sun for solar radiometric calibrations. (b) Glint observations are made at latitudes on the sunlight hemisphere where the solar zenith angle is less than 75°. (c) For Target observations, the spacecraft points the instrument at a stationary surface target as it flies over. A small-amplitude sinusoidal oscillation in the pitch axis is superimposed on the nominal pointing to scan the spectrometer slit across the Target.

For Nadir and Glint observations, the ACS is required to point the instrument's field of view to within 0.25° of its intended target (3 km at nadir). For Target observations, a pointing accuracy of 0.3° is required. OCO-2 will switch from Nadir to Glint observations on alternate 16-day global ground-track repeat cycles so that the entire OCO-2 ground track is mapped in each mode every 32 days. Comparisons between Nadir and Glint observations will provide opportunities to

identify and correct for biases introduced by the viewing geometry. Target observation will be acquired over an OCO-2 validation site roughly once each day.

The same data sampling rate is used for Nadir, Glint, and Target observations. While the instrument is capable of collecting up to 8 adjacent, spatially resolved samples every 0.333 seconds (24 samples per second), the nominal data transmission and ground processing approach has been sized to accommodate only 12 samples per second as a cost saving measure. At this data collection rate, the Observatory collects ~200 soundings per degree of latitude as it travels from pole to pole, or ~7 million soundings over the sunlit hemisphere every 16 day ground repeat cycle. The data collection rate can be increased to 24 samples/seconds at any time during the mission if there are adequate resources. Clouds, aerosols, and other factors will reduce the number of soundings available for X_{CO2} retrievals, but the small sounding foortprint ensures that some data will be sufficiently cloud free on regional scales at monthly intervals.

Nadir observations will be collected at all locations where the surface solar zenith angle is less than 85°. This mode provides the highest spatial resolution and is expected to return more usable soundings in regions that are partially cloudy or have significant surface topography. However, Nadir observations are expected to have limited SNR's over dark ocean- or ice-covered surfaces at high latitudes. Glint observations are expected to provide much greater SNR over these surfaces. Glint soundings will be collected at all latitudes where the surface solar zenith angle is less than 75°. Target observations will be conducted over OCO-2 validation sites that are within 61° of the local spacecraft nadir along the orbit track and spacecraft viewing angles between 30° west of the ground track and 5° east of the ground track. When the target is near the ground track, a single pass can last for up to 9 minutes, providing 6000 to 12000 soundings in the vicinity of the target. This large number of soundings reduces the impact of random errors and provides opportunities to identify spatial variability in the X_{CO2} field near the target.

While the sunlight incident at the top of the Earth's atmosphere is unpolarized, both reflection from the surface and scattering by the atmosphere can affect the polarization of the radiation field measured by the OCO-2 instrument. These processes act primarily to reduce the intensity of the radiation that is polarized in the direction parallel to the Principal Plane. Polarization has a much smaller effect on the intensity polarized in the direction perpendicular to the Principal Plane. As noted above, the OCO-2 instrument is only sensitive to light polarized in the direction parallel to the orientation of the long axis of the spectrometer slits. The Nadir and Glint observing strategies have therefore been designed such that the long axis of the spectrometer slits (which are roughly parallel to the Observatory y-axis) remains oriented perpendicular to Principal Plane to maximize signal and minimize polarization errors (Figure 2-4 (a)). As the Observatory ascends over the southern terminator, its x-axis is pointed north-northwest along the orbit track and the spectrometer slits are oriented almost perpendicular to the orbit track (Figure 2-4 (b)). In this orientation, the instrument collects data in a conventional push-broom fashion, where the footprint is determined by the cross-track instantaneous field of view (0.1°) and the integration time (0.333 seconds). For Nadir observations, this yields 4 to 8 cross-track footprints along the spectrometer slit with dimensions of 1.29 km by 2.25 km.

As the Observatory proceeds northward along its orbit, it rotates counterclockwise about its z axis, such that the x-axis points westward, and the long axis of the spectrometer slits are aligned with the track just north of the sub-solar latitude. At this point, each spatially-resolved surface footprint is determined by the projected width of the slit (<0.03°) and the exposure time. For

Nadir observations at the sub-solar latitude, each of the footprints is ~0.4 km by 2.25 km and there is spatial overlap between footprints acquired in successive exposures by the spatial elements along the slit. The Principal Plane azimuth rotation continues as the Observatory approaches the northern terminator, where the x-axis is pointing southwest, along the orbit track, and the spectrometer slit is once again almost perpendicular to the orbit track.

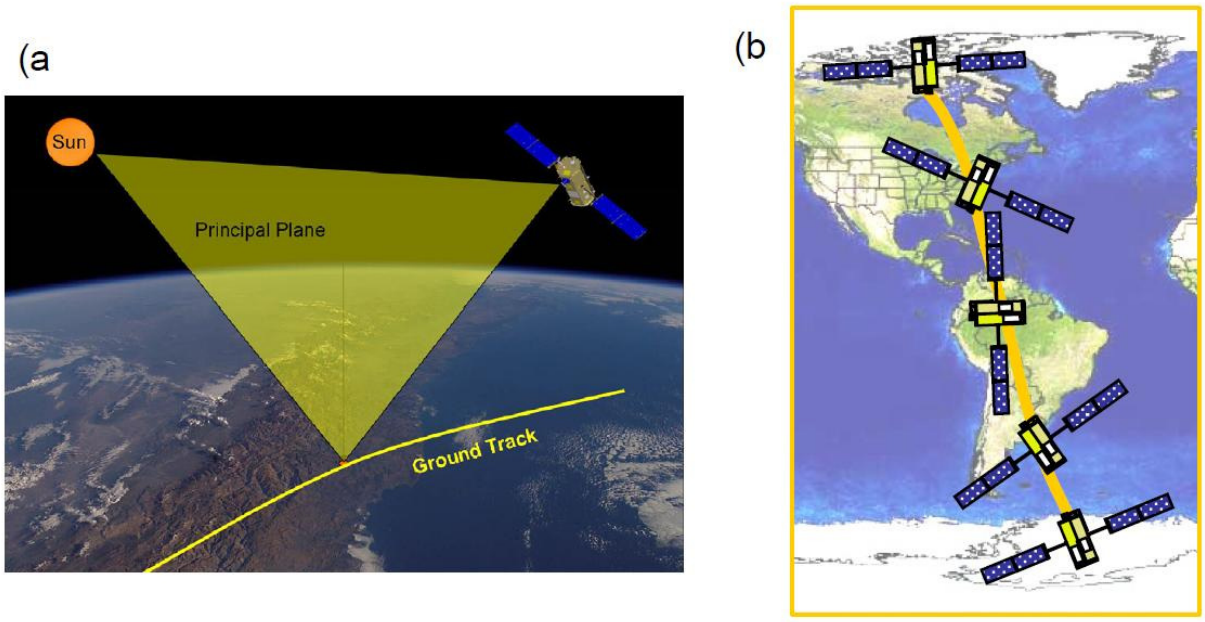

Figure 2-4. (a) The Principal Plane is defined with respect to the sun, surface footprint and spacecraft. (b) The spacecraft azimuth changes during the orbit to maintain the alignment of the spectrometer slits (which are roughly parallel with the axis of the solar panels) perpendicular to the Principal Plane [Crisp et al 2007].

2.3.2 Data Product Delivery

Science and housekeeping data are transmitted to a NASA Near Earth Network station in Alaska once each day. The data are then transferred to the Earth Science Mission Operations (ESMO) center at the NASA Goddard Space Flight Center (GSFC) where the raw telemetry is converted to time-ordered raw radiance spectra (Level 0 Products). This product is then delivered to the OCO-2 Science Data Operations System (SDOS) at the NASA Jet Propulsion Laboratory, where full orbits are first processed to yield radiometrically calibrated, geolocated spectral radiances within the O_2 and CO_2 bands (Level 1 Products). The bore-sighted spectra for each coincident CO_2 / O_2 sounding are then processed to estimate the column averaged CO_2 dry air mole fraction, X_{CO2} (Level 2 Products). Other Level 2 data products to be retrieved from each sounding include the surface pressure, surface-weighted estimates of the column-averaged water vapor and atmospheric temperature, the vertical distribution and optical depth of optically-thin clouds and aerosols, the CO_2 column averaging kernels, and a number of diagnostic products.

3. Algorithm Description

3.1 Algorithm Overview

The primary purpose of the retrieval algorithm is to derive estimates of the column averaged atmospheric CO_2 dry air mole fraction, X_{CO2}, and other Level 2 data products from the spectra returned by the OCO-2 mission. X_{CO2} is defined as the ratio of the column abundances of CO_2 and the column abundance of dry air:

$$X_{CO2} = \int_0^\infty N_{CO2}(z)\, dz \;/\; \int_0^\infty N_{air}(z)\, dz\,. \tag{3-1}$$

Here, $N_{CO2}(z)$ is the altitude (z) dependent number density of CO_2 (e.g. number of CO_2 molecules per cubic meter) and $N_{air}(z)$ is the altitude dependent number density of dry air. Because O_2 constitutes 0.20955 N_{air}, X_{CO2} can also be expressed as:

$$X_{CO2} = 0.20955 \int_0^\infty N_{CO2}(z)\, dz \;/\; \int_0^\infty N_{O2}(z)\, dz\,. \tag{3-2}$$

The number densities of CO_2 and O_2 can be inferred from precise, spectroscopic observations of reflected sunlight because the measured intensity of the sunlight at wavelengths where these gases absorb is proportional to the total number of molecules along the optical path, S:

$$I(\lambda, \theta, \theta_o, \varphi\text{-}\varphi_o) = F_o(\lambda) \cos\theta_o R(\lambda, \theta, \theta_o, \varphi\text{-}\varphi_o) < \exp\{-\int_0^S \textstyle\sum_{m=1}^{M} [\sigma_m(\lambda,s)\, N_m(s)]\, ds\} > \tag{3-3}$$

Here, $I(\lambda, \theta, \theta_o, \varphi\text{-}\varphi_o)$ is the observed intensity at wavelength, λ. θ and φ are the observation zenith and azimuth angles while θ_o, and φ_o are the corresponding solar zenith and azimuth angles. $F_o(\lambda)$ is the solar flux at the top of the atmosphere, $R(\lambda, \theta, \theta_o, \varphi\text{-}\varphi_o)$ is the reflectance of the surface, $\sigma_m(\lambda,s)$ and $N_m(s)$ are the absorption cross-section of the m^{th} absorbing constituent (CO_2, O_2, or other absorber), and the integration is performed along an optical path, S, which extends from the top of the atmosphere to the reflecting surface, and back to the spacecraft. The brackets, < >, indicate that an average over the range of possible optical paths that the photons could travel. A few of the possible optical paths are illustrated in Figure 3-1.

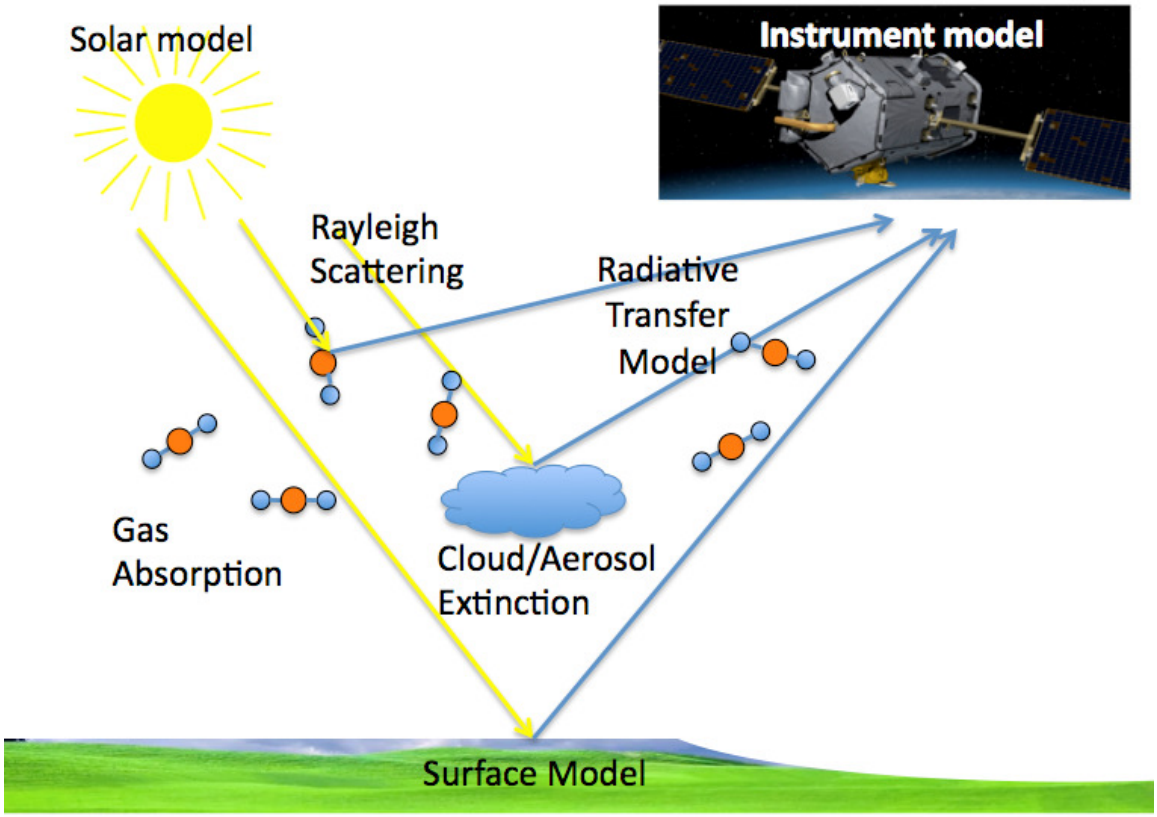

Figure 3-1. Viewing geometry and a few possible optical paths traversed by solar photons that are recorded by the instrument. This figure also illustrates the forward model components.

Because the argument of the exponential in (3-3) depends linearly on the optical cross-section per molecule, σ, and length of the optical path, S, as well as the number density of absorbing molecules, errors or uncertainties in either σ or S can introduce compensating errors and uncertainties in the retrieved number densities. For example, consider a sounding footprint that is partially obscured by a cloud, which scatters a fraction of the radiation back to the sensor before it has traversed the complete path from the top of the atmosphere to the surface and back the space. If the scattering by this cloud is neglected in the retrieval algorithm, the reduced optical path could be misinterpreted as evidence for a reduced number density of absorbing molecules. Similarly, if multiple scattering between the surface and an airborne aerosol layer produces an optical path that is longer than the direct path between the sun, surface, and spacecraft, and multiple scattering is neglected, the enhanced optical path could be misinterpreted as evidence for a large number density of absorbing molecules. Accurately estimating the atmospheric optical path is therefore a primary focus of the retrieval algorithm.

If we divide the atmosphere into a series of discrete layers where the vertical distributions of the absorbing constituents are uniform or at least spatially uncorrelated, we can rewrite the quantity:

$$\int_0^S \sum_{m=1}^{M}[\sigma_{\mathrm{m}}(\lambda,\mathrm{s})\, N_m\,(\mathrm{s})]\,\mathrm{ds} \;=\; \sum_{n=1}^{N}\;\sum_{m=1}^{M}\;\int_{s(n)}^{s(n+1)} \sigma_{\mathrm{m}}(\lambda,\mathrm{s})\, N_m\,(s)]\; ds \tag{3-4}$$

If we consider a linear path through plane-parallel layer, n, at a local zenith angle of θ, the optical path between point *s(n)* and *s(n+1)* can be approximated as $ds = dz/\cos\theta$. We can then express the quantity included in the integrand in terms of the vertical optical depth, in each layer,

$$\tau_{m,n}(\lambda,z) \;=\; \int_{s(n)}^{s(n+1)} \sigma_{\mathrm{m}}(\lambda,\mathrm{z})\, N_m\,(\mathrm{z})]\; dz\,. \tag{3-5}$$

The total, column integrated vertical optical depth can then be given as:

$$\tau(\lambda) = \;\sum_{n=1}^{N}\;\sum_{m=1}^{M}\;\int_{s(n)}^{s(n+1)} \sigma_{\mathrm{m}}(\lambda,\mathrm{z})\, N_m\,(\mathrm{z})]\; dz\,. \tag{3-6}$$

If we assume that the atmosphere is plane parallel and ignore scattering by gases and airborne particles, the intensity observed by the spacecraft for a solar zenith angle, θ_0 and observation angle, θ is given by:

$$\begin{aligned} I(\lambda,\ \theta,\ \theta_o\ \varphi\text{-}\varphi_o) = F_o(\lambda)\cos\theta_o\, R(\lambda,\theta,\ \theta_o\ \varphi\text{-}\varphi_o) \times \\ \exp\{-\ \tau(\lambda)\,(\ \cos\theta_0 + \cos\theta\ )/(\ \cos\theta_0\cos\theta\ )\ \}\,. \end{aligned} \tag{3-7}$$

In the above discussion, all of the complexity associated with scattering by gases, airborne particles, and the surface was avoided by introducing the optical path averaging operator, < > or simply ignored (as in 3-6). More generally, the observed intensity will depend on both the absorption and scattering, which can alter the optical path traversed by the solar photons. Fortunately, all of these optical processes can be accurately simulated by solving the Equation of Transfer:

$$\mu\frac{d\,\mathbf{I}(\tau,\theta,\phi)}{d\tau} = \mathbf{I}(\tau,\theta,\phi) - \mathbf{J}(\tau,\theta,\phi) \tag{3-8}$$

Where

$$\mathbf{J}(\tau,\theta,\phi) = \frac{\omega(\tau)}{4\pi}\int_{-1}^{1}\int_{0}^{2\pi}\mathbf{\Pi}(\tau,\theta,\theta',\phi-\phi')\,\mathbf{I}(\tau,\theta',\phi')d\phi' d\theta' + \mathbf{Q}(\tau,\mu,\phi) \tag{3-9}$$

Here, ω is the single scattering albedo, $\mathbf{\Pi}$ the phase matrix for scattering, and $\mu = \cos\theta$. The first term in Eq. (3-9) represents multiple scattering contributions. The inhomogeneous source term $\mathbf{Q}(\tau,\mu,\varphi)$ describing single scattering of the (attenuated) solar beam can be expressed as:

$$\mathbf{Q}(\tau,\mu,\varphi)=\frac{\omega(\tau)}{4\pi}\,\mathbf{\Pi}(\tau,\mu,-\mu_0,\phi-\phi_0)\,\mathbf{I}_0\,\exp[-\tau/\mu_O] \tag{3-10}$$

Within the context of an atmospheric remote sensing retrieval algorithm, the Equation of Transfer is a component of the "Forward Model".

Monitoring small changes in the abundances of gases such as O_2 and CO_2 using near infrared absorption poses special challenges at near infrared wavelengths because their absorption cross sections, σ, vary rapidly with wavelength (Figure 3-2).

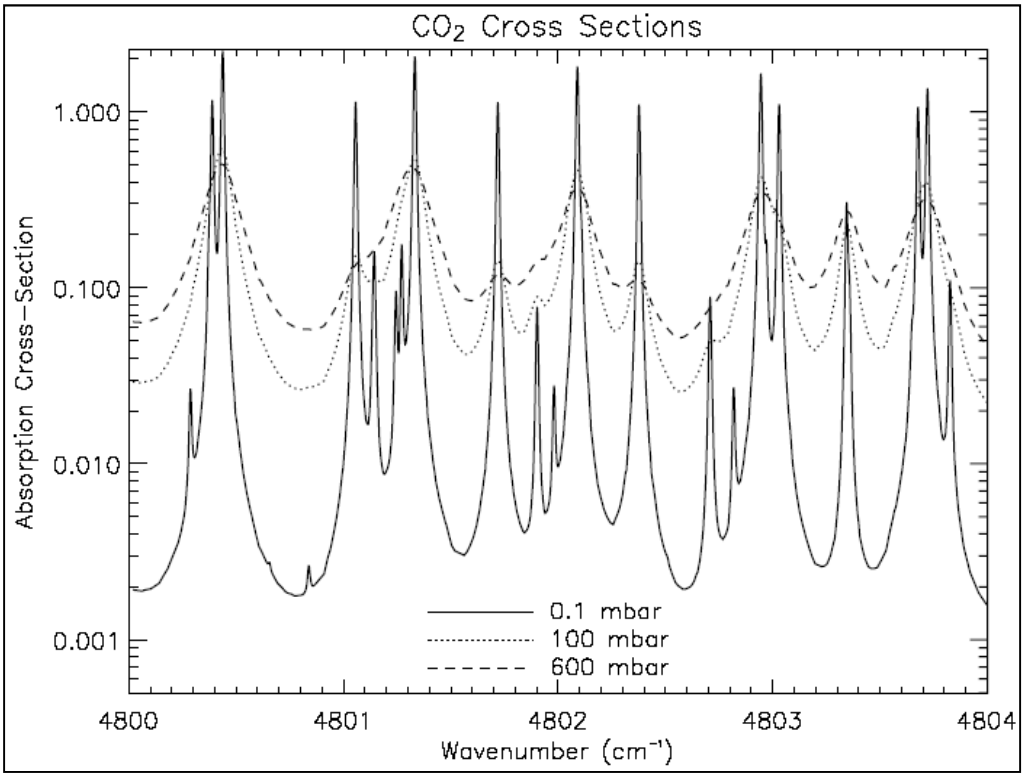

Figure 3-2. Spectral dependence of the absorption coefficients of CO_2 at wavelengths within the Strong CO_2 band at wavelengths near 2.08 μm are shown for pressures near 0.1, 100, and 600 hPa (mbar).

The strongest absorption occurs near the centers of the narrow vibration-rotation lines. At other wavelengths, the absorption can be orders of magnitude weaker. Hence, for small number densities and/or optical pathlengths, changes in these properties will therefore produce their largest variations in the radiance field at wavelengths near the line centers. Eventually, however, as the number densities or optical pathlengths increase, virtually all of the sunlight is absorbed at these wavelengths (e.g. the line cores become "saturated"), and the sensitivity to further changes decreases dramatically. The region of peak sensitivity then moves further down the line wings.

Even with its relatively high spectral resolving power ($\lambda/\delta\lambda$ ~ 20,000), the OCO-2 instrument does not completely resolve the narrow cores of spectral lines. In spite of this, the spectral variability must be resolved by the Forward Model to accurately quantify the absorption within the spectral range sampled by the instrument line shape function (ILSF). The most straightforward way to do this is to divide the spectral range of interest into a series of discrete spectral intervals that are narrow enough to completely resolve the spectral features contributed by atmospheric gases, the incident solar radiation field, airborne particles, or the reflecting surface. The equation of transfer must then be evaluated within each spectral interval. Finally, the full-resolution simulated spectrum must be convolved with the ILSF to simulate the spectrum observed by the instrument.

The primary advantages of this direct, spectrum-resolving approach are its conceptual simplicity and intrinsic accuracy, because it can fully accommodate all of the physics of the atmospheric and surface processes that contribute to the absorption and scattering of solar radiation. Its primary drawback is its computational expense, because the Equation of Transfer must be evaluated thousands of times to resolve the spectral structure within a near infrared O_2 or CO_2 band. A number of methods (c.f. correlated-k, spectral mapping, etc.) have been developed to reduce the number of spectral intervals needed, but all of these methods introduce simplifications and approximations that can introduce unacceptable errors in the computed radiance spectra.

To retrieve estimates of $N_{CO2}(z)$ or $N_{O2}(z)$ (or $\tau_{m,n}$) from observations of reflected solar radiation, the equation of transfer must be inverted. In general, this cannot be done analytically because of the complexity and nonlinearity of the equation of transfer. However, these quantities can be derived using conventional non-linear least squares fitting techniques, where these quantities are treated as unknown coefficients and the equation of transfer is the fitting function. In addition to the fitting function, these techniques require the first derivatives of the intensities with respect to any specific component of the state vector, $x_{m,n}$,

$$K_{m,n} = \partial I / \partial x_{m,n} \tag{3-11}$$

These "radiance Jacobians" are also generated by the Forward Model. Because the Equation of Transfer his highly non-linear with respect to most elements of the state vector, radiances and Jacobians must be derived for a surface/atmospheric state that is close to the actual state or the retrieval algorithm may not converge.

The primary components of the OCO-2 X_{CO2} retrieval process are summarized in Figure 3-3. Given an initial guess for the atmospheric and surface state and the observing geometry for a specific sounding, the "Forward Model" generates polarized synthetic radiance spectra and radiance Jacobians in the O_2 A-band and in the two CO_2 bands observed by the OCO-2 instrument. This model first generates these synthetic spectra on a spectral grid that fully resolves the solar spectrum at the top of the atmosphere, the absorption and scattering cross-sections for each atmospheric gas and airborne cloud and aerosol particle type included in the state vector, and the reflecting surface. The Instrument Model then convolves this full-resolution synthetic radiance spectrum the instrument line shape function and corrects for instrument polarization to simulate the spectrum recorded by the instrument. The Forward Model is described in Section 3.2.

The "state structure" includes atmospheric and surface properties that affect the spectrally dependent radiances observed by the satellite. The surface-atmosphere "state vector" includes

those components of the state structure that will be optimized by the retrieval algorithm to improve the fit between the observed and simulated radiances. The state vector is described in Section 3.3. Some of aspects of the instrument throughput (e.g. dispersion, instrument line shape) can also be included in the state vector. The methods used to generate radiance Jacobians are described in Section 3.4.

The "Inverse Method" is based on a Rodgers [2000]-type optimal estimation approach and has been described in Connor et al. [2008] and Boesch et al. [2006]. This model modifies the initial state vector to minimize differences between the observed and simulated spectra from each sounding. The inverse method is described in Section 3.5.

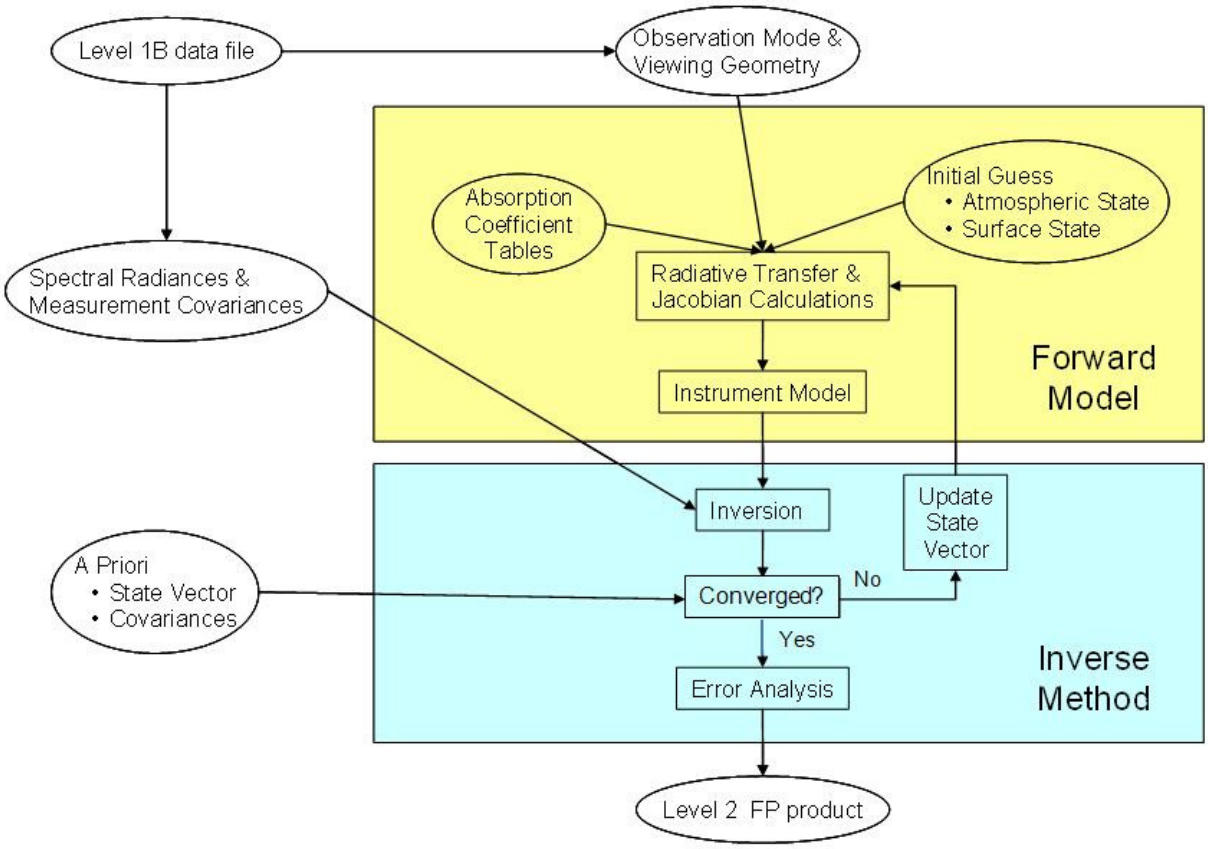

Figure 3-3. Flow diagram for the Level 2 Retrieval Algorithm.

Once the atmospheric state yielding the best match to the observed spectrum has been found, the algorithm then determines X_{CO2}, errors in X_{CO2} from different sources (such as vertical smoothing, measurement noise, etc), and the X_{CO2} column averaging kernel. This step is necessary because X_{CO2} is not itself an element of the state vector. Rather, it is determined from the profile of CO_2 which is part of the state vector. It is formally given by the total number of CO_2 molecules in the column divided by the total number of dry air molecules in the column. This step is labeled "Error Analysis" in Figure 3-3, and is described in Section 3.6.

Finally, given an estimate of X_{CO2}, a series of screening tests are performed to evaluate the quality of the retrieval. The criteria for a successful retrieval are currently under investigation and are subject to change prior to the final delivery of the data. Examples of success criteria are:

(1) Measurement relative χ^2 in each band < threshold
(2) A-posteriori X_{CO2} error < threshold
(3) Retrieved aerosol optical depth < threshold

3.2 Forward Model

The Forward Model simulates solar spectra and radiance Jacobians for analysis of observations acquired by the OCO-2 spacecraft in nadir, glint, or target modes. A simple cartoon illustrating the atmospheric and surface optical processes that contribute to the absorption and scattering of solar radiation as it traverses the atmosphere and is reflected by the surface is shown in Figure 3-1. The Forward Model can also generate synthetic spectra and Jacobians for the analysis of direct observations of the solar disk collected by the OCO-2 Instrument during Thermal Vacuum testing, or those collected by the Fourier Transform Spectrometers in the Total Column Carbon Observing Network (TCCON).

The software components of the forward model include:

- Spectrally-dependent surface and atmosphere optical properties
  - Cloud and aerosol single scattering optical properties
  - Gas absorption and scattering cross sections
  - Surface reflectance
- Solar Model
- Atmosphere/surface Radiative Transfer Model
- Radiance Jacobians module
- Instrument model (Spectral Dispersion, ILS, and polarization response)

The methods used to generate the spectrally dependent gas and particle optical properties are described in section 3.2.1. The solar spectrum at the top of the atmosphere is generated by a model described in section 3.2.2. Synthetic spectra are generated by a radiative transfer algorithm based on a spectrum-resolving, multi-stream multiple scattering radiative transfer model that incorporates the scalar discrete ordinate model, LIDORT [Spurr et al., 2001; Spurr, 2002], a polarization correction based on a fast, 2-orders of scattering model [Natraj and Spurr, 2007] and a series of other techniques to improve its accuracy, speed, and range of validity. This model is described in Section 3.2.3. The instrument model simulates the spectral dispersion, instrument line shape (ILS) function, and polarization dependence. The instrument model is described in section 3.2.4.

The inputs and outputs of the forward model are enumerated in Table 3-1.

Table 3-1 Inputs and Outputs to Forward Model.

Inputs	Outputs
Parameter structure: defines dimensions of sub-structures.	Radiance spectrum.
State Structure: • Atmospheric State • Surface State • Instrument (ILS, Dispersion, Polarization)	Partial derivatives (Jacobians) of the radiance spectrum with respect to each of the state vector elements.
Flag Structure: defines which elements of the state structure PD's are needed.	
Perturbation structure (for those Jacobians calculated by finite differences).	
Auxiliary parameter structure.	
Observation Geometry: Zenith angles, altitude, etc.	
Solar spectrum.	
Gas absorption and scattering cross sections.	
Aerosol optical properties.	
Surface BRDF Parameters	

Several assumptions have been made for analyzing the OCO-2 data. First, it is assumed that measured radiances have been radiometrically calibrated. Second, it is assumed that thermal emission from atmosphere is negligible compared with reflected sunlight. This is certainly true in the O_2A and Weak CO_2 bands, and is a reasonably good assumption in the Strong CO_2 band at 2.06 microns. Third, soundings that contain optically-thick clouds or aerosols can be rejected because they contain no useful information about CO_2 in the lower troposphere. It is assumed that inelastic scattering processes (e.g. Raman) are negligible at the wavelengths of interest to OCO-2. Further, the effects of airglow and absorption by the Chappuis bands of ozone in the O_2A band are also currently ignored.

3.2.1 Optical Properties

This section describes the atmospheric absorption and scattering calculation in the forward model. The radiative transfer code uses these values to predict the solar energy absorbed or scattered at each wavelength within an atmospheric layer at a given temperature and pressure.

To improve computational efficiency, the OCO-2 algorithm generates look-up tables for each absorbing gas in advance and interpolates between table entries at runtime. For absorbing gases, the table generation process records representative cross-sections k_v (cm^2/molecule) at *every* applicable wavelength for the full range of applicable pressures (Pa), temperatures (K), and frequencies (cm^{-1}). The resulting "ABSCO table," is a 4-dimensional look-up table for each absorbing gas in the forward model. For airborne cloud and aerosol particles, the wavelength single scattering optical cross sections and scattering phase functions are tabulated for specific particle modes. The wavelength dependent Rayleigh scattering cross-sections and phase functions are calculated for each iteration for each retrieval.

We begin with a broad overview of the gas absorption calculations and physical models used to produce the cross-sections, followed by a brief review of the laboratory experiments and spectroscopic parameters used to inform these calculations. We then describe software that implements the algorithm.

3.2.1.1 Gas absorption cross-section calculation

For a single molecule, the absorption associated with a single transition, *k,* between 2 states, *i* and *j,* centered at wavenumber, ν_k $(=\nu_{ij})$ can be written as the product of the corresponding line intensity S_k,$(= S_{ij})$ and a line shape function, $f(\nu,\nu_k)$. The monochromatic absorption coefficient at frequency ν_k of a given species is given by a summation over all relevant lines:

$$k_\nu{}^x = \sum_\nu S_k f(\nu,\nu_k) \tag{3-12}$$

In the lower atmosphere, the shape of the spectral lines is dominated by collisions between molecules. This is known as "pressure broadening," and can be represented most simply by the Lorentz shape function:

$$f_\nu = \frac{\alpha_L}{(\nu-\nu_k)^2+\alpha_L{}^2} \tag{3-13}$$

At lower pressures, where there are fewer collisions, the line shape is determined more the distribution of molecular velocities. These Doppler effects result in a Gaussian line profile:

$$f_\nu = \frac{1}{\alpha_D\sqrt{\pi}}\exp\left[\frac{-(\nu-\nu_k)^2}{\alpha_D}\right]. \tag{3-14}$$

α_L and α_D are the well-known Lorentz and Doppler half-widths at the half maximum (HWHM), respectively. At intermediate altitudes, both pressure and Doppler broadening are important, and the combined effects of these processes can be modeled by convolving these two profiles to yield a Voigt line shape.

Recent laboratory experiments [Tran and Hartmann, 2008; Predoi-Cross et al., 2008a; Hartmann et al., 2009] show that accurate retrievals of CO_2 and O_2 from near infrared solar spectra also require attention to other more subtle phenomena such as quantum-mechanical line-mixing and collision-induced absorption. Both processes are included in the OCO-2 absorption coefficient

(ABSCO) model. Line mixing (LM) occurs when the spectral lines of a given molecular species overlap, such that rotationally inelastic collisions can transfer intensity from one line to another. Line mixing can change the population of states (e.g. the distribution of line strengths within a band) as well as the shapes of individual spectral lines, overestimating the absorption in the wings of the band and underestimating the absorption in the peaks of the P and R branches [Tran et al. 2006]. Collision-induced absorption (CIA) occurs at high pressures, where interactions between molecules are strong enough and/or operate over long enough periods to violate the quantum rules that govern the "allowed" energy states for transitions of individual, isolated molecules, introducing (or "turning on") additional transitions.

Absorption cross-sections accounting for line mixing

To include the effects of line mixing and CIA, we have adopted versions of the codes developed by Niro et al. [2005a,b] for CO_2 and Tran et al. [2006] for the main isotope of O_2. Only a brief summary of these methods is given here. We refer the reader to these publications for a comprehensive description. These models utilize the Energy Corrected Sudden (ECS) model for line mixing, yielding a more general expression for the absorption cross-sections k_ν, of the form,

$$k_\nu^{LM}(p_X, P, T) = \frac{8\pi^2\nu}{3hc}\left[1-\exp\left(-\frac{hc\nu}{k_B T}\right)\right]\times\frac{P_x}{kT}\times\sum_k\sum_{k'}\rho_k(T)\times d_k\times d_{k'}\times \mathrm{Im}\left\{\left\langle\left\langle k'\left|\left[\mathbf{\Sigma}-\mathbf{L_0}-iP\mathbf{W}^{\mathbf{X-Y}}(T)\right]^{-1}\right|k\right\rangle\right\rangle\right\} \tag{3-15}$$

In this expression the sum extends over all lines k and k' and Im{ …} denotes the imaginary part. ρ_k and d_k are respectively the population of the initial level of line k and the dipole matrix element of the optical transition. The latter is related to the integrated line intensity S_k by:

$$S_k(T) = \rho_k(T)\times\sigma_k\times(1-e^{-hc\nu/k_B T})\times d_k^{\,2} \tag{3-16}$$

$\mathbf{\Sigma}$, $\mathbf{L_0}$, and $\mathbf{W^{X-Y}}$ are operators in the Liouville space. The complex relaxation operator, **W,** depends on the absorbing species, X, the band, the temperature, and the perturbing species, Y, and contains the influence of collisions on the absorption line shape. Its off-diagonal elements account for mixing between absorption lines, whereas the diagonal elements are related to the line pressure broadening coefficient γ_k and the line shifting coefficient δ_k. For each line k and absorbing species, X, we have:

$$\left\langle\left\langle k\left|W^{X-Y}(T)\right|k\right\rangle\right\rangle = \gamma_k^{X-Y}(T) - i\delta_k^{X-Y}(T) \tag{3-17}$$

There are two possibilities for the relaxation matrix W. If W is diagonal, the lines can be calculated in isolation. This results in the usual addition of Lorentzian (or Voigt) line

contributions but neglects line mixing contributions. Nonzero off-diagonal matrix elements connect the different transitions in the spectrum creating the line-mixing effect. A detailed description of how to compute the relaxation matrix for CO_2 can be found in Rodrigues et al. [1998]. Collisional transfers between levels in different vibrational states are extremely small and, hence, only the **W** elements connecting transitions within a given band are accounted for.

For OCO-2, we found that LM produces its largest impacts on the O_2 A-band (Figure 3-4) and the strong CO_2 band at 2.06 μm. Its impacts on the weak CO_2 band at 1.61 μm are much less pronounced.

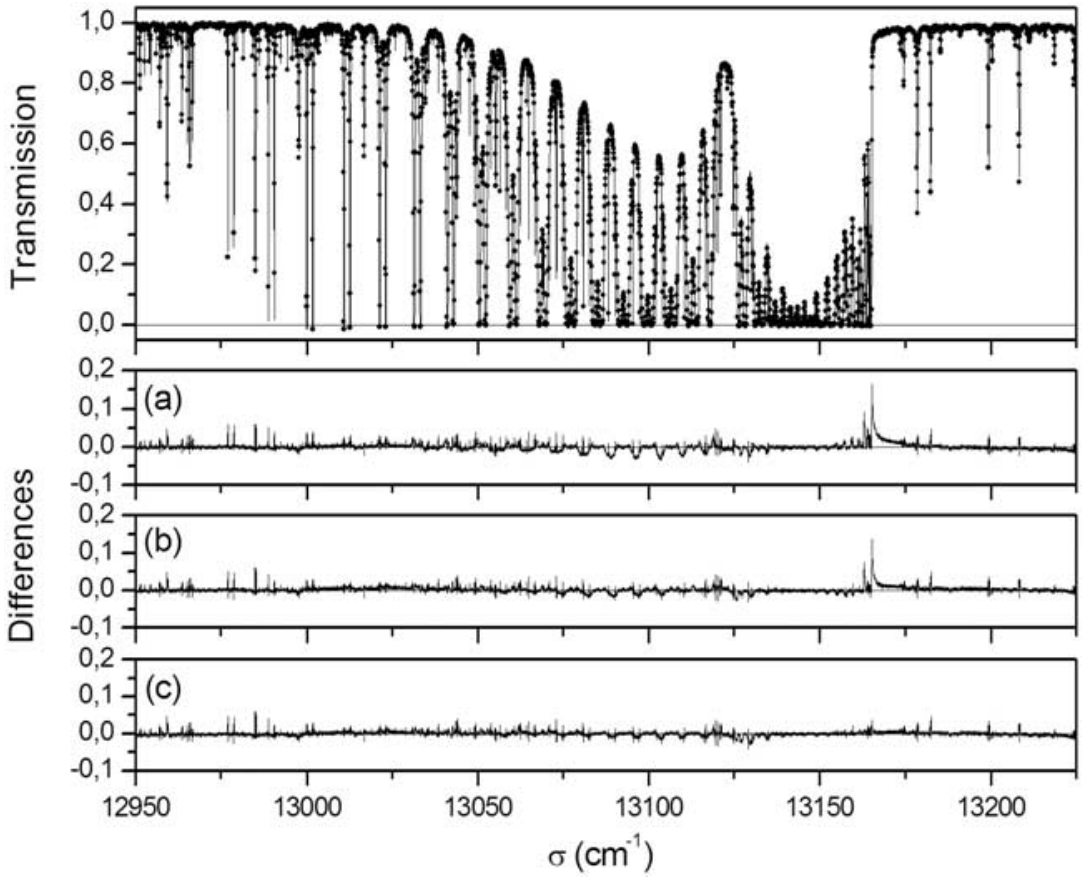

Figure 3-4. Line mixing effects in atmospheric O_2 spectra. Atmospheric transmission spectra measured (circles) and simulated. The differences at the bottom are between measured and simulated spectra using a) Only Voigt profile; [from Tran et al., 2006]. b) Voigt profile and Collision Induced Absorption (CIA); c) Line mixing and CIA. [from Tran and Hartmann, 2008]

Another important atmospheric effect included in ABSCO calculations is Collision Induced Absorption (CIA). Figure 3-5 shows that CIA can have a significant effect on absorption in the O_2 A band [Hartmann et al., 2008]. The possible role of a contribution of CO_2 CIA underlying the allowed ro-vibrational transitions in the 2.06 μm CO_2 band remains open.

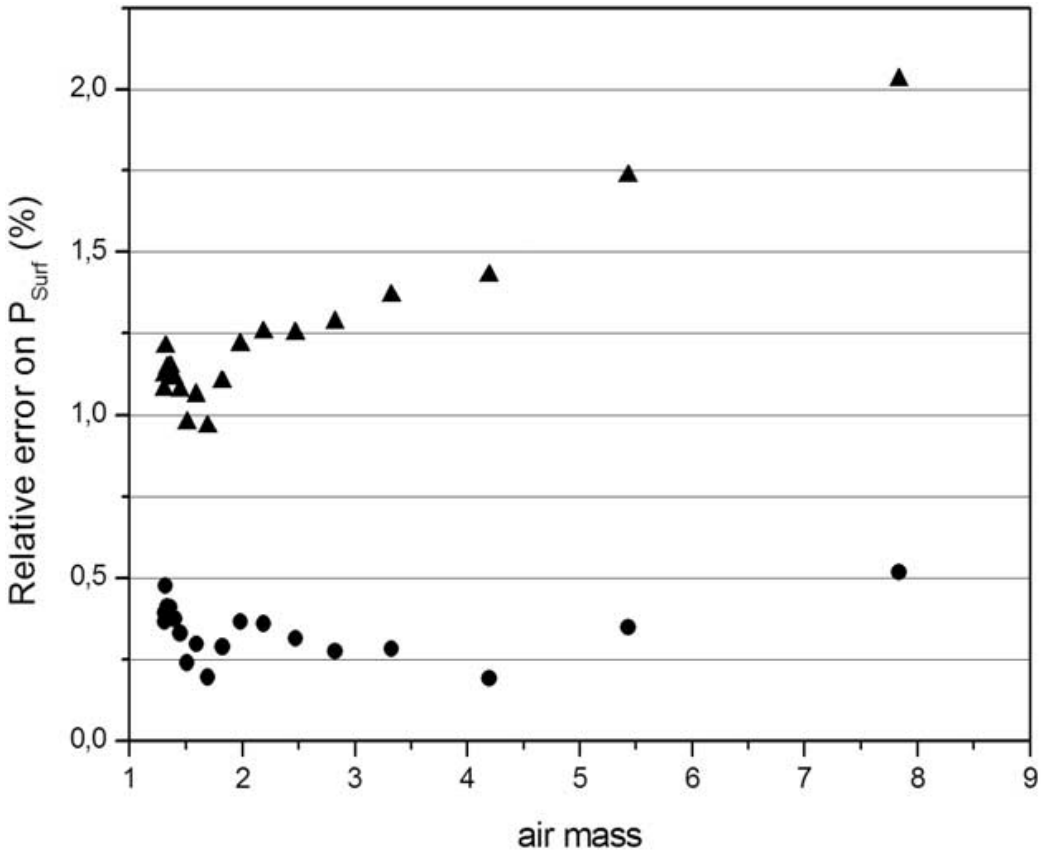

Figure 3-5. Relative errors (with respect to measured values) on surface pressures using Voigt lineshapes without CIA (solid triangles) and accounting for line-mixing and CIA (solid circles). [from Tran and Hartman, 2008].

3.2.1.2 Spectroscopy and Laboratory Measurements

This section describes the sources of model parameters used in computation of the absorption cross-sections. The OCO-2 mission required dramatic improvements to the near infrared spectroscopy of CO_2 and O_2 in the three spectral channels at 0.76, 1.61 and 2.06 μm. To achieve this, members of the Science Team formed international collaborations with leading experts to obtain high quality laboratory measurement and theoretical modeling of high resolution laboratory spectra of these two constituents.

The state-of-the-art was greatly advanced in measuring the spectral line positions, line intensities, and pressure-broadened line shapes and pressure shifts of CO_2 and O_2 absorption features. Improvements came from careful control of the experimental process applied for the laboratory measurement, the use of reliable spectrometers (the McMath-Pierce Fourier transform spectrometer (FTS) at Kitt Peak National Observatory, a Bruker 125 FTS at JPL, a Cavity Ringdown Spectrometer (CRDS) at NIST in Maryland, a Bomem FTS at NRC in Canada, a Bruker 120 FTS in Giessen, Germany, a Bruker FTS 66V at LISA in France) and sophisticated retrieval methods that evoked non-Voigt line shapes in a multispectrum fitting procedure [e.g. Devi et al., 2007 a,b].

For near-IR CO_2 alone, 13 peer-reviewed papers [Miller et al., 2004 a,b; 2005; Toth et al., 2006 a,b, 2007 a,b, 2008 a,b; Devi et al., 2007 a,b; Predoi-Cross et al., 2009; Sung et al., 2009]

provided the precisions essential for OCO-2, as well as for ground-based observations. Even CO_2 broadened by water vapor was characterized [Sung et al., 2009] for inclusion in future releases. Similarly improved O_2 A-band parameters were obtained [Robichaud et al., 2008 a,b; Robichaud et al., 2009; Predoi-Cross 2008 a,b; Tran and Hartmann 2008]. This body of recent work provided the essential line parameters along with validation of their precisions and accuracies of the individual line parameters themselves.

With a few important exceptions in the O_2 band, the "ordinary" line parameters such as widths, intensities, and positions have been incorporated into the publically available HITRAN 2008 database and summarized by Rothmann et al. [2009]. We describe these sources here for reference, and note a few instances where our line list departs from the standard.

O_2 A-band line parameters at 0.76 µm

In the A-band, lines corresponding to the $^{16}O_2$ (major) isotope are calculated separately from the minor isotopes. The major isotope calculations use line positions and intensities from the HITRAN 2008 database [Rothman et al., 2009]. The isotopic fractions for O_2 molecules are also based on those in HITRAN 2008. Pressure-broadening parameters (half-widths and pressure-induced frequency shifts) were based on the following parametric form from Yang et al. [2005], where N is the upper-state quantum number:

$$\gamma = A + \frac{B}{1 + c_1 J' + c_2 J'^2 + c_3 J'^4} \tag{3-18}$$

Pressure shifts for the major lines were taken from Robichaud et al. [2008a] for the P Branch, but the R branch used averages of shifts from Predoi-Cross et al. [2008b]. These values were then modified using an A-Band spectrum from the JPL Bruker FTS instrument [Robichaud et al., 2009]. Temperature dependence of widths draws on Robichaud et al. [2008a]. Brown and Plymate 2000 supply the temperature dependence of widths. O_2 Line Mixing coefficients for the major isotope are based on the calculations referenced in work by Tran et al. [2006], using values for line mixing and Collision Induced Absorption (CIA) from revisions in later work [Tran et al., 2008].

For the minor isotopic species, all parameters including pressure-broadening factors are identical to the HITRAN 2008 database [Rothman et al., 2009]. We use the Yang polynomial expression above for pressure broadening, but with coefficients updated by Robichaud et al. [2008a]. The positions and intensities of the two minor oxygen species are taken from Robichaud et al. [2009].

Near-infrared CO_2 parameters

The OCO-2 effort for CO_2 began with a laboratory study of the 4300 – 7000 cm^{-1} interval which first resulted in a database for use with Voigt line shapes. Extensive measurements were obtained using normal and isotopically-enriched CO_2 samples with the Kitt Peak FTS and ended with the creation of a new near-IR database that contained some 28000 lines involving 8 isotopologues with modeled line intensities $> 4.x10^{-26}$ cm^{-1}/(molecule cm^{-2}) at 296 K based on the laboratory studies [Toth et al. 2006 a,b; 2007 a,b; 2008 a] as well as estimates of weaker lines down to 10^{-30} cm^{-1}/(molecule cm^{-2}) at 296 K. Air- and self- broadening (widths and pressure shifts) were obtained as well (Figure 3-6)].

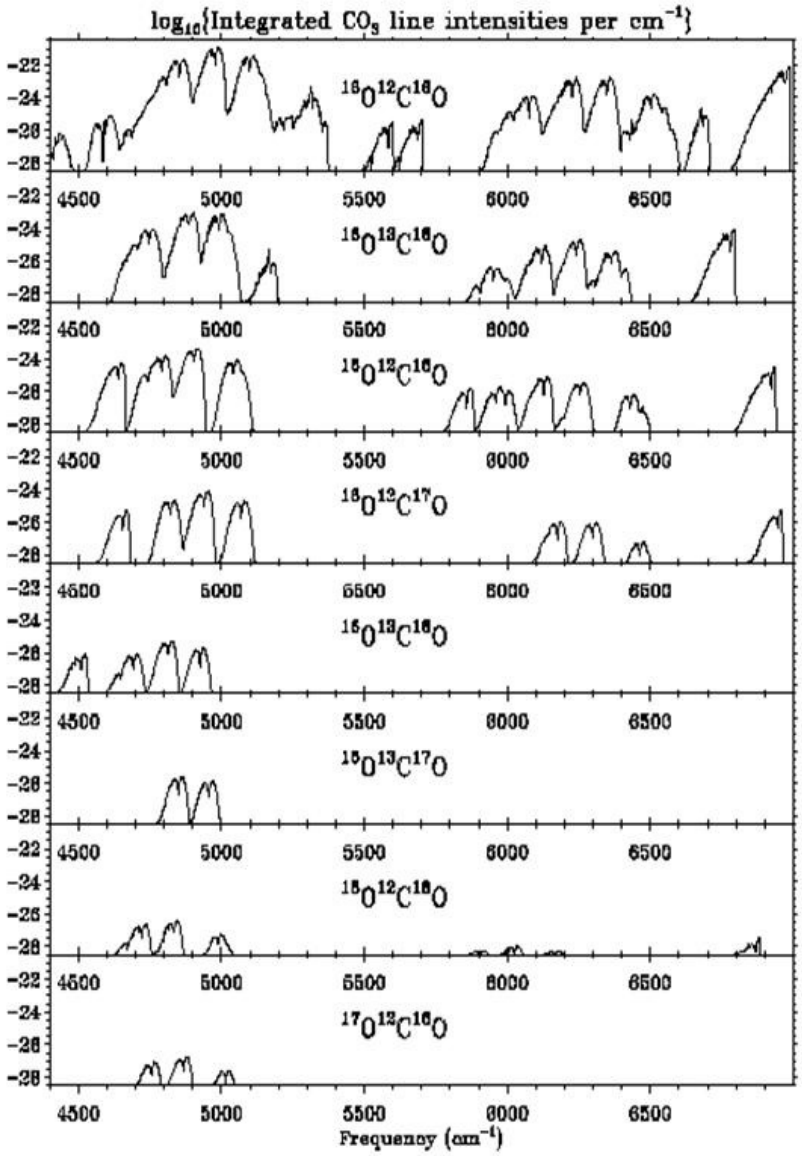

Figure 3-6. Laboratory Spectroscopy for carbon dioxide in the near-IR. Plotted are the log of intensities vs cm^{-1} by isotopologue contained in the near-IR "Voigt" database for CO_2 line parameters from 4300 to 7000 cm^{-1}. (See [Toth et al., 2008b].)

It was demonstrated that the commonly-used Voigt shape was not sufficient to reproduce high quality laboratory data, and a second set of analyses of the 1.6 μm region was undertaken [Devi et al., 2007 a,b; Predoi-Cross et al., 2009]; these efforts employed empirical off-diagonal matrix element form of line mixing with speed dependence (Figure 3-7). This provided an internally consistent set of positions, intensities, air-broadening (widths, shifts and their temperature dependences) sufficient for the weak CO_2 channel. A similar analysis of the strong bands at 2.06 μm is currently in progress and is expected to provide similar parameters in the strong CO_2 channel [Benner et al., 2009].

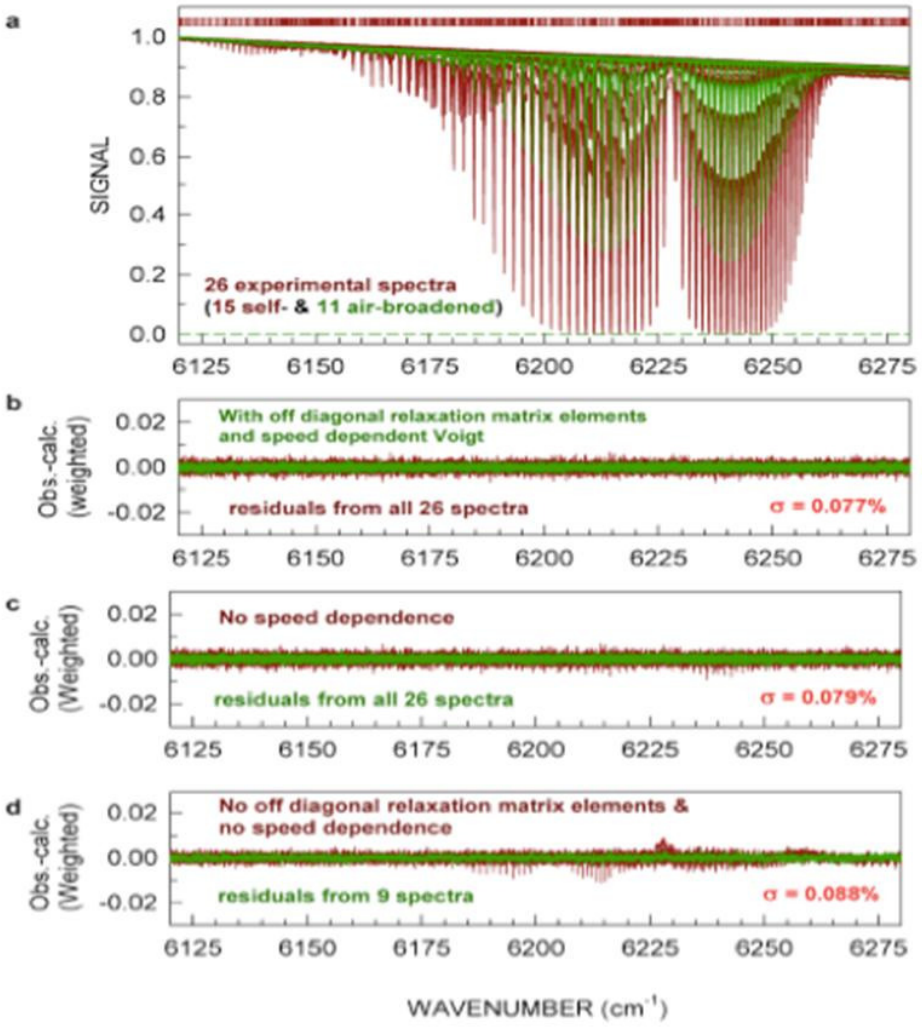

Figure 3-7. Retrievals of CO_2 line parameters from laboratory FTS spectra recorded at 0.01 cm^{-1} high resolution [Devi et al. 2007b]. Sophisticated multispectral retrievals using different combinations of molecular line shapes (Voigt, line mixing and speed dependence) reveal the poor quality of the usual Voigt profile; precisions of intensities limited to 1% with Voigt improves to 0.3% when additional line shapes parameters are evoked.

CO_2 line parameters and isotopic abundances are drawn from the HITRAN 2008 database. We refer the reader to Rothman et al. [2009] for these details. The only exception is the line mixing contribution, which is not yet available in HITRAN. These correspond to the contribution due to the off-diagonal terms of the W matrix in equation (3-15) above. Our strategy for incorporating line mixing follows the approach of Hartmann et al. [2009] who used it in atmospheric retrievals. Specifically, we note that absorption coefficients can be reformulated as an additive combination of the standard Voigt line shape with a asymmetric separate line-mixing part. We compute this line-mixing contribution with a separate line-mixing code by Hartmann et al. for the major lines based on parameters from the HITRAN 2000 database. Figure 3-8, taken from Hartmann et al. [2009], shows the improvement in synthetic spectra's match to atmospheric data after incorporating line mixing with this strategy.

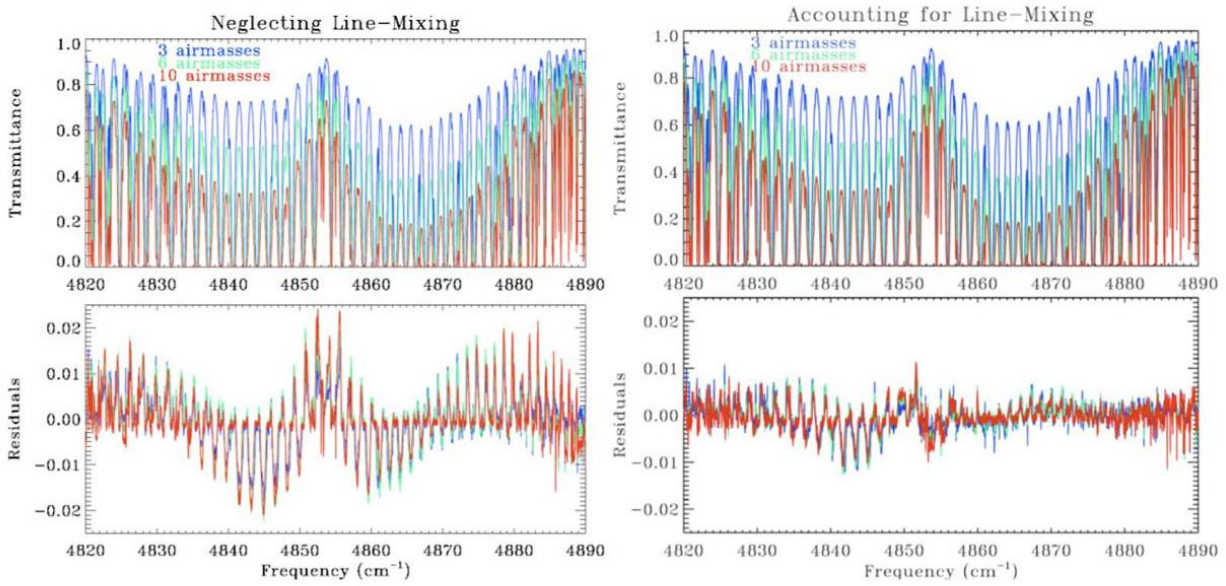

Figure 3-8. Line mixing effects evident in atmospheric CO_2 spectra. Atmospheric retrievals from Hartmann et al. [2009] showing transmittance in CO_2 absorption bands, with residuals before (Left) and after (Right) accounting for line mixing. Different colors correspond to measurements at different airmasses. The use of line mixing substantially improves the match between simulated and retrieved spectra.

Note that strong- and weak-band CO_2 line strengths in HITRAN 2000 differ significantly from more recent estimates, causing a discrepancy between the strength of the line mixing portion and the Voigt portion. To account for the difference we rescale the contribution due to Hartmann's line-mixing by a constant factor of 0.9. This provides the best empirical match to the ordinary HITRAN 2008 line parameters, and is consistent with results from the Hartmann 2009 study.

Other Absorbing Gases:

Several gases besides CO_2 and O_2 absorb within the spectral ranges used by OCO-2. The most important gas is water vapor (H_2O), which produces measureable absorption in all 3 bands. Line parameters for H_2O transitions in the OCO-2 channels are currently taken from the HITRAN 2008 database [Rothman et al., 2009]. Efforts to revise the near-IR water parameters are underway. [e. g. Jenouvrier et al., 2007 and Tennyson et al., 2009].

No other gases are currently included within the OCO-2 spectral ranges. Perhaps the most important omission is ozone (O_3) Chappuis-Wulf bands, which produce weak, quasi-continuum absorption within the O_2 A-band (2 to 4×10^{-22} cm^2/molecule). With ozone column abundances near 300 Dobson Units (e.g. 8×10^{18} molecules/cm^2) the absorption by this band increases from~0.4% at one air mass to > 3% at the largest air masses viewed by OCO. Omitting this band therefore introduces an air mass dependent bias in absorption, whose impact on retrievals has not yet been assessed.

Methane produces negligible absorption within the spectral ranges of strong and weak CO_2 bands used by OCO-2, but produces strong absorption at wavelengths near 1.66 μm, which is measured by the EnviSat SCIAMACHI and GOSAT TANSO FTS instruments. The CH_4 line

parameters near 1.66 μm included in the HITRAN 2008 database were not sufficiently accurate for retrieving this gas from GOSAT or SCIAMACHY spectra. However, updates to this database proposed by Frankenberg et al. [2008] and Lyulin et al. [2010] can produce substantial improvements in accuracy. More improvements were expected from the GOSAT-IBUKI mission for the methane line parameters.

Three other gases that absorb within the OCO-2 CO_2 bands are ammonia (NH_3), hydrogen bromide (HBr) and hydrogen sulfide (H_2S). HBr has a few weak transitions ($<10^{-22}$ cm^2/molecule) within strong CO_2 band. NH_3 has large numbers of weak transitions within the strong CO_2 band (5×10^{-21} cm^2/molecule) and within the weak CO_2 band (5×10^{-22} cm^2/molecule). Hydrogen sulfide (H_2S) also has weak transistions within both the strong (10^{-23} cm^2/molecule) and weak (5×10^{-22} cm^2/molecule) CO_2 bands. However, the column abundances of these gases are too small to produce measurable absorption away from strong sources, and are currently omitted from the algorithm.

3.2.1.3 Software Implementation

This section describes the current software implementation of the absorption cross-section computations. Figure 3-9 shows a schematic of the I/O structure. The OCO Spectroscopic Database includes all spectroscopic parameters. Here the "OCO Spectroscopic database" refers to the specific parameters detailed in the above section, which matches HITRAN 2008 in many cases but also includes the departures we have noted. These are reformatted for an absorption cross-section computation that includes both line mixing and CIA where appropriate.

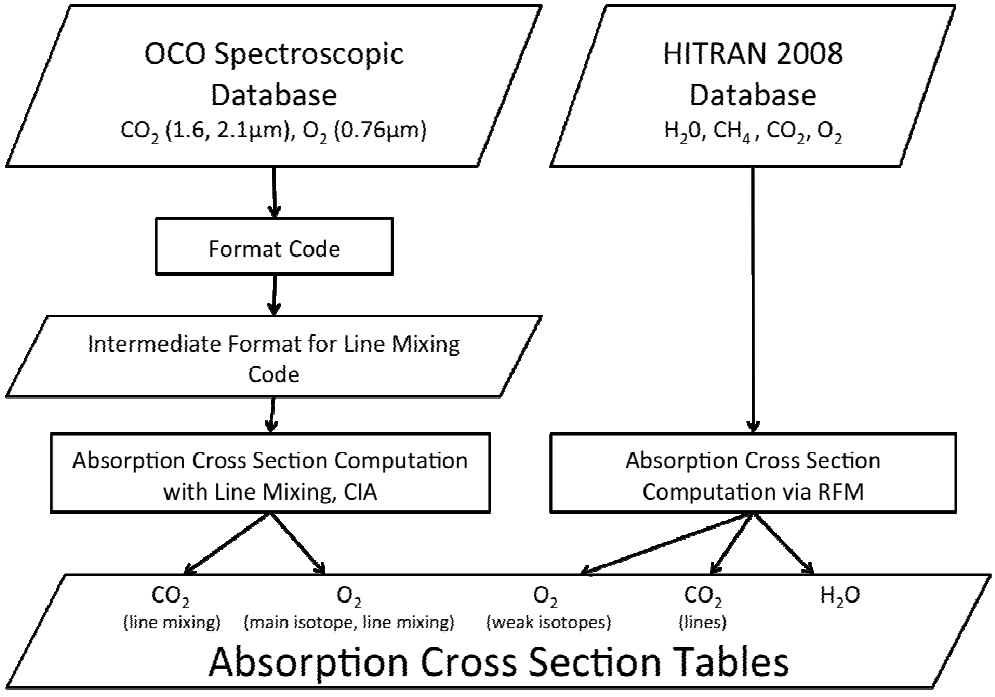

Figure 3-9. Input/Output Structure in the calculation of absorption coefficients.

The line mixing code used in the ABSCO tables is a modified version of codes used by in Niro et al. [2005a,b] and Tran et al. [2006]. These codes have been modified so that updated spectroscopic data can be used in the calculations (Table 3-2), and the output is compatible with the other modules of the ABSCO production system.

Currently, absorption cross-section tables for each gas are derived at 71 pressure levels between 5 and 102,034 Pa. At each pressure level, cross sections are derived for 19 temperatures, spaced at 10 K increments. The same, equally-spaced spectral grid is used at all levels. Currently, the resolution of this grid is 0.01 cm^{-1}, but that grid spacing is not adequate to resolve the narrow, Doppler broadened lines at levels above the tropopause. A higher-resolution spectral grid is currently under investigation.

Table 3-2 Sources of Line Parameters used for ABSCO table calculation

	0.76μm O_2	**1.61μm CO_2**	**2.06μm CO_2**
Table range, resolution	12745-13245 cm^{-1}, 0.01cm^{-1}	4700-6500cm^{-1}, 0.01cm^{-1}	4700-6500cm^{-1}, 0.01cm^{-1}
Positions	Robichaud [2008b, 2009][1]	Devi [2007a,b][1]	Toth [2008b][1]
Intensities	Robichaud [2008a, 2009][1]	Devi [2007a,b][1]	Toth [2008b][1]
Air-widths	Yang [2005], Robichaud [2008a][1,2]	Predoi-Cross [2009][1]	Predoi-Cross [2009][1]
Air-shifts	Robichaud [2008a][1] Predoi-Cross [2008a][1,3]	Devi [2007b][1]	Toth [2007b][1,4]
Temperature dependence	Brown [2000][1]	Predoi-Cross [2009][1]	Predoi-Cross [2009][1]
Line shapes	Voigt	Voigt	Voigt
Isotopic abundances	Rothman [2009], Šimečková [2006][1,4,6]	Rothman [2009], Šimečková [2006][1,6]	Rothman [2009], Šimečková [2006][1,6]
H_2O-broadened widths	n/a	n/a	n/a
Air-Line mixing	Tran [2008] [4]	Hartmann [2009][5]	Hartmann [2009][5]
" Temp. dependence	Tran [2008] [4]	n/a	n/a
Narrowing	n/a[4]	n/a	n/a
CIA	Tran [2008]	n/a	n/a

[1] Included via the HITRAN 2008 spectroscopic database, Rothman [2009].
[2] Strong and weak lines in the O_2 band are currently derived from different sources. See text for details.
[3] Modification to pressure shifts in the R-branch using JPL Bruker spectrometer measurements.
[4] See notes in text on line-mixing calculation

3.2.1.4 Calculation of Gas absorption optical depths in each atmospheric layer

Once we have the lookup tables of cross section on pressure P, temperature T, and wavelength λ, we must use the actual profiles of P, T and gas concentration to calculate optical depth for each layer and gaseous species.

Let us suppose we have a thick layer that goes from a lower pressure P_{bot} to an upper pressure P_{top} and we wish to calculate the optical depth of this layer for a certain species of gas. Let the dry air volume mixing ratio of this gas be q_{gas} which is defined as the number of moles of the gas per mole of dry air. Further, let us call the absorption cross-section of the gas (in $m^2\ mol^{-1}$) $K(P,T)$ at a particular wavenumber. Because the temperature T is an intrinsic function of the pressure P for the given profile, we write the gas absorption coefficient for this specific layer as $k(P)$.

In an infinitesimal layer, it can be shown that the number of molecules of *dry air* (against which the volume mixing ratio of any gas is defined) can be written as

$$N_{dry}\, dZ = -\frac{dP}{g M_{dry}}(1-q) \tag{3-19}$$

where dZ is the layer width in meters, N_{dry} is the number of moles of dry air per cubic meter, g is the local gravitation acceleration, q is the local specific humidity, and M_{dry} is the molar mass of dry air in $kg\ mol^{-1}$. Thus, the total optical depth of a thick layer can be written as

$$\tau_{gas} = \int_{P_{top}}^{P_{bot}} q_{gas} \frac{k(P)(1-q(P))}{g(P)\, M_{dry}}\, dP \tag{3-20}$$

Note that we've expressly allowed g, q, q_{gas}, and k to vary as a function of pressure across this layer. Unfortunately, we only know each quantity at the boundary of the layer in question. Therefore, we must make assumptions about how each varies across the layer in order to evaluate the integral. Initially, each quantity was simply evaluated at the center of the layer assuming a linear variation; however, this approach can cause small biases in the total optical depth of a given gas and lead to corresponding biases in retrieved XCO_2. This is mostly due to layers at the top of the atmosphere that span sometimes close to two orders of magnitude in pressure (say from 1 to 100 mbar) – the variation across this layer in k is so great (and quite nonlinear) and that we cannot simply ignore it.

A straightforward approach that largely eliminates this bias is to divide each layer into a number of sublayers. Then the optical depth for each sublayer is evaluated according to the approximation

$$\tau_{sub} = \frac{q_{gas,cen}(1-q_{cen})}{g_{cen}\, M_{dry}} K(P_{cen}, T_{cen})\, \Delta P \tag{3-21}$$

where the "*cen*" subscript indicates a quantity to be evaluated at the center of the layer; all such quantities are evaluated using linear interpolation in pressure.

$K(P_{cen},T_{cen})$ is then evaluated using 2d linear interpolation in both pressure and temperature. The optical depth of the full layer is then simply the sum of the optical depth of its component

sublayers. Note that a better but more complicated choice would be to do a quadratic interpolation in temperature. This is not used as the lookup table in temperature is relatively fine, having grid points every 10 K. It was found that the error due to this formulation was relatively minor, though future versions of the code may be updated to allow for a quadratic temperature interpolation.

The level-2 FP code currently subdivides each model layer into 10 sublayers of equal pressure width. This has been found to result in almost no bias and is yet very fast. This is accomplished in the module *rtmod/gas_tau.F90*. Once the sub-layer optical depths are evaluated, they can be simply summed to obtain the total gas optical depth of each layer (and for each species of gas).

3.2.1.5 Rayleigh scattering cross sections

Rayleigh scattering is accounted for in all OCO bands, though it is most important in the oxygen-A band. The Rayleigh scattering cross-section is calculated using the following classic model:

$$\sigma_R = \frac{24\pi^3}{N_s^2 \lambda^4} \frac{(n_s^2 - 1)^2}{(n_s^2 + 2)^2} \frac{6 + 3\rho}{6 - 7\rho} \tag{3-22}$$

where λ is the wavelength, N_s is the number density of air at some pressure and temperature, and n_s is the index of refraction of standard air *at the same pressure and temperature*; according to Lorentz-Lorenz theory, the product of the two terms in involving these two variables is independent of pressure and temperature. We take $N_s = 2.687 \bullet 10^{19}$ molecules/cm^3 at 273.15 K and 1013.25 mbar. The prefactor $24\pi^3/N_s^2$ may be calculated to be $1.031 \bullet 10^{-20}$ m^2 μm^4 per molecule, such that specifying λ in μm will result in the cross section have units of m^2/molecule.

The index of refraction for air at standard pressure and 273.15 K is taken from Allen [1964], using the following parameterization:

$$n_s = 1 + a * (1 + b\, \lambda^{-2}) \tag{3-23}$$

where λ is in microns, a= 2.871e-4 and b = 5.67e-3. The depolarization factor is taken to be a constant over all the OCO bands, with a value of 0.0279 as suggested by Young [1980]. The Rayleigh phase matrix including polarization is a standard formulation (e.g. Hansen & Travis, [1974]).

In order to calculate the Rayleigh optical depth τ_R for a given layer, it is necessary to multiply the cross section by the total number of air molecules per m^2 in the layer. For a given layer with pressure width ΔP given in Pa and mean gravity g in m/s^2, this is given approximately by:

$$n\Delta z = \frac{N_A \Delta P}{M_{dry}\, g} \tag{3-24}$$

where N_A = 6.02297e23 is Avogadro's number (note this value is slightly erroneous), and M_{dry} = 28.96e-3 is the molar mass of dry air in kg/mole. Because this should represent the total number of air molecules in a layer, it must include the wet and dry contributions. Thus, it will be slightly

wrong due to its neglect of the presence of water vapor. The correct value would be that of equation (2) multiplied by the virtual temperature of the layer divided by the physical temperature of the layer. This will cause errors of up to 2-3% in the lower troposphere in particularly wet atmospheres.

3.2.1.6 Cloud and aerosol cross-sections

The single scattering optical properties (cross sections, single scattering albedos, scattering phase functions) of cloud and aerosol particles are also pre-computed and tabulated. Currently, the OCO-2 retrieval algorithm includes only four different types of airborne particles for each sounding. The first two are liquid water and ice clouds. The wavelength dependent optical properties for liquid water clouds were calculated from Mie theory assuming a Gamma particle size distribution and an effective radius of 8 μm. The optical properties of ice clouds with a single effective radius of 70 μm were obtained from the database published by Baum et al. [2005a, 2005b], and interpolated to the wavelengths of interest.

The second two aerosol types currently implemented in the algorithm include a continental aerosol type [Shettle and Fenn, 1979], which is concentrated in the boundary layer, and a stratospheric aerosol consisting of 75% sulfuric acid [Palmer and Williams, 1975]. Both of these particle types are assumed to consist of spherical particles, and their optical properties are computed with a Mie code, using a modified gamma-function size distribution and size parameters from the World Climate Research Programme, (1986). The optical properties for non-spherical aerosols, such as coarse mineral dust, have also been derived using a T-matrix code [Mishchenko and Travis, 1998], but are not currently used in routine retrievals. Water cloud, ice cloud, and aerosol all include a fully polarized treatment of the scattering phase function, using a standard formalism [Siewert, 1982; de Rooij and van der Stap, 1984].

3.2.2 Solar Model

The OCO-2 FP Forward Model uses a solar model to calculate a synthetic solar spectrum. The solar model consists of two parts: the solar absorption model and the solar continuum model. A solar model offers several advantages over a measured solar spectrum:

i. Solar spectrum can be calculated on the exact spectral grid that is needed, avoiding the complication of re-sampling the measured spectrum which results in undersampling structures

ii. A measured solar spectrum is already convolved with the ILS of the spectrometer that measured it. Using such a measured solar spectrum causes spectral artifacts (called I_0 effect)

The solar absorption model calculates the solar lines based on empirical solar line list that has been optimized for either a disk-center or a disk-averaged observations. This solar absorption model has been used extensively for the analysis of ground-based FTS spectra, both in the infrared [e.g. Toon et al., 1999] and the NIR [e.g., Yang, et al, 2002, Washenfelder, 2003]. We assume that the solar absorption spectrum is invariant in time. This is probably a good assumption in the infrared and near-infrared, but less good in the visible. All solar lines are assumed to have an absorption line shape of the form:

$$f(v) = exp\{-(v-v_0)^2 / [(\alpha_d^4 + (v-v_0)^2 * y^2)]\} \quad (3\text{-}25)$$

where

ν_0 is the line-center frequency (cm^{-1})

y is the 1/e folding width (cm^{-1})

α_d is the Doppler width (cm^{-1}).

In the Doppler limit, i.e. $\alpha_d^2 >> (v-v_0).y$

$$f(v) = exp\{-((v-v_0) / \alpha_d)^2\}. \quad (3\text{-}26)$$

In the far line wing limit, i.e. $(v-v_0).y >> \alpha_d^2$,

$$f(v) = exp(-|(v-v_0) / y|). \quad (3\text{-}27)$$

Near the line center, the line shape is essentially Doppler, but in the line wings it decays exponentially (if y>0). This choice of line shape has no physical basis, but seems to give a reasonable representation is nearly all cases. The only exceptions are the extremely broad lines of light atoms such as H (atomic hydrogen) or Mg. However, by representing the H absorptions as super-positions of two lines, one narrow and the other broad, adequate results were obtained. Molecular absorptions (e.g. CO, OH, NH, CN) tend to have narrow, Doppler line shapes because they are confined to a relatively narrow layer in the cooler, upper, part of the solar atmosphere. In the hotter depths, molecules become dissociated. Atomic transitions, on the other hand, are formed over a much wider range of solar altitudes, and hence a wider range of pressures and temperatures. This gives rise to line shapes whose wings decay in an approximately exponential manner with the distance from line center. The line shape of equation above does a reasonable job in both cases. This algorithm also makes allowances for the effect of the finite FOV of the observing instrument, which gives rise to:

- broadening of the solar lines due to the linear variation of the Doppler shift from solar rotation across the solar disk.
- distortion of the solar lines due to limb darkening.

The algorithm represents solar emission lines by using negative strengths.

3.2.2.1 Solar Line List

The solar line list covers the 550-15000 cm^{-1} region and contains over 18,000 lines. This is based on the work of Geller [NASA RP 1224, 1992] who analyzed the ATMOS exo-atmospheric spectra covering the 600-4800 cm^{-1}. The line list was subsequently extended to 5600 cm^{-1} using MkIV balloon spectra, and to 15000 cm^{-1} using Kitt Peak solar spectra. It has also been checked against balloon spectra acquired by Camy-Peyret in the 12800-13200 cm^{-1} region (A-band), although these balloon spectra were not used in the derivation of the solar line list.

3.2.2.2 Solar Continuum Model

The solar continuum model calculates the solar Planck Function which is then multiplied with the solar absorption spectra to obtain the solar spectrum. The solar continuum model is based on a polynomial fit to the near-infrared part of the low resolution extra-terrestrial solar spectrum acquired by the SOLSPEC instrument [Thuillier et al., 2003]. The uncertainty of the SOLSPEC data is estimated to be around 1 and 2%. We assume that the solar continuum is invariant over time.

The SOLSPEC spectra are given for a Sun-Earth distance of 1 Astronomical Unit (AU, 1 AU = 149597871 km), so that it is necessary to scale the spectrum with the square of the seasonally-varying Earth-Sun distance, which has been taken from http://eclipse.gsfc.nasa.gov.

3.2.2.3 Solar Doppler Stretch

The relative velocity of the Earth and the Sun caused by the Earth's rotation and the ellipticity of the Earth's orbit about the sun produces daily and seasonal Doppler shifts in the solar lines with respect to the telluric lines. The Doppler shift, $\Delta\lambda$, for wavelength, λ, is calculated assuming a small (non-relativistic) relative velocity v_{rel}:

$$\Delta\lambda/\lambda = - v_{rel}/c \tag{3-28}$$

where c is the speed of light.

The relative velocity is given by the sum of the Earth-Object radial velocity and the Earth rotational velocity component. Both are calculated using the solar ephemeris based on Van Flandern and Pulkkinen [1979] which is claimed to be accurate to ±1 arcminute for ±300 years. Note that this correction does not include the Doppler shift due to the spacecraft's ~7 km/sec velocity around the Earth, which affects solar and telluric lines equally.

3.2.3 Radiative Transfer

The radiative transfer module (RTM) encapsulates all the physics associated with the modification of the solar radiation during its passage through the atmosphere and reflection by the surface. This is greatly complicated by the fact that some of the radiation is reflected back to space (by cloud/aerosol) before hitting the ground causing the average photon path to be wavelength-dependent as well as by the fact that reflected radiation is strongly polarized, especially in glint mode over ocean.

Because OCO-2 is polarization sensitive and the radiation can be highly polarized, it is essential that the forward-model calculations take this into account and calculate the fully-polarized radiation. We describe the radiance at a given wavelength incident upon the instrument by a 3-element Stokes vector {I, Q, U}. We neglect the circular polarization component because it is generally negligible and OCO-2 is not sensitive to it. Traditionally, a fully-polarized radiative transfer code such as VLIDORT would be used for the calculation, but this is simply too computationally expensive. Instead, we resort to a piecemeal approach. First, we approximate the Stokes vector as:

$$I = I_1 + I_{ms} + I_{corr} \quad (3\text{-}29)$$

$$Q = Q_1 + Q_2 \quad (3\text{-}30)$$

$$U = U_1 + U_2 \quad (3\text{-}31)$$

where subscript '1' denotes first order of scattering (and includes the direct beam reflected from the surface), '2' denotes second order of scattering, 'ms' denotes all orders of scatter above the first, and I_{corr} represents a polarization correction to I_{ms}. The various terms are then calculated as follows:

1. I_1, Q_1, and U_1 are calculated by a fast, fully-polarized single-order of scattering module.
2. I_{ms} is calculated by Radiant, a multiple-scattering scalar radiative transfer code.
3. Q_2, U_2, and I_{corr} are calculated by a fully-polarized, second-ordering of scattering technique called 2OS.

Our goal is a spectrum of I, Q, and U at each of the ~40,000 high-resolution spectral points, in order to convolve with the instrument response. However, even with the savings of not using vectorized, all-orders-of-scatter code, a direct brute-force process is still too expensive. Therefore, a method dubbed the Low Streams Interpolator is employed to drastically speed up the radiative transfer process and avoid the direct, brute-force approach.

3.2.3.1 LIDORT

The Full Physics algorithm uses LIDORT [Spurr et al., 2001; Spurr, 2002] to solve the radiative transfer equation (RTE). LIDORT is a linearized discrete ordinate radiative transfer (RT) model that generates radiances and Jacobians (derivatives of the radiance with respect to atmospheric and surface properties) simultaneously. The Jacobians are computed by an internal perturbation analysis of the complete discrete ordinate solution to the RTE. LIDORT is a quasi-spherical model; the direct beam and line of sight attenuations are treated for a curved atmosphere while the multiple scattering considered to be locally plane parallel.

3.2.3.2 Polarization Correction: The Two Orders of Scattering (2OS) Model

The OCO-2 FP code uses LIDORT as the scalar RT model. However, to fully describe the state of light observed by the detector, polarization has to be taken into account. Calculations of multiple scattering with full treatment of polarization are computationally very expensive. Since multiple scattering is depolarizing, it is reasonable to expect that the polarization could be accounted for by a low-order scattering approximation. Natraj and Spurr [2007] extended the scalar Kawabata and Ueno [1988] model to compute the first two orders of scattering (2OS) for vertically inhomogeneous scattering media with polarization included. To enable accurate computations for the range of solar viewing angles encountered by OCO-2, atmospheric transmittances for the incoming solar beam are treated for a curved spherical-shell atmosphere [Spurr, 2002]. For the glint and nadir modes of operation, there is also a correction for the sphericity along the line of sight. Polarization induces a change in the intensity; to account for

this, we compute a correction to the scalar intensity. The 2OS model simultaneously computes both the simulated backscatter radiance (and intensity correction) and any number of associated weighting functions (partial derivatives of the radiance with respect to retrieved and other atmospheric and surface properties). The 2OS computation is an order of magnitude faster than a full multiple scattering scalar calculation and two orders of magnitude faster than a vector multiple scattering computation.

Theory

The formulation of the 2OS model is based on the invariant imbedding theory of RT. The contribution from the p^{th} order of scattering is related to that from the $p\text{-}1^{th}$ order of scattering by an integro-differential equation. Starting from direct transmission, the expressions for subsequent orders of scattering can be derived. This is particularly straightforward for the first two orders of scattering. A Fourier series expansion is done to solve the problem efficiently. The expressions for the Stokes parameters *I*, *Q* and *U* are as follows:

$$I_{OCO} = I_{sc} + I_{corr} \tag{3-32}$$

$$Q_{OCO} = Q_1 + Q_2 \tag{3-33}$$

$$U_{OCO} = U_1 + U_2 \tag{3-34}$$

where the subscripts OCO-2, sc,1 and 2 are, respectively, the OCO-2 measurement, scalar computation (from Radiant), first and second order computations (from the 2OS model). I_{corr} is the intensity correction computed by the 2OS model.

Evaluation

The OCO-2 full physics RT model has been tested against the full multiple scattering vector model VLIDORT [Spurr, 2006] for the OCO-2 nadir, glint and target modes of operation. Computations were performed for different solar zenith angles, surface types and aerosol loadings [Natraj et al., 2008]. The radiance errors using the hybrid LIDORT-2OS model are an order of magnitude (or more) smaller than errors arising from the use of LIDORT alone. In addition, a linear error analysis study showed that the errors in the retrieved X_{CO2} using the hybrid model are much lower than the ‘‘measurement’’ noise and smoothing errors. On the other hand, the scalar model alone induces X_{CO2} errors that could dominate the retrieval error budget.

3.2.3.3 RT calculations with Low-Streams Interpolation

The radiative transfer (RT) code inside the full-physics algorithm, Radiant, relies on a quadrature-based type approach wherein the code effectively only treats radiation coming from specific, discrete zenith angles or “streams”, and interpolates between these angles to find the radiation at an arbitrary angle. In the nomenclature, a code is said to be run with N streams total, where N/2 is the number of streams in either the upper or lower hemisphere. The computational burden in theory goes like N^3, because the codes largely rely on multiplication and inversion of NxN matrices. However, often there is significant overhead which lessens the extreme dependence on N to be more like N^2, especially for lower numbers of streams.

The number of streams required to achieve a given accuracy varies on the type of atmosphere in question. Generally speaking, the stronger the scattering, the higher is number of streams required. However, internal tests have shown that a minimum of 8 streams is required, and up to 32 streams would be highly desirable for the retrieval code. 32 streams is too much if run in a brute-force manner, where every high resolution spectral point is run through the radiative transfer with 32 streams.

Fortunately, there are some features of the RT that can be exploited to lower the amount of calculation time required to simulate a large number of instrumental channels that lie within a relatively small part of the spectrum. Primarily, we can exploit the fact that within the narrow OCO-2 bands, scattering characteristics of clouds, aerosols, and the surface will vary much more slowly than do absorption characteristics. A method has been developed for use in the retrieval code call the "low-streams interpolator" which follows the following basic approach:

- Within a band, do one 4-stream calculation for every high-resolution spectral point. These will yield relatively low-accuracy values of I, Q, and U at each such point. In the O2-A band, this is more than 20,000 RT calculations.
- Form average optical properties for all spectral points with similar total gas optical depths. Create approximately 20 logarithmically-space optical depth bins.
- Perform 4 and 32 stream calculations on each of these ~20 bins.
- For each bin, determine the errors made in I, Q, and U by the 4-stream calculations relative to the 32 stream calculations
- Assume these errors vary linearly in total gas optical depth, and interpolate to determine the approximately error made by the 4-stream calculation at *all spectral points*.

Analysis has demonstrated that the error made by only using 4 streams varies in a smooth way when plotted against the log of the total-column gas optical depth. The errors for I, Q, and U always vary relatively smoothly with total gas optical depth. There is some scatter for unknown reasons, but this is typically small and leads to an acceptable error once the radiances have been convolved with the ILS. The result is that virtually all the time is spent doing the ~20,000 4 stream calculations; the ~20 32 stream calculations take significantly less time, as well as the error interpolation required to "correct" the 4-stream calculations. Thus we essentially get a 32-stream calculation for the speed cost of a 4-stream calculation. In addition, because the technique is so simple (involving just a couple of very simple equations), it was very straightforward to linearize such that it can handle Jacobians as well.

3.2.4 Instrument Model

The radiative transfer model produces high resolution (~0.01 cm^{-1}) synthetic spectra of I, Q, and U for a specified observing geometry and surface/atmospheric state. Before these synthetic spectra can be compared to the calibrated, geolocated spectral radiances, they must be corrected for instrument dispersion, convolved with the instrument line shape (ILS) function. The

resulting, synthetic I, Q, and U, must then be corrected for instrument polarization. Each of these steps is defined below. The instrument model performs these steps.

3.2.4.1 Pixel-Wavelength Mapping

The wavelength λ for detector pixel *i* and spectrometer *k* is given by

$$\lambda_i = \sum_{n=1}^{N} d_k^n \times i^{n-1} \tag{3-35}$$

where *d* are the *N* dispersion coefficients for spectrometer *k*.

3.2.4.2 Instrument Lineshape Function (ILS)

The instrument lineshape function ILS describes the response of the instrument to light with a wavelength λ. Mathematically this can be described by a convolution of the monochromatic intensity *I* with the ILS:

$$I(\lambda) = \int_{-\infty}^{+\infty} I(\lambda') \times ILS(\lambda, \lambda')\, d\lambda' \tag{3-36}$$

3.2.4.3 Continuum

The calculated spectrum can be scaled by a detector pixel dependent scale factor called continuum. For radiometric calibrate spectra, this continuum factor is set to one. For non-calibrated spectra, this continuum value is used to match the absolute values of the measured and modeled spectrum.

$$C(\lambda) = \sum_{n=1}^{N} c_k^n \times (\lambda - \lambda_c)^{n-1} \tag{3-37}$$

where c are N continuum coefficients for spectrometer *k* and λ_c is the center wavelength of the spectral window.

3.2.4.4 Polarization Correction:

The radiative transfer model used in the L2 retrieval algorithm calculates the polarized radiance at the top of the atmosphere, returning Stokes' vector (I, Q, U, V) . The components of this vector provide the total intensity I and parameters Q, U and V that specify (indirectly) the degree of polarization, its ellipticity, and the preferred orientation of the polarization ellipse. Stokes' vector is specified with reference to the plane defined by the direction of propagation of the radiation and the vector perpendicular to the surface of the Earth at the target. Meanwhile, the OCO-2 instrument only transmits only radiation with its plane of polarization aligned with the Y -axis of the satellite. The computed radiances must therefore be corrected for polarization before

they can be compared to the observed values. This correction is straightforward given the viewing geometry of the sun, surface target, and the observatory (Figure 3-10).

Observing Geometry:

The area on the surface of the reference ellipsoid covered by the eight footprints of OCO-2 is referred to as the target area, and the centre of this area as the target centre. Here, we assume that the slits of the three spectral channels are parallel but displaced laterally.

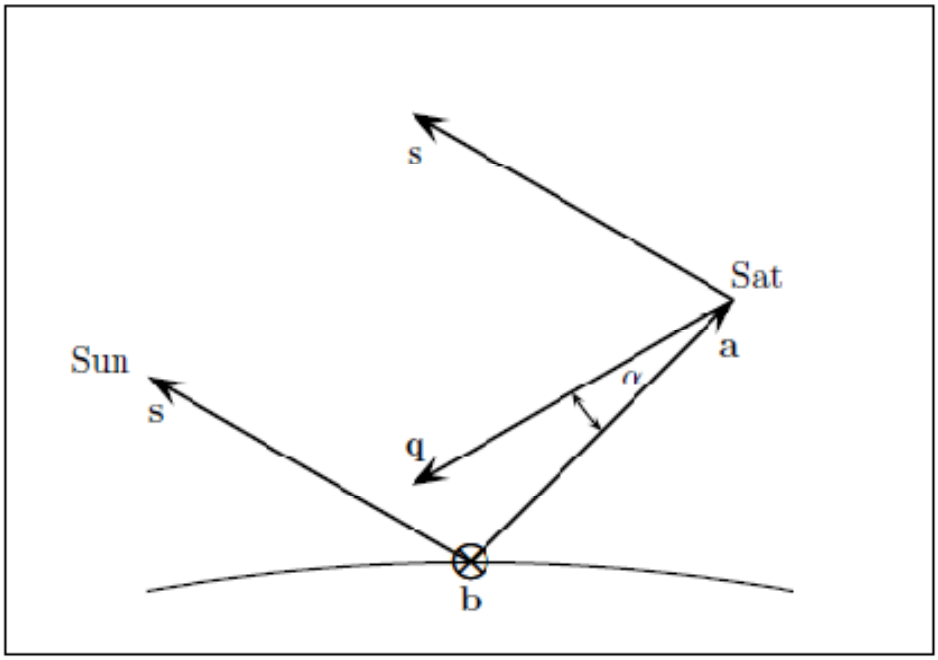

Figure 3-10. Vectors **s** and **a** point from the centre of the target area to the sun and satellite respectively. The vector **b** (pointing into the paper) is parallel to the entrance slit. Vector **q** points from the satellite to the centre of the misaligned target area. The vector **q** is assumed to lie in the plane defined by **s** and **a**.

1. With reference to Figure 3-10, let **a** denote a unit vector from the target centre to the satellite. Ideally this unit vector will be parallel to the bore-sight axis of the instrument (the positive X-axis), but this might not be so.

2. Let **s** denote a unit vector from the target centre to the sun.

3. Let **b** denote a unit vector parallel to the slit axis. In the simulator, it is assumed for nadir and glint modes that **b** is perpendicular to the plane defined by vectors s and **a**, and therefore is given by

$$\mathbf{b} = (\mathbf{s} \times \mathbf{a}) / |\mathbf{s} \times \mathbf{a}| \qquad (3\text{-}38)$$

4. Let **c** complete the right-handed, orthornormal coordinate system containing vectors **a** and **b**,

$$\mathbf{c} = \mathbf{a} \times \mathbf{b} \tag{3-39}$$

5. Again with reference to Figure 3-10, let **q** denote a unit vector that points from the satellite to the centre of the misaligned target area. The assumption of parallel displacement of the slit means that **q** lies in the plane defined by **a** and **s**, and therefore may be represented in the form, $\mathbf{q} = \sin\alpha\,\mathbf{c} - \cos\alpha\,\mathbf{a}$, where α is the angular misalignment.

6. Let $\mathbf{p_n}$ denote a unit vector pointing from the satellite to the centre of footprint *n*. We assume that $\mathbf{p_n}$ lies in the plane defined by the slit axis **b** and the vector **q** that points to the centre of the misaligned target area. Thus,

$$\mathbf{p_n} = \sin\beta_n\,\mathbf{b} + \cos\beta_n\,\mathbf{q}, \tag{3-40}$$

where

$$\beta_n = (n - 4 - 1/2)\,\theta, \quad n = 1, 2, \ldots, 8, \tag{3-41}$$

and 8 θ is the angular width of the field of view along the slit axis. The nominal value of $\theta \sim 0.1°$. Hence,

$$\beta_1, \beta_2, \beta_3, \ldots \beta_8 = -3.5\,\theta, -2.5\,\theta, \ldots +3.5\,\theta. \tag{3-42}$$

7. Let $\mathbf{t}_n$ denote a unit vector pointing from the centre of the earth to the centre of footprint n. Let $\mathbf{k}_n$ denote the normal vector to the reference ellipsoid at $\mathbf{t}_n$.

8. The solar zenith angle, θ_n, at the centre of footprint *n* is the angle between vectors, **s** and $\mathbf{k}_n$,

$$\cos\theta_n = \mathbf{s} \bullet \mathbf{k}_n \tag{3-43}$$

The solar azimuth, ϕ_n, is computed by projecting **s** onto the tangent plane at $\mathbf{t}_n$, and then computing the angle between the projection and the vector pointing north.

9. The zenith angle, θ'_n, and azimuth, ϕ'_n, of the satellite are computed similarly using vector **a** rather than **s**.

10. The components of the Stokes vector reflected to the satellite are specified relative to the plane defined by the local normal vector $\mathbf{k}_n$ at the centre of footprint, *n,* and the vector, $\mathbf{p}_n$, pointing from the satellite to the footprint. However, only photons with parallel polarization in the plane determined by vectors, $\mathbf{p}_n$, and the slit axis, **b**, will be accepted by the polarizer, and hence contribute to the measured signal. Let ϕ_n denote the angle between these two planes, the reference plane for the radiative transfer and the plane of acceptance of the polarizer.

11. Let $\mathbf{u}_n$ denote a unit vector perpendicular to the plane defined by $\mathbf{p}_n$ and $\mathbf{k}_n$,

$$\mathbf{u}_n = (\mathbf{p}_n \times \mathbf{k}_n) / | \mathbf{p}_n \times \mathbf{k}_n | \tag{3-44}$$

Similarly, let $\mathbf{v}_n$ denote a unit vector perpendicular to the plane defined by $\mathbf{p}_n$, and the slit axis, $\mathbf{b}$,

$$\mathbf{v}_n = (\mathbf{p}_n \times \mathbf{b}) / | \mathbf{p}_n \times \mathbf{b} | \tag{3-45}$$

The angle, ϕ, is the angle between vectors $\mathbf{u}_n$ and $\mathbf{v}_n$, given by

$$\cos \phi_n = \mathbf{u}_n \bullet \mathbf{v}_n \tag{3-46}$$

12. Consider Stokes vector in the form, $(I_{||}, I_{\perp}, U, V)$, when the reference plane is defined by $\mathbf{p}_n$ and $\mathbf{k}_n$. Let $(I'_{||}, I'_{\perp}, U', V')$ denote Stokes vector referred to the plane defined by $\mathbf{p}_n$ and $\mathbf{b}$. Chandrasekhar [1950] proves that:

$$\begin{pmatrix} I'_{\|} \\ I'_{\perp} \\ U' \\ V' \end{pmatrix} = \begin{pmatrix} \cos^2\phi_n & \sin^2\phi_n & \frac{1}{2}\sin 2\phi_n & 0 \\ \sin^2\phi_n & \cos^2\phi_n & -\frac{1}{2}\sin 2\phi_n & 0 \\ -\sin 2\phi_n & \sin 2\phi_n & \cos 2\phi_n & 0 \\ 0 & 0 & 0 & 1 \end{pmatrix} \begin{pmatrix} I_{\|} \\ I_{\perp} \\ U \\ V \end{pmatrix}. \tag{3-47}$$

The OCO-2 polarizer accepts only the polarization parallel to the plane defined by $\mathbf{p}_n$ and $\mathbf{b}$, so the measured intensity is given by $I'_{||}$;

$$I'_{||} = \cos^2\phi_n I_{||} + \sin^2\phi_n I_{\perp} + 0.5 \sin 2\phi_n U \tag{3-48}$$

Given that $I = I_{||} + I_{\perp}$ and $Q = I_{||} - I_{\perp}$, this equation reduces to:

$$I'_{||} = 0.5 [I + \cos 2\phi_n Q + \sin 2 \phi_n U]. \tag{3-49}$$

In the special case of (glint) measurements in the principal plane when $\phi_n = \pi/2$, the measured intensity reduces to

$$I'_{||} = 0.5 [I - Q]. \tag{3-50}$$

However, in nadir mode, the polarization angle will vary with the footprint index from near 0° to near 180°.

3.3 State Vector

3.3.1 Basic description of State Vector

A state vector specifies those aspects of the state of the atmosphere being measured, and of the instrument measuring it, which together determine the value of the resulting measurement. We will use the term *state structure* to indicate the complete set of parameters required by the forward model to simulate a measurement to the necessary accuracy, and the term *state vector* to indicate the set of parameters being retrieved. This may be a simple subset of the state structure,

or parameters that describe changes to the state structure (such as an offset to a temperature profile).

The state structure contains all the information about the atmosphere, the surface, the instrument and the sun needed by the forward model as described in the previous section. These are captured in six sub-structures:

- Atmosphere: temperature profile, water vapor profile, surface pressure
- Absorber: gaseous VMR profiles (CO_2, H_2O, O_2, O_3)
- Aerosol: aerosol extinction profiles
- Ground: BRDF parameters – Either albedo at band endpoints or surface wind speed.
- Instrument: spectral dispersion and ILS.
- Solar: parameters of solar continuum model

The state structure is completely flexible and can include an arbitrary number of absorber and aerosol extinction profiles with an arbitrary number of vertical levels. Temperature and gaseous VMR can be retrieved either for each level or by shifting (temperature) or scaling (VMR) the a priori profile.

The state vector for land currently consists of 112 (land) or 107 (water) elements as shown in Table 3-3. It is not currently known whether spectral dispersion (either shift only, or shift + stretch) will be retrieved operationally for each footprint or only verified occasionally.

Table 3-3 Full Physics State Vector.

Description	Parameters	Number of Elements
Aerosols	4 x 20 levels	80
Temperature	Scalar	1
Water Vapor	Scalar	1
Surface Pressure	Scalar	1
Albedo (land)	2 x 3 bands	6
Cox-Munk	1	1
CO_2	20 levels	20
Spectral Dispersion	Shift (+ stretch)	3 (6)
Total		**112 (115) /107 (110)**

Note that the bulk of the retrieval is currently going into constraining profiles of different types of aerosol, and not carbon dioxide, which represents slightly less than 20% of the state vector. In

the next subsection, we describe the initial value and associated uncertainties of each state vector quantity.

3.3.2 The A Priori State Vector and Covariance Matrix

One of the most important factors in any optimal estimation retrieval algorithm is the setup of the a priori values and their corresponding errors, or covariances. They represent our best-guess of the value of a parameter given by our prior knowledge, along with the 1-sigma error of its uncertainty (assuming a Gaussian distribution of errors). When the a priori constraint on a parameter is relatively loose (large a priori covariance), the retrieval relies more on the measurement in order to determine the parameter; conversely when the a priori constraint is tight (small a priori covariance), the less will the measurements affect the retrieved parameter value. The overall a priori covariance matrix is the matrix of error variances and covariances of the a priori values of all state vector parameters; in principle the a priori errors of any two parameters may be correlated.

The retrieval algorithm relies in part on constraining solutions so that they are statistically reasonable. In order to do this, we must have a realistic a priori state vector and covariance matrix which we obtain from model data sets. Note that, for convenience the a priori state vector is also used for the first guess in our retrieval, as it ideally represents our best guess on the state of the atmosphere and surface before taking the OCO-2 observations into account.

The a priori vector is a simple block of parameters with their a priori values. We take the corresponding a priori covariance matrix to be diagonal, with the exception of the carbon dioxide profile block. That is, the a priori uncertainty of every parameter is assumed to be uncorrelated with that of every other parameter, except within the a priori CO_2 profile, in which uncertainties at one vertical level may be correlated with uncertainties at other levels. We now describe the a priori values and assumed uncertainties for each parameter in turn.

3.3.2.1 Profile of Carbon Dioxide Concentration

The a priori profile of CO_2 is derived from a multi-year global run of the LMDZ model. The monthly zonal mean is calculated from the model in 10º latitude bands, separately for land and ocean surfaces. An offset is added to all the model values to make the global average surface value approximately equal to the measured value from GLOBALVIEW-CO2; this offset is to be updated monthly to reflect the increasing concentration of CO_2**.**

The CO_2 covariance submatrix naturally has the most impact on retrieval of X_{CO2}. Currently a single CO_2 covariance matrix is used for all retrievals. This covariance has been constructed by assuming a root-mean-square (rms) variability of X_{CO2} of 12 ppm, which is an estimate of global variability [Dufour and Breon, 2003]. Variability as a function of height is assumed to decrease rapidly, from ~ 10% at the surface to ~1% in the stratosphere. The covariance among altitudes in the troposphere was estimated based on the LMDZ model, but the correlation coefficients were reduced arbitrarily to ensure numerical stability in taking its inverse. The total variability embodied in this covariance is unrealistically large for most of the world (all relatively clean-air sites). It is intended to be a minimal constraint on the retrieved X_{CO2}; the use of a single covariance everywhere at all times eliminates the covariance matrix as a source for variation in retrieval characteristics.

3.3.2.2 Surface Pressure

The a priori surface pressure value is taken from the meteorological data file. Briefly, a horizontal interpolation is done to find the surface pressure for a hypothetical model grid box centered on the instrument field-of-view. Because the elevation of this hypothetical grid box is based on the ECMWF model, it can in principle be different from the actual elevation at the center of the FOV. Thus, a further correction is made based on the hydrostatic equation to account for this elevation difference.

The ECMWF surface pressures are expected to have a 1-sigma error of approximately 1 hPa as they describe a grid-box average (R. Engelen, personal communication). It is unknown what the true error will be when over complex topography at scales of 1-2 km. Currently, the code assumes a 1-sigma error of 4 hPa on the a priori surface pressure estimate.

3.3.2.3 Temperature and Water Vapor

As stated previously, the FP code does not try to retrieve the entire temperature profile in the state vector. Instead it is assumed that the ECMWF forecast temperature profile is correct up to an overall offset. The a priori 1-sigma uncertainty in this offset is taken to be 5 Kelvin. It is likely that there is more information on temperature than just a single number, but thus far retrieval experiments indicate that this temperature assumption is sufficient.

Similar to temperature, the water vapor profile from the ECMWF forecast is assumed to be correct, up to an overall scale factor. This is consistent with the fact that there is not much water vapor information in the OCO-2 spectra, and most of it comes from the strong CO_2 band. Tests thus far indicate that this assumption seems to be justified. We assume a 1-sigma error of 0.5 on the water vapor scale factor, which is probably overly conservative, but will allow the measurements to fully constrain the value.

3.3.2.4 Aerosol Profiles

As stated previously, the full-physics model attempts to retrieve complete profiles of four different aerosol types, the assumption being that more complex distributions of aerosols can be built from a suitable combination of these four fundamental types. Two of the types are traditional aerosol, specifically Kahn types 2b and 3b [Kahn et al., 2001]. The other two types are assumed to be cloud water with an effective radius of 8 microns and cloud ice with an effective radius of 70 microns. The two aerosol types are constrained to live in the lower-mid troposphere, the ice type is constrained to live in the mid-high troposphere, and water clouds can live throughout the entire troposphere.

Each of these aerosol profiles is parameterized in terms of the natural logarithm of the aerosol optical depth (AOD) (at 0.755 microns) per unit pressure. The a priori for each profile is chosen such that the column-integrated optical depths are initially equal among the four types. In order to allow for a better first-guess, one of three initial aerosol profile scenarios is selected; these three scenarios contain total aerosol optical depths of 0.05, 0.15, and 0.25. The particular scenario is chosen based on an initial guess of the total aerosol optical depth which is derived from the AOPD algorithm. The scenario with the closest total aerosol optical depth is selected; for instance, values of 0.1-0.2 would be assigned to the a priori profile scenario with AOD of 0.15. As each of the four aerosol subcomponents have an equal optical depths in each scenario, they are 0.0125, 0.0375, and 0.0625 in the three scenarios, respectively.

Currently, the aerosol error covariance matrix is strictly diagonal. Each individual logarithmic value has a 1-sigma error of 2.3, which essentially means that it can change in either direction by a factor of ten. As all values in the profile for the four aerosol types can do this independently, this gives an incredible amount of leeway to the aerosol profiles during the retrieval.

3.3.2.5 Surface Properties

3.3.2.5.1 Land Surface A priori

Over land, the surface is assumed to be lambertian with a variable slope to the albedo, such that the albedo can vary linearly over each band. This makes for 6 total parameters: one mean albedo and one slope for each of the three bands. It is found that using a more accurate a priori (and hence first-guess) value for the albedo results in a more stable retrieval, as we are starting closer to the correct answer. Therefore, the a priori values for the albedos are selected from the measured continuum radiances in each band, and initially assume zero slope. These mean albedos are constructed using the following standard formula:

$$A = \frac{2\pi I}{\mu_0 I_0} \tag{3-51}$$

where I is the measured radiance in the continuum for a given band, I_0 is the input solar continuum radiance in that band, and μ_0 is the cosine of the solar zenith angle. While this formula does not account for aerosol, it does provide a reasonable good first guess (it is usually correct to about 0.05 of the true albedo). The a priori error on the mean albedo is set wide-open at unity, and the error on the slope is set such that the relative values at the band edges can vary by 50%.

3.3.2.5.2 Ocean Surface A priori in Glint Mode

Over ocean in glint mode, the surface is assumed to be described by a Cox-Munk distribution of planar facets [Cox and Munk, 1954]. The corresponding BRDF is described by the wind speed and index of refraction of the water. The refractive index is taken to be constant within a band, with values of 1.331, 1.318, and 1.303 in the Oxygen-A, weak CO_2, and strong CO_2 bands, respectively. The 1-sigma error on each refractive index is taken to be 0.005, which is fairly tight and reflects the relatively good knowledge of the value of this parameter. Future versions of the code may relax this constraint, and even allow the refractive indices to vary within a band, to allow for more complex ocean surfaces (covered by algae or foam, for instance).

Like the albedo, an estimate of the wind speed is made based directly on the continuum radiance itself. Because the wind speed is a single constant (as opposed to the albedo which varies between the bands), we estimate the value of the wind speed from the weak CO_2 band alone. We take this band because it is the middle of the three bands, Rayleigh scattering is negligible, and biases induced by aerosol hopefully will cancel out among the other two bands.

A semi-empirical model of the wind speed based on the weak CO_2 continuum radiance has been made by model simulations of the three a priori aerosol scenarios at a number of different wind speeds and solar zenith angles. It is assumed that the instrument is looking directly at the glint spot (observation zenith angle equals solar zenith angle); if this is not true, the first guess may have significant errors. The model is as follows:

$$\frac{1}{2\sigma^2} = (0.003 + 0.00512\,W)^{-1} = \frac{I/I_0 - R_{atm}}{R_{surf} - \beta R_{atm}} \tag{3-52}$$

where W is the wind speed in m/s, I_0 is the input solar irradiance, I is the measured continuum radiance, R_{atm} is the solar reflectivity off the atmosphere (due almost entirely to aerosol), and R_{surf} is the solar reflectivity off the surface at the glint angle and includes atmospheric attenuation. σ^2 represents the variance of the slope distribution of the Cox-Munk surface, and the formula for this in terms of wind speed has been taken directly from the original Cox and Munk [1954] work.. β is a parameter whose value depends on which aerosol a priori scenario is used, and is given in Table 3-4. The surface term R_{surf} is well-described by the following relationship:

$$R_{surf} = \frac{\mu_0}{2\pi}\exp(A + B\mu_0^{\alpha})\, e^{-\frac{2\delta}{\mu_0}} \tag{3-53}$$

where A, B, and α are empirically-determined parameters with values A=9.054, B=-14.42, and α=0.355 (these are specific to the weak CO_2 band and it's a priori value of the refractive index). δ is a parameter that represents the atmospheric optical depth; it varies depending on which of the three initial aerosol scenarios is used, with appropriate values given in Table 3-4. Again, μ_0 is the cosine of the solar zenith angle. Finally, an empirical parameterization of R_{atm} based on simulations is given by the exponential of a third order polynomial in μ_0:

$$R_{atm} = \exp\left\{\sum_{n=0}^{3} C_n \mu_0^n\right\} \tag{3-54}$$

where the values the parameters C_n also depend on aerosol scenario and are given by Table 3-4.

These three formulae, along with the parameter values given in Table 3-4, form a complete recipe to obtain a wind speed estimate from the measured radiance continuum. It has been found to generally be good to ± 0.5 m/s, assuming the surface pressure is greater than about 900 hPa, which is always true for the oceans, but not necessarily so for high-altitude lakes. The a priori 1-sigma error is taken to be 3.3 m/s, to give the retrieval sufficient flexibility to converge to a good answer.

Table 3-4 Parameter values for the wind speed initial guess model.

Parameter	AOD 0.05	AOD 0.15	AOD 0.25
δ	0.04	0.12	0.21
β	0.004	0.016	0.016
C_0	-1.452	-0.981	-1.039
C_1	-4.577	-4.925	-3.434
C_2	-7.489	-5.039	-6.336
C_3	6.357	4.560	4.958

3.4 Jacobians

In the inverse method we use, the entire "K-matrix" of the state vector is required, which represents the partial derivative of each spectral channel radiance with respect to each state vector element. Mathematically, this is expressed as

$$K_{ij} = \frac{\partial F_i(\mathbf{x})}{\partial x_j} \tag{3-55}$$

where x_j is the state vector element j and F_i is the forward modeled radiance for channel i. The typical retrieval set-up for OCO-2 has m = 3048 channels and n = 112 state vector elements, meaning that K is a (3048,112) matrix.

We have implemented two methods for computing the K-matrix: Finite difference and analytic. Finite difference is only using for validation of the analytic Jacobians, where are much faster to calculate and hence are what is used operationally.

3.4.1 Finite Difference

In the finite difference approach, the radiance is calculated for the base state and then for a perturbed state. The Jacobian is computed using the finite difference between the two

$$K = \frac{\partial F(x)}{\partial x} \cong \frac{F(x+\Delta x) - F(x)}{\Delta x} \tag{3-56}$$

where K is the Jacobian, x is the parameter being perturbed and Δx is the perturbation step size.

This technique is very time-consuming since a large number of forward model calculations have to be carried out. A higher efficiency can be achieved by calculating analytic Jacobians. The finite-difference Jacobians can be seen as an accurate standard which enables validating Jacobians calculated with other techniques. It should be noted that Jacobians don't have to be as accurate as the simulated spectrum itself and small errors may be acceptable.

3.4.2 Analytic

Finite difference methods require an additional forward-model call for each elements of the state vector. Because our state vector typically has greater than 100 elements, this results in a large calculational burden. However, an internal perturbation analysis can be performed to simultaneously compute the Jacobian along with the base state radiances. Clearly, this tremendously reduces computation time, since the evaluation of the Jacobian in the finite difference method takes more than 80% of the total CPU time. In addition, this technique also guarantees numerical stability since it does not depend on the perturbation step size.

Our state vector can roughly be divided into three categories: atmospheric parameters, surface parameters, and instrument parameters. Derivatives with respect to atmospheric parameters are the most difficult, and we focus the bulk of the following discussion on their computation.

3.4.2.1 Derivatives with respect to atmospheric parameters

Atmospheric parameters in the state vector are carbon dioxide concentration (on levels), water vapor multiplier, temperature offset, aerosol concentration (on levels), and surface pressure. However, within the forward model, these quantities are at some point converted to CO_2 profile (on layers), temperature (on layers), water vapor concentration (on layers), and aerosol optical depth per layer (and per aerosol type). First we describe the computation of these layer-based derivatives; then a simple application of the chain rule allows them to be computed to the desired state vector quantity.

It is important to remember that within the forward model, atmospheric quantities are first converted to optical properties; then high-resolution (monochromatic) radiances are computed from the optical properties via our RT module. A general way of thinking about a call to the RT module is as follows:

$$S_\lambda = RT(\vec{\tau}, \vec{\omega}, PM, s) \tag{3-57}$$

where $\vec{\tau}$ is a vector of the profile composite optical depths, $\vec{\omega}$ is a vector of the profile composite single-scattering albedo, *PM* represents the composite phase matrix for each atmospheric layer, and *s* represents all the relevant surface parameters. Each of these four quantities is an implicit function of wavelength. Finally, the returned quantity S_λ represents the 3 stokes parameters: {*I, Q, U*} at monochromatic wavelength λ. Our analytic Jacobians are intimately tied to the way Jacobians are produced within the RT module.

This RT module is "linearized": it can compute changes to the output S_λ, for a set of input atmospheric or surface changes. The special thing about our RT code is that it can do this for each atmospheric layer simultaneously.

3.4.2.1.1 Composite Optical Properties

Before going further, it is important to write down the composite atmospheric optical properties. The following equations are meant to apply to a particular layer and monochromatic wavelength. The composite optical depth for a layer is calculated as the sum of several components:

$$\tau = \tau_g + \tau_R + \tau_a + \tau_b \tag{3-58}$$

where *g* stands for gas absorption, *R* represents Rayleigh scattering, and *a* and *b* represent two types of aerosol; this method can be easily extended to any number of aerosol types. The composite single scattering albedo is given by

$$\omega = \frac{\tau_R + \omega_a \tau_a + \omega_b \tau_b}{\tau} \tag{3-59}$$

where we make use of the fact that the single scattering albedo of Rayleigh scattering is by definition unity. Finally, the composite phase matrix is:

$$PM = \frac{PM_R \tau_R + PM_a \omega_a \tau_a + PM_b \omega_b \tau_b}{\tau_R + \omega_a \tau_a + \omega_b \tau_b} \tag{3-60}$$

With these basic equations in mind, let us begin to construct the partial derivatives of the monocrhomatric Stokes parameters with respect to various quantities related to state vector elements.

3.4.2.1.2 Carbon Dioxide & Water Vapor

The concentration of carbon dioxide (or any other gas excepting water vapor) only affects the Stokes parameters through the gas absorption τ_g for each layer in the atmosphere. Through equations (3-58) and (3-59), above, a change in τ_g will affect both the composite optical depth and the composite single scattering albedo. Therefore:

$$\frac{\partial S_\lambda}{\partial \tau_{g,i}} = \frac{\partial S_\lambda}{\partial \tau_i}\frac{\partial \tau_i}{\partial \tau_{g,i}} + \frac{\partial S_\lambda}{\partial \omega_i}\frac{\partial \omega_i}{\partial \tau_{g,i}} \tag{3-61}$$

where *i* denotes the layer index. The derivative terms $\frac{\partial S_\lambda}{\partial \tau_i}$ and $\frac{\partial S_\lambda}{\partial \omega_i}$ are provided by the RT module. The other two terms are calculated simply from equations (3-58) and (3-59), leading to:

$$\frac{\partial S_\lambda}{\partial \tau_{g,i}} = \frac{\partial S_\lambda}{\partial \tau_i} - \frac{\partial S_\lambda}{\partial \omega_i}\frac{\omega_i}{\tau_i} \tag{3-62}$$

Equations (3-61) and (3-62) together thus provide derivatives of each Stokes S_λ with respect to the gas optical depth for each layer. In order to obtain the Jacobian for gas concentration on a level *j*, we use the fact that this concentration only affects the optical depths of the layers above and below it. Therefore:

$$\frac{\partial S_\lambda}{\partial x_j} = \sum_{i=j-1}^{j} \frac{\partial S_\lambda}{\partial \tau_{g,i}}\frac{\partial \tau_{g,i}}{\partial x_j} \tag{3-63}$$

where *i* is the layer index and runs over the two layers than border the level *j*; in the case of the top and bottom boundaries, it runs over a the single bordering layer. X_i therefore represents the gas concentration on a level *j*, and could represent either carbon dioxide or water vapor. The terms $\frac{\partial \tau_{g,i}}{\partial x_j}$ are calculated analytically within the gas absorption module.

Finally, for water vapor there should be an additional dependence with regard to Rayleigh scattering. However, as we ignore this in the calculation of Rayleigh optical depth itself, it is also ignored for the calculation of the water vapor Jacobian.

3.4.2.1.3 Temperature

The derivative of the Stokes parameters with respect to temperature, also specified on levels, is calculated in a virtually identical way to that of gas concentration. As for water vapor, the Rayleigh temperature dependence is ignored. Therefore, we use equations (3-61) and (3-62) again to obtain the partials with respect to gas optical depth τ_g for each layer, and a modified version of equation (3-63) to connect to the temperature on level *j*:

$$\frac{\partial S_\lambda}{\partial T_j} = \sum_{i=j-1}^{j} \frac{\partial S_\lambda}{\partial \tau_{g,i}} \frac{\partial \tau_{g,i}}{\partial T_j} \tag{3-64}$$

The derivative terms $\frac{\partial \tau_{g,i}}{\partial T_j}$ are calculated analytically within the gas absorption module.

3.4.2.1.4 Surface Pressure

A change in the surface pressure will cause all four optical depth terms from equation (3-58) to change. However, the change in the Rayleigh term τ_R as well as the aerosol terms τ_a and τ_b depend linearly on the pressure width of the lowest atmospheric layer. Let this pressure width be

$$\Delta P_n = P_s - P_n \tag{3-65}$$

where P_s is the surface pressure and P_n is the (fixed) pressure of atmospheric level n. Then we can write

$$\tau_R = C_R \Delta P_n \tag{3-66}$$

where C_R is a constant that determines the Rayleigh scattering in the surface layer. The same form of equation (3-64) holds true for the aerosol optical depths, τ_a and τ_b, as well. Therefore, an extremely nice simplification is that the composite phase function *does not depend on surface pressure*. This is because all the τ terms in equation (3-60) contain ΔP_n terms which cancel out.

However, the same does not hold true for the composite single scattering albedo ω. Its dependence can be shown to be:

$$\frac{\partial \omega_n}{\partial P_s} = \frac{\omega_n}{\tau_n}\left(\frac{\tau_n}{\Delta P_n} - \frac{\partial \tau_n}{\partial P_s}\right) \tag{3-67}$$

where all subscripts n refer to the lowest atmospheric layer. The dependence of the total optical depth in the lowest layer can be shown to be:

$$\frac{\partial \tau_n}{\partial P_s} = \frac{\partial \tau_{g,n}}{\partial P_s} - \frac{(\tau_n - \tau_{g,n})}{\Delta P_n} \tag{3-68}$$

The term $\frac{\partial \tau_{g,n}}{\partial P_s}$ is calculated internally in the code by simple finite differencing (though a future version will change to a fully analytic calculation). Finally, using the chain rule, the total dependence of Stokes S_λ on surface pressure P_s is given by

$$\frac{\partial S_\lambda}{\partial P_s} = \frac{\partial S_\lambda}{\partial \tau_n}\frac{\partial \tau_n}{\partial P_s} - \frac{\partial S_\lambda}{\partial \omega_n}\frac{\partial \omega_n}{\partial P_s} \tag{3-69}$$

3.4.2.1.5 Aerosol concentration per type

So far, we have been lucky in that we've only needed partial derivatives of monochromatic Stokes parameters with respect to composite optical depth and composite single scattering albedo on each layer, which are easily calculated within the RT code. This is because the composite

phase matrix has not yet had any dependence on any of the variables of interest. Unfortunately, the situation changes with aerosols; when the concentration of a particular aerosol is changed, its optical depth is changed, which via equation (3-60) changes the composite phase matrix. Let us first find the derivative of S_λ with respect to the aerosol optical depth (for a particular type). Because all three composite parameters depend on τ_a, we have

$$\frac{\partial S_\lambda}{\partial \tau_a} = \frac{\partial S_\lambda}{\partial \tau}\frac{\partial \tau}{\partial \tau_a} + \frac{\partial S_\lambda}{\partial \omega}\frac{\partial \omega}{\partial \tau_a} + \sum_{p=1}^{6}\sum_{l=0}^{l_{\max}} \frac{\partial S_\lambda}{\partial PM_{l,p}}\frac{\partial PM_{l,p}}{\partial \tau_a} \tag{3-70}$$

where it is implicit that all terms (except S_λ) are with respect to a given layer i. Differentiating equations (3-58)-(3-60) with respect to τ_a yields

$$\frac{\partial S_\lambda}{\partial \tau_a} = \frac{\partial S_\lambda}{\partial \tau} - \frac{\omega}{\tau}\frac{\partial S_\lambda}{\partial \omega} + \sum_{p=1}^{6}\sum_{l=0}^{l_{\max}} \frac{\partial S_\lambda}{\partial PM^{l,p}}\frac{\omega_a(PM_a^{l,p} - PM^{l,p})}{\omega\tau} \tag{3-71}$$

where the index l refers to phase function expansion moment and p refers to one of the six polarization components in the phase matrix PM. As stated previously, the partial derivatives of S_λ with respect to composite variables τ and ω are calculated within the RT code. However, calculating all 6 * l_{max} is highly impractical. Fortunately, because the RT code is linearized, it takes a linear perturbation of all parameters simultaneously. Therefore, if the linear perturbations for optical depth and single scattering albedo are set to zero, and the linear perturbations to the phase matrix are set to $\frac{\omega_a(PM_a^{l,p} - PM^{l,p})}{\omega\tau}$ for each legendre moment l and polarization component p, then the RT code will return precisely the last term (with the double summation) in equation (3-71).

To obtain the derivative with respect to aerosol concentration on a level, we must go through a similar procedure as was done for gas concentration and temperature.

$$\frac{\partial S_\lambda}{\partial C_{a,j}} = \sum_{i=j-1}^{j} \frac{\partial S_\lambda}{\partial \tau_{a,i}}\frac{\partial \tau_{a,i}}{\partial C_{a,j}} \tag{3-72}$$

Where $C_{a,j}$ represents the aerosol concentration on level j for type a, and the summation is over the two neighboring layers i. Finally, if we are retrieving the logarithm of the aerosol concentration (as we often are), a final step is necessary:

$$\frac{\partial S_\lambda}{\partial \ln C_{a,j}} = C_{a,j}\frac{\partial S_\lambda}{\partial C_{a,j}} \tag{3-73}$$

3.4.2.1.6 Number of Jacobians & the adjoint alternative

We can express the efficiency with which the K-matrix is obtained in terms of how fast the forward model calculations are with and without Jacobians. This is primarily determined by the "number of atmospheric Jacobians" calculated within the RT module (remember that it does all layers independently and simultaneously). For our work, we need two Jacobians for the optical depth and single scattering albedo, and an additional atmospheric Jacobian for each aerosol type. Nominally using four aerosol types, this leads to six total atmospheric Jacobians, which

essentially means that the calculations with Jacobians take ~ 7 times as long as with no Jacobians; call this 7X.

There is potential time savings to be had if an adjoint of our RT module were available; adjoints are run after the forward model run, and typically take about 3 times as long as the forward model run. Thus an adjoint method could run in 4X, or close to twice as fast as our current formulation. However, because of the extreme difficulty in actually coding an adjoint method, this option is unlikely to be pursued in the near future.

3.4.2.2 Derivatives with respect to surface parameters

The full-physics code currently runs with two types of surfaces: over land, a Lambertian surface is assumed, while over ocean a pure Cox-Munk surface is assumed.

3.4.2.2.1 Lambertian Albedo

Over land, a Lambertian surface is retrieved with an albedo A_λ that varies linearly with wavelength λ over a given OCO-2 band:

$$A_\lambda = A_0 + B(\lambda - \lambda_0) \tag{3-74}$$

where A_0 is the albedo at λ_0 and B is the albedo slope. For a given monochromatic wavelength, the RT module calculates $\frac{\partial S_\lambda}{\partial A_\lambda}$, the partial derivative of Stokes S_λ with respect to the albedo at wavelength λ. Using the chain rule, the derivatives with respect to the two albedo parameters are given by:

$$\frac{\partial S_\lambda}{\partial A_0} = \frac{\partial S_\lambda}{\partial A_\lambda} \tag{3-75}$$

$$\frac{\partial S_\lambda}{\partial B} = \frac{\partial S_\lambda}{\partial A_\lambda}(\lambda - \lambda_0) \tag{3-76}$$

3.4.2.2.2 Cox & Munk Surface

Our Cox-Munk surface is determined primarily by four parameters: the wind speed, and the refractive index in each of the three bands. Using a similar methodology to that for land surfaces, the partial derivatives of S_λ are easily determined.

3.4.2.3 ILS Convolution

Once the derivatives of the monochromatic wavelengths are determined, it is straightforward to run them through the instrument model in order to determine their effect on measured radiances. First the measured high-resolution radiance is constructed as a simple linear combination of Stokes parameters using the Mueller matrices multiplied by the solar irradiance; for nadir and glint mode, this is simply

$$I_{meas,\lambda} = \frac{I_\lambda - Q_\lambda}{2} s_\lambda \tag{3-77}$$

where s_λ denotes the solar irradiance. The convolution to construct a given channel m is

$$I_m = \int I_{meas,\lambda} ILS_m(\lambda) d\lambda = \frac{\sum_i I_{meas,\lambda_i} ILS_m(\lambda_i) \Delta\lambda_i}{\sum_i ILS_m(\lambda_i) \Delta\lambda_i} \tag{3-78}$$

where the term in the denominator ensures proper normalization. Equation (3-78) can be recast as:

$$I_m = \sum_i w_{m,i} I_{meas,\lambda_i} \tag{3-79}$$

where the weight terms $w_{m,i}$ are calculated easily from (3-78). To determine the partial derivative of any parameter x is then simply a summation over a different variable:

$$\frac{\partial I_m}{\partial x} = \sum_i w_{m,i} \frac{\partial I_{meas,\lambda_i}}{\partial x} \tag{3-80}$$

In order to construct derivatives of variables such as water vapor scale factor and temperature offset, another application of the chain rule is simply required. For instance, in the case of temperature, we assume the true profile is the a priori profile plus an offset:

$$T_j = T_{ap,j} + \Delta T \tag{3-81}$$

Therefore, the Jacobian for ΔT is requires a simple sum of the derivatives with respect to level temperature T_j over all atmospheric levels j

$$\frac{\partial I_m}{\partial \Delta T} = \sum_j \frac{\partial I_m}{\partial T_j} \tag{3-82}$$

3.5 Inverse Method

3.5.1 Formulation and implementation

As mentioned in the algorithm overview section, the notation and concepts of Rodgers [2000] are employed for the inverse method. This section builds on section 2.1 of Connor et al. [2008]. The spectrum, or measurement vector **y**, is expressed symbolically as **y = F(x) + ε** where **x** is the state vector, **F** is the forward model, and **ε** is the vector of spectral errors due to the measurement and forward model.

The solution of the OCO-2 inverse method is the state vector $\hat{\boldsymbol{x}}$ with maximum *a posteriori* probability, given the measurement **y.** Our inverse method employs the Levenberg-Marquardt modification of the Gauss-Newton method.

The operational inverse method consists of a set of routines which are essentially mathematical and independent of the physics embodied by the measurement and state vectors. This implies that the structure of both vectors may be varied, so the routines are readily applied to other

experiments, such as SCIAMACHY or ground-based FTS [Boesch et al, 2006]. The ability to retrieve X_{CO2} from space-based and ground-based measurements using the same algorithm is critical for detecting and removing biases from the space-based data and forms a critical component of the OCO-2 validation strategy [Crisp et al., 2004].

The result of the inverse method is classified according to the parameter 'outcome', as follows:

Outcome	Description
1	convergence was reached and the spectral fit was consistent with assumed uncertainties
2	convergence was reached but the spectral fit was poor relative to assumed uncertainties
3	convergence was not reached in the maximum allowed number of iterations
4	the maximum number of diverging steps (described below) was exceeded

To find the state vector that produces the maximum a-posteriori probability, we minimize the following standard cost function χ^2:

$$\chi^2 = (\mathbf{y} - \mathbf{F(x)})^T \mathbf{S_\varepsilon}^{-1} (\mathbf{y} - \mathbf{F(x)}) + (\mathbf{x_a}-\mathbf{x})^T \mathbf{S_a}^{-1}(\mathbf{x_a} - \mathbf{x}) \quad (3\text{-}83)$$

where $\mathbf{K} = \frac{\partial \mathbf{F(x)}}{\partial \mathbf{x}}$ is the weighting function matrix, or Jacobian, $\mathbf{x_a}$ is the a priori state vector, $\mathbf{S_a}$ is the a priori covariance matrix, $\mathbf{S_\varepsilon}$ is the measurement covariance matrix. On each iteration *i*, we solve for the state vector update $\mathbf{dx_{i+1}}$, using a slightly modified form of Rodgers' Eq. 5.36, to improve numerical accuracy by avoiding inversion of a large matrix:

$$(\,(1+\gamma)\mathbf{S_a}^{-1} + \mathbf{K_i}^T \mathbf{S_\varepsilon}^{-1} \mathbf{K_i}\,)\ \mathbf{dx_{i+1}} = [\mathbf{K_i}^T \mathbf{S_\varepsilon}^{-1} (\mathbf{y} - \mathbf{F(x_i)}) + \mathbf{S_a}^{-1}(\mathbf{x_a} - \mathbf{x_i})] \quad (3\text{-}84)$$

where γ is the Levenberg-Marquardt parameter. This method reduces to regular Gaussian Newton minimization when $\gamma = 0$. γ is initialized with a value of 10.0.

After each calculation of $\mathbf{dx_{i+1}}$, before using it to update $\mathbf{x_i}$, we assess the impact of forward model nonlinearity on the reduction in the cost function. To do this, we calculate the following quantity:

$$R = \frac{\chi_i^2 - \chi_{i+1,FC}^2}{\chi_i^2 - \chi_{i+1}^2} \quad (3\text{-}85)$$

This is simply the ratio of the actual reduction in the cost function χ^2 (between iterations *i* and *i+1*) to the forecast reduction in the cost function based on an assumption of linearity. For a perfectly linear forward model, the cost function reduction will equal the forecast cost function reduction, and *R* will equal unity. A step in which the cost function actually increases will yield $R < 0$. Cases for which $0 < R < 1$ are cases for which the cost function decreased, but not by as much as expected. Cases with $R < 0.25$ are labeled diverging steps; if the total number of

diverging steps passes a certain threshold, the entire retrieval is abandoned, and 'outcome' is set = 4.

Cases with $R >= 0.25$ are deemed non-diverging steps. Those cases with $R > 0.75$ are deemed quite linear and in these cases the Levenberg-Marquardt parameter γ is reduced by a factor of two. For non-diverging steps with $R < 0.75$, γ is left unchanged.

After each successful, non-divergent iteration, we further test for convergence. To facilitate that, we compute the error variance derivative

$$d\sigma_i^2 = \mathbf{dx_{i+1}}^T \hat{\mathbf{S}}^{-1} \mathbf{dx_{i+1}} \tag{3-86}$$

where $\hat{\mathbf{S}}$ denotes the covariance of the retrieved state, using the relation

$$\hat{\mathbf{S}}^{-1} \mathbf{dx_{i+1}} \cong [\mathbf{K_i}^T \mathbf{S_\varepsilon}^{-1} (\mathbf{y} - \mathbf{F(x_i)}) + \mathbf{S_a}^{-1}(\mathbf{x_i} - \mathbf{x_a})] \tag{3-87}$$

and dx_{i+1} is the state vector update assuming $\gamma = 0$ (this is generally larger than the actual step size dx_{i+1} computed for nonzero γ). $d\sigma_i^2$ is effectively the square of the state vector update in units of the solution variance.

If $d\sigma_i^2 <$ fn (where n is the number of state vector elements, and f ~1), convergence is reached. We then update the state vector a final time.

Lastly, we compute the retrieval covariance matrix, $\hat{\mathbf{S}}$, and the averaging kernel matrix **A.** $\hat{\mathbf{S}}$ is given by

$$\hat{\mathbf{S}} = (\mathbf{K}^T \mathbf{S}_\varepsilon^{-1} \mathbf{K} + \mathbf{S}_a^{-1})^{-1} \tag{3-88}$$

The averaging kernel matrix **A** is given by

$$\mathbf{A} = \hat{\mathbf{S}} \mathbf{K}^T \mathbf{S}_\varepsilon^{-1} \mathbf{K} \tag{3-89}$$

Finally, the degrees of freedom for signal are given by the trace of the matrix **A**; the degrees of freedom for the CO_2 profile are the trace of the CO_2-only sub-matrix.

We note that the OCO-2 retrieval problem as described is underdetermined. There are typically 1.0 – 1.5 degrees of freedom for the CO_2 profile (compared to 20 profile levels) and ~ 20 total degrees of freedom (compared to ~100 elements). However, the use of an a priori constraint guarantees that the problem is well posed and well conditioned. Although there is little more than one degree of freedom for the CO_2 profile, and thus little ability to discriminate between altitudes, the profile, rather than just the CO_2 column, is formally retrieved. This is to allow for the large variations of CO_2 in the boundary layer; such variations can produce bias in the results if a fixed profile shape is used in the retrieval.

3.5.2 Goodness of Spectral Fit

The goodness of fit is determined from chi-squared, i.e. the ratio of the mean square of measured minus calculated spectra to the mean square of the spectral errors, χ^2_i, for each spectral band i. If $\chi^2_i <$ max_chi2 $\forall$ i, then the fit is acceptable, and 'outcome' is set = 1; otherwise, outcome = 2.

3.6 X_{CO2}, Characterization, and Error Analysis

3.6.1 Pressure Weighting Function

We define the pressure weighting function **h** to relate the local CO_2 mixing ratio values specified on the discrete pressure levels to the profile-weighted average such that $X_{CO2} = \mathbf{h}^T \hat{\mathbf{x}}$. Recalling that X_{CO2} is defined as the CO_2 column divided by the dry air column, it may be seen that the vector **h** represents the pressure intervals assigned to the state vector levels, normalized by the surface pressure and corrected for the presence of water vapor such that $\hat{\mathbf{x}}$ is weighted by the number of moles of dry air per layer.

In order to calculate **h**, we must both relate the column of any gas to its dry mixing ratio profile, and the pressure interval in each layer must be conceptually divided by assigning fractions of it to the two adjacent levels, in such a way that integrating over all levels conserves both total pressure and CO_2 column.

The column of gas X may be shown to be given by

$$C_X = \sum_i \frac{u_i^X}{g_i \, m_{air}\left(1 + u_i^{H2O} \times m_{H2O}/m_{air}\right)} \Delta p_i \tag{3-90}$$

where u_i is the mixing ratio on level i, Δp_i is the pressure interval assigned to that level, g is the local acceleration due to gravity, and m_x is the molecular weight of gas x.

Combining Eq (3-90) with the definition of **h** implies that

$$h_i = \frac{\left(g_i \, m_{air}\left(1 + u_i^{H2O} \times m_{H2O}/m_{air}\right)\right)^{-1} \Delta p_i}{\sum_i \left(g_i \, m_{air}\left(1 + u_i^{H2O} \times m_{H2O}/m_{air}\right)\right)^{-1} \Delta p_i} \tag{3-91}$$

Appendix A of Connor et al. [2008] details the calculation assigning pressure intervals to atmospheric levels. From Eq (A7) it may be seen that

$$\Delta p_i = \left| \left(-p_i + \frac{p_{i+1} - p_i}{\ln(p_{i+1}/p_i)}\right) + \left(p_i - \frac{p_i - p_{i-1}}{\ln(p_i/p_{i-1})}\right) \right| \tag{3-92}$$

where we have kept the two terms separated for ease of calculating the edge layers. Note that if p decreases with increasing i, h_i is formally negative, thus we have taken the absolute value.

Equation (3-91) applies to the calculation of **h** for elements h_i, for i =1, q, where q is the number of levels. By definition, $h_i = 0$, for i = q+1, n, where n is the number of elements in the state vector.

3.6.2 X_{CO2}

Finally, X_{CO2} and its uncertainty σ_{XCO2} are calculated. The CO_2 dry air mole fraction, X_{CO2}, is obtained by averaging the CO_2 profile, weighted by the pressure weighting function, **h**, such that $X_{CO2} = \mathbf{h}^T \hat{\mathbf{x}}$. The formal error variance in the retrieved X_{CO2} is therefore given by $\sigma^2_{XCO2} = \mathbf{h}^T \hat{\mathbf{S}}\, \mathbf{h}$.

A series of standard error analysis calculations are performed as part of each retrieval to characterize the retrieval results and quantify their uncertainties. The retrieval uncertainties and averaging kernels are calculated from the measurement Jacobian, **K** of section 3.5.1, evaluated at the retrieved state, the measurement covariance matrix, and the a priori covariance matrix. From these we compute the column averaging kernel, $\mathbf{a_{CO2}}$, the uncertainty due to smoothing and interference, $\tilde{\mathbf{a}}_\mathbf{c}$, the correlation of non-CO_2 state vector elements to X_{CO2}, $\tilde{\mathbf{s}}_1$, and the components of X_{CO2} variance due to measurement error, smoothing, and interference. These last six quantities are defined and discussed below. A complete list of operational retrieval products is given in Table 3-5.

3.6.3 The column averaging kernel, $\mathbf{a_{CO2}}$

Let $\hat{\mathbf{u}}$ be the retrieved CO_2 mixing ratio profile, and $\hat{\mathbf{e}}$ be the retrieved vector of all non-CO_2 quantities, i.e.

$$\hat{\mathbf{x}} = \begin{pmatrix} \hat{\mathbf{u}} \\ \hat{\mathbf{e}} \end{pmatrix} \tag{3-93}$$

and let

$$\mathbf{A}_{ij} = \frac{\partial \hat{\mathbf{x}}_i}{\partial \mathbf{x}_j} \quad i, j = 1,n \tag{3-94}$$

so

$$\frac{\partial X_{CO2}}{\partial \mathbf{x}_j} = (\mathbf{h}^T \mathbf{A})_j \tag{3-95}$$

Now consider only the CO_2 part of the state vector, the first q elements u_i , i=1 to q and define the column averaging kernel

$$(\mathbf{a}_{CO2})_j = \frac{\partial X_{CO2}}{\partial \mathbf{u}_j} \frac{1}{\mathbf{h}_j} = (\mathbf{h}^T \mathbf{A})_j \frac{1}{\mathbf{h}_j} \tag{3-96}$$

The column averaging kernel $\mathbf{a}_{CO2}$ has the property that its elements all equal 1 in the 'ideal' case, where the retrieved X_{CO2} responds to changes in **u** exactly as the true value of the profile-weighted mixing ratio. For a real retrieval, the elements of $\mathbf{a}_{CO2}$ may be more or less than 1, and will have values much less than 1 in regions where the a priori CO_2 profile is important.

3.6.4 Smoothing and interference due to the state vector, $\tilde{\mathbf{a}}_c$

The vector $\tilde{\mathbf{a}}_c$ captures the smoothing and interference (or 'cross-talk') errors in X_{CO2} due to each element of $\hat{\mathbf{x}}$. Thus, $\tilde{\mathbf{a}}_c$ reveals the sensitivity of the retrieved X_{CO2} value to uncertainties in elements of the state vector. It may be derived from the full averaging kernel matrix as follows.

The error in X_{CO2} is given by

$$\Delta X_{CO2} = \mathbf{h}^T(\hat{\mathbf{x}} - \mathbf{x}) = \mathbf{h}^T(\mathbf{A}_{uu} - \mathbf{I})(\mathbf{u} - \mathbf{u_a}) + \mathbf{h}^T\mathbf{A}_{ue}(\mathbf{e} - \mathbf{e_a}) + \varepsilon_u \tag{3-97}$$

Eq. (3-97) is an adaptation of Eq. (7) in Rodgers and Connor [2003]. The first term in Eq.(3-97) represents smoothing error, the second interference error, and ε_u all other sources of error. Here $\mathbf{A}_{uu}$ and $\mathbf{A}_{ue}$ are submatrices of $\mathbf{A}$, representing the CO_2-only component and the cross-talk components (those which mix elements of the CO_2 profile $\mathbf{u}$ and the non-CO_2 elements $\mathbf{e}$), respectively. $\mathbf{I}$ is the identity matrix.

It follows that the error in X_{CO2} due to each state vector element is given by

$$\tilde{\mathbf{a}}_{c,j} = \begin{cases} \mathbf{h}^T(\mathbf{A} - \mathbf{I})\sigma_j, \; j = 1, q \\ \mathbf{h}^T\mathbf{A}\sigma_j, \; j = q+1, n \end{cases} \tag{3-98}$$

where σ_j is the error in element j. Since $h_j \equiv 0$ for $j > q$, the full matrix $\mathbf{A}$ may be used in place of the submatrices in Eq (3-97).

Alternatively, (3-98) may be written

$$\tilde{\mathbf{a}}_{c,j} = \begin{cases} (\dfrac{\partial X_{CO2}}{\partial \mathbf{u}_j} - \mathbf{h}_j)\sigma_j = (\mathbf{a}_{CO2,j} - 1)\mathbf{h}_j\sigma_j, j = 1, q \\ \dfrac{\partial X_{CO2}}{\partial \mathbf{e}_j}\sigma_j, j = q+1, n \end{cases} \tag{3-99}$$

The first q elements of $\tilde{\mathbf{a}}_c$, corresponding to the CO_2 profile, are components of the smoothing error. The remaining elements represent the interference, or cross-talk error.

3.6.5 Correlation of X_{CO2} with non-CO_2 state vector elements, $\tilde{\mathbf{s}}_1$

We define $\tilde{\mathbf{s}}_1$, the correlation of X_{CO2} with the state vector elements, to aid the diagnosis and understanding of cross-talk. Define a matrix $\mathbf{H}$ with dimension $n \times (n+1)$ such that

$$\mathbf{H}_{ij} = \begin{cases} \mathbf{h}_i, j = 1 \\ 1, i = j - 1, j > 1 \\ 0, else \end{cases} \tag{3-100}$$

Thus

$$\mathbf{H}^{\mathrm{T}}\hat{\mathbf{x}} = \begin{pmatrix} X_{CO2} \\ x_1 \\ x_2 \\ \bullet \\ \bullet \\ x_n \end{pmatrix} \tag{3-101}$$

and the correlation matrix of $\mathbf{H}^{\mathrm{T}}\hat{\mathbf{x}}$ is given by $\mathbf{H}^{\mathrm{T}}\hat{\mathbf{C}}\,\mathbf{H}$, where $\hat{\mathbf{C}}$ is the correlation matrix corresponding to $\hat{\mathbf{S}}$.

$\tilde{\mathbf{s}}_1$ is the first row of $\mathbf{H}^{\mathrm{T}}\hat{\mathbf{C}}\,\mathbf{H}$, where $\tilde{\mathbf{s}}_1 = (\,1 \;\; \rho_{XCO2,j} \ldots)$ for j = 1, *n*. The second and subsequent elements of $\tilde{\mathbf{s}}_1$ are the correlation coefficients of X_{CO2} with each element of the state vector.

3.6.6 Components of X_{CO2} Variance

In Section 3.6.2 above, the variance in X_{CO2} is given as

$$\sigma^2_{XCO2} = \mathbf{h}^T\hat{\mathbf{S}}\mathbf{h} \tag{3-102}$$

for pressure weighting function **h** and a posteriori error covariance $\hat{\mathbf{S}}$. We also calculate the component parts of the variance, as described next.

In Eq 3.16 of Rodgers [2000], the total error is broken up into measurement, smoothing, and forward model error (which includes both radiative transfer and the instrument). The operational L2 code has no explicit information on forward model error, though it may be implicitly included in the measurement error estimate provided as input. Formally then, we separate the error into measurement and smoothing components. Further, smoothing due to the full state vector may logically be separated into smoothing due to CO_2 itself and interference due to non-CO_2 elements, as described in Rodgers and Connor [2003]. Thus we calculate variance components due to spectral error (measurement and implicit model error), smoothing (due to CO_2), and interference.

First, define the contribution function as

$$\mathbf{G}_\mathbf{y} = \hat{\mathbf{S}}\mathbf{K}^{\mathbf{T}}\mathbf{S}_\varepsilon^{-1} \tag{3-103}$$

Then the measurement error covariance is

$$\hat{\mathbf{S}}_\mathbf{m} = \mathbf{G}_\mathbf{y}\mathbf{S}_\varepsilon\mathbf{G}_\mathbf{y}^{\mathbf{T}} \tag{3-104}$$

the smoothing error due to CO_2 is

$$\hat{\mathbf{S}}_\mathbf{s} = (\mathbf{A}_{\mathbf{CO2}} - \mathbf{I})\mathbf{S}_{\mathbf{a,CO2}}(\mathbf{A}_{\mathbf{CO2}} - \mathbf{I})^{\mathbf{T}} \tag{3-105}$$

and the interference error is

$$\hat{\mathbf{S}}_\mathbf{i} = \mathbf{A}_{\mathbf{ue}}\mathbf{S}_{\mathbf{ae}}\mathbf{A}_{\mathbf{ue}}^{\mathbf{T}} \tag{3-106}$$

where subsets of the averaging kernel **A** and a priori covariance $\mathbf{S_a}$ are defined as follows:

$$\mathbf{A_{CO2} = A(1:nz, 1:nz)} \qquad \text{for nz = \# levels in } CO_2 \tag{3-107}$$

$$\mathbf{A_{ue} = A(1:nz, nz+1:n)} \qquad \text{n = full length of state vector} \tag{3-108}$$

$$\mathbf{S_{aCO2} = S_a(1:nz, 1:nz)} \tag{3-109}$$

$$\mathbf{S_{ae} = S_a(nz+1:n, nz+1:n)} \tag{3-110}$$

Finally, the variance components are

$$\sigma^2_m = \mathbf{h}^T \hat{\mathbf{S}}_\mathbf{m} \mathbf{h} \tag{3-111}$$

for measurement error,

$$\sigma^2_s = \mathbf{h}^T \hat{\mathbf{S}}_\mathbf{S} \mathbf{h} \tag{3-112}$$

for smoothing due to CO_2, and

$$\sigma^2_i = \mathbf{h}^T \hat{\mathbf{S}}_\mathbf{i} \mathbf{h} \tag{3-113}$$

for interference. These components of variance have the property that

$$\sigma^2_{XCO2} = \sigma^2_m + \sigma^2_s + \sigma^2_i \tag{3-114}$$

Table 3-5 Inverse Method Products Recorded with each Sounding

Name	Size	Comment
χ^2	3	Sum of squares of normalized residuals in each spectrometer
$\hat{\mathbf{x}}$	*n*	Retrieved State Vector
$\hat{\mathbf{S}}_{\mathbf{ii}}$	*n*	Diagonal elements of $\hat{\mathbf{S}}$ (error covariance matrix)
$\hat{\mathbf{S}}_{CO2}$	q^2	CO_2-only sub-matrix of $\hat{\mathbf{S}}$
$\tilde{\mathbf{s}}_1$	*n-q*	Correlation of X_{CO2} with non-CO_2 elements of **x**
$\mathbf{A_{CO2}}$	q^2	CO_2-only sub-matrix of averaging kernel (**A**)
$\mathbf{a_{CO2}}$	*n*	Column averaging kernel
$\tilde{\mathbf{a}}_\mathbf{c}$	*n*	Error in X_{CO2} due to smoothing and interference
X_{CO2}	1	Column-weighted CO_2 dry air mole fraction
σ^2_m	1	Variance of X_{CO2} due to measurement noise
σ^2_s	1	Variance of X_{CO2} due to smoothing

Name	Size	Comment
σ^2_i	1	Variance of X_{CO2} due to interference
σ^2_{XCO2}	1	Total Variance of X_{CO2} ($\sigma^2_m + \sigma^2_s + \sigma^2_i$)
d_f	1	Degrees of Freedom (full state vector)
d_{CO2}	1	Degrees of Freedom (CO_2 profile only)

4. References

Albert, S., A. Bauerecker, V. Boudon, L.R. Brown, J.-P. Champion, M. Loete, Nikitin, M. Quack (2009), Global Frequency and Intensity Analysis of $^{12}CH_4$ in the 0-4800 cm^{-1} region, *Chem. Phys. 356,* 131–146**.**

Allen, C.W. (1964), *Astrophysical Quantities*, Athlone Press (2nd ed.), London, 1964.

Anderson, P. W. (1949), Pressure Broadening in the Microwave and Infra-Red Regions, *Phys. Rev.*, vol. 76, Issue 5, pp. 647-661.

Babcock, H. D., and Herzberg, L. (1948), Fine structure of the red system of atmospheric oxygen bands, *Astrophys. J. 108*, 167-190.

Baranger, M. (1958), General Impact Theory of Pressure Broadening, *Phys. Rev.*, vol. 112, Issue 3, pp. 855-865.

Bates, D. R. (1984), Rayleigh scattering by air. *Planet. Space Sci.,* 32, 785–790.

Baum, B. A., A. J. Heymsfield, P. Yang, and S. T. Bedka (2005a), Bulk scattering properties for the remote sensing of ice clouds. Part I: Microphysical data and models, J. Appl. Meteorol., 44, 1885–1895.

Baum, B. A., P. Yang, A. J. Heymsfield, S. Platnick, M. D. King, Y.-X. Hu, and S. T. Bedka (2005b), Bulk scattering properties for the remote sensing of ice clouds. Part II: Narrowband models, J. Appl. Meteorol., 44, 1896–1911.

Benedetti, A., P. Gabriel, and G. L. Stephens (2002), Properties of reflected sunlight derived from a Green's function method. JQSRT2002; 72: 201-25.

Benner, D. C., V. M. Devi, E. Nugent, L. R. Brown, C. E. Miller, R. A. Toth, and K. Sung (2009), The 4850 cm^{-1} spectral region of CO_2: constrained multispectrum nonlinear least squares fitting including line mixing, speed dependent line profiles and Fermi resonance*, 64th Molecular Spectroscopy Symposium, Ohio State Univ.*

Bodhaine, B. A., N. B. Wood, E. G. Dutton, J. R. Slusser (1999), On Rayleigh Optical Depth Calculations. *J. Atmos. Oceanic Technol.,* 16, 1854–1861, doi: 10.1175/1520-0426.

Boesch, H., G.C. Toon, B. Sen, R.A. Washenfelder, P.O. Wennberg, M. Buchwitz, R. de Beek, J.P. Burrows, D. Crisp, M. Christi, B.J. Connor, V. Natraj, and Y.L. Yung (2006), Space-based near-infrared CO2 measurements: Testing the Orbiting Carbon Observatory retrieval algorithm and validation concept using SCIAMACHY observations over Park Falls, Wisconsin, *Journal of Geophysical Research-Atmospheres, 111* (D23).

Bonamy, L., and F. Emond (1995), Rotational-angular-momentum relaxation mechanisms in the energy-corrected-sudden scaling theory, *Phys. Rev. A*, 51, 1235–1240.

Brown, L. R., and C. Plymate (2000), Experimental line parameters of the Oxygen A band at 760 nm, *J. Mol. Spectrosc. 100*, 166-179.

Brown, L. R. (2005), Empirical Line Parameters of Methane from 1.1 to 2.1 μm, *J. Quant. Spectrosc. Radiat. Transfer 96*, 251-270.

Canadell, J. G., C. Le Que´re´, M. R. Raupach, C. B. Field, E. T. Buitenhuis, P. Ciais, T. J. Conway, N. P. Gillett, R. A. Houghton, and G. Marlandi (2007), "Contributions to accelerating atmospheric CO_2 growth from economic activity, carbon intensity, and efficiency of natural sinks," *PNAS*, 2007.

Chandrasekhar, S., (1950), *Radiative Transfer*. Oxford Univ. Press, Oxford.

Christi, M. J., and G. L. Stephens (2004), Retrieving profiles of atmospheric CO_2 in clear sky and in the presence of thin cloud using spectroscopy from the near and thermal infrared: A preliminary case study, *J. Geophys. Res.*, 109, D04316, doi: 10.1029/2003JD004058.

Chylek, P., and G. Videen (1994), Longwave radiative properties of polydispersed hexagonal ice crystals, *J. Atmos. Sci.*, 51(2), 175–190.

Connor B. J., H. Boesch, G. Toon, B. Sen, C. Miller and D. Crisp (2008), Orbiting Carbon Observatory: Inverse method and prospective error analysis, *J. Geophys. Res*., 113, D05305, doi:10.1029/2006JD008336.

Corey, G. C., and F. R. McCourt (1984), Infinite-order sudden calculations of pressure broadening cross sections for noble gas-oxygen binary mixtures, *J. Chem. Phys.*, 81, 3892–3907.

Cox, C. and W. Munk (1954), Measurement of the roughness of the sea surface from photographs of the sun's glitter, *J. Opt. Soc. Am.*, **44**, 838-850.

Crisp, D., R.M. Atlas, F.-M. Breon, L.R. Brown, J.P. Burrows, P. Ciais, B.J. Connor, S.C. Doney, I.Y. Fung, D.J. Jacob, C.E. Miller, D. O'Brien, S. Pawson, J.T. Randerson, P. Rayner, R.J. Salawitch, S.P. Sander, B. Sen, G.L. Stephens, P.P. Tans, G.C. Toon, P.O. Wennberg, S.C. Wofsy, Y.L. Yung, Z. Kuang, B. Chudasama, G. Sprague, B. Weiss, R. Pollock, D. Kenyon, S. Schroll (2004), "The Orbiting Carbon Observatory (OCO) mission" *Advances in Space Research* 34, 700–709.

Crisp, D., C. E. Miller, and P. L. DeCola (2007), "NASA Orbiting Carbon Observatory: Measuring the column averaged carbon dioxide mole fraction from space," *JARS*, 12/1/2007.

Crisp, D. (2008), "The Orbiting Carbon Observatory: NASA's First Dedicated Carbon Dioxide Mission," *Proc. SPIE*, *7106*, DOI: 10.1117/12.802194.

De Pristo, A. E., S. D. Augustin, R. Ramaswamy, and H. Rabitz (1979), Quantum number and energy scaling for nonreactive collisions, *J. Chem. Phys.,* 71, 850– 865.

de Rooij, W. A., and C. C. A. H. van der Stap (1984), Expansion of Mie scattering matrices in generalized spherical functions, *Astron. Astrophys.*, 131, 237–248.

Devi, V. M., D. C. Benner, L. R. Brown, C. E. Miller, and R. A. Toth (2007a), Line mixing and speed dependence in CO_2 at 6348 cm^{-1}: Constrained multispectrum analysis of intensities and line shapes in the 30012 ← 00001 band, *J. Mol. Spectrosc. 242*, 90-117.

Devi, V. M., D. C. Benner, L. R. Brown, C. E. Miller, and R. A. Toth (2007b), Line mixing and speed dependence in CO_2 at 6227.9 cm^{-1}: Constrained multispectrum analysis of intensities and line shapes in the 30013 ← 00001 band, *J. Mol. Spectrosc. 245*, 52-80.

Dudhia, Anu (2009), RFM Software package and user guide available at http://www.atm.ox.ac.uk/RFM/

Dufour, E. and F.-M. Bréon, (2003), "Spaceborne Estimate of Atmospheric CO_2 Column by Use of the Differential Absorption Method: Error Analysis," *Appl. Opt.* **42**, 3595-3609.

Draine, B. T. (1988), The discrete-dipole approximation and its application to interstellar graphite grains, *Astrophys. J.*, *333,* 848–872.

Edmonds, A. R. (1974), Angular Momentum in Quantum Mechanics, edited by R. Hofstadter, Princeton Univ. Press, Princeton, N. J.

Falke, S., E. Tiemann, C. Lisdat, H. Schnatz, and G. Grosche (2006), Transition frequencies of the D lines of K-39, K-40, and K-41 measured with a femtosecond laser frequency comb, *Phys. Rev. A 74*, DOI: 10.1103/PhysRevA.74.032503.

Fanjoux, G., R. Millet, R. Saint-Loup, and R. Chaux (1994), Coherent anti-Stokes Raman spectroscopy study of collisional broadening in the O_2-H_2O Q branch, *J. Chem. Phys. 101*, 1061-1071.

Frankenberg, C., T. Warneke, A. Butz, I. Aben, F. Hase, P. Spietz, and L. R. Brown (2008), Methane spectroscopy in the near infrared and it simplification on atmospheric retrievals, *Atmos. Chem. Phys. 8*, 5061-5075.

Gabriel P., M. Christi, and G.L. Stephens (2006), Calculation of Jacobians for Inverse Radiative Transfer: An Efficient Hybrid Method. *Journal of Quantitative Spectroscopy & Radiative Transfer*, **97** (2):209, 2006.

Galatry, L. (1961), Simultaneous effect of Doppler and foreign gas broadening on spectral lines, *Phys. Rev.*, *122*, 1218-1223.

Geller, M. A. (1992), high-resolution atlas of the infrared spectrum of the sun and the earth atmosphere from space, Volume III Key to identification of solar features, NASA Reference Publication 1224, 1992.

Hansen, J.E., and L.D. Travis (1974), Light Scattering in Planetary Atmospheres, *Space Science Reviews*, **16***,* 527-610.

Hartmann, J.-M., C. Boulet, and D. Robert (2008), Collisional Effects on Molecular Spectra: Laboratory experiments and models, consequences for applications,edited by Elsevier Science Ltd.

Hartmann, J.-M., H. Tran, and G. Toon (2009), Influence of line mixing on the retrievals of atmospheric CO_2 from spectra in the 1.6 and 2.1 μm regions, *Atmos. Chem. Phys. Disc.9,*, 4873-4898.

Heidinger A.K., and G. L. Stephens (2000), Molecular line absorption in a scattering atmosphere: II Application to remote sensing in the O2 A-band. *J. Atmos. Sci*.,57, 1615-1634.

Ishimaru, A. (1991), *Electromagnetic Wave Propagation, Radiation, and Scattering*, Englewood Cliffs: Prentice Hall.

Jenouvrier A., L. Daumont, L. Regalia-Jarlot, V. G. Tyuterev, M. Carleer, A. C. Vandaele, S. Mikhailenko, and S. Fally (2007), Fourier transform measurements of water vapor line parameters in the 4200–6600 cm^{-1} region, *J. Quant. Spectrosc. Radiat. Transfer 105*, 326–355.

Kahn, R., P. Banerjee, and D. McDonald (2001), Sensitivity of multiangle imaging to natural mixtures of aerosols over ocean, *J. Geophys. Res.*, 106 (D16), 18,219–18,238.

Kawabata, K., and S. Ueno (1988), The first three orders of scattering in vertically inhomogeneous scattering–absorbing media, *Astrophys. Space Sci.*, 150(2), 327–344.

A. Levy, N. Lacome and C. Chackerian, Jr. (1992), Chapter V, Collisional Line Mixing, in *Spectroscopy of the Earth's Atmosphere and Interstellar Molecules* (K. Narahari Rao and A. Weber, Eds.) Academic Press Inc. pp 261-337.

Lyulin, O. M., A. V. Nikitin, V. I. Perevalov, I. Morino, T. Yokota, R. Kumazawa, and T. Watanabe (2009), Measurements of N_2- and O_2-broadening and -shifting parameters of the methane spectral lines in the 5550-6236 cm^{-1} region, *J. Quant. Spectrosc. Radiat. Transfer 110*, 654-668.

Lyulin, O. M., S. Kassi, K. Sung, L.R. Brown and A. Campargue (2010), Determination of the low energy values of $^{13}CH_4$ transitions in the $2\nu_3$ region near 1.66 μm from absorption spectra at 296 and 81 K, *Journal of Molecular Spectroscopy Volume 261, Issue 2*, June 2010, p. 91-100.

Maignan F., F.M. Bréon, and R. Lacaze (2004), Bidirectional reflectance of Earth targets: Analytical modeling and validation against a large data set of satellite observations. *Rem. Sens. Env.,* 90, 210-220.

Miller, C.E., and L. R. Brown (2004a), Near Infrared Spectroscopy of Carbon Dioxide: $^{16}O^{12}C^{16}O$ Line Positions, *J. Mol. Spectrosc. 228*, 329-354.

Miller, C. E., M. A. Montgomery, R. M. Onorato, C. Johnstone, T. P. McNicholas, B. Kovaric and L. R. Brown (2004b), Near Infrared Spectroscopy of Carbon Dioxide. II. $^{16}O^{13}C^{16}O$ and $^{16}O^{13}C^{18}O$ Line Positions, *J. Mol. Spectrosc. 228*, 355-374.

Miller, C. E., L. R. Brown, R. A. Toth D. C. Benner, and V. M. Devi (2005), Spectroscopic challenges for high accuracy retrievals of atmospheric CO_2 and the Orbiting Carbon Observatory (OCO) experiment, *Comptes Rendus Physique 6*, 876-887.

Miller, C. E., D. Crisp, P. L. DeCola, S. C. Olsen, J. T. Randerson, A. M. Michalak,A. Alkhaled, P. Rayner, D. J. Jacob, P. Suntharalingam, D. B. A. Jones, A. S. Denning, M. E. Nicholls, S. C. Doney, S. Pawson, H. Boesch, B. J. Connor, I. Y. Fung, D. O'Brien, R. J. Salawitch, S. P. Sander, B. Sen, P. Tans, G. C. Toon, P. O. Wennberg, S. C. Wofsy, Y. L. Yung, and R. M. Law (2007), "Precision requirements for space-based X_{CO2} data", *J. Geophys. Res.* 112, D10314, [doi:10.1029/2006JD007659].

Mishchenko, M. I. (1991), Light scattering by randomly oriented axially symmetric particles, *J. Opt. Soc. Am. A*, 8(6), 871–882.

Mishchenko, M. I., and L. D. Travis (1998), Capabilities and limitations of a current FORTRAN implementation of the T-matrix method for randomly oriented, rotationally symmetric scatterers, *J. Quant. Spectrosc. Radiat. Transfer*, 60(3), 309–324.

Mishchenko, M. I., L. D. Travis, R. A. Kahn, and R. A. West (1997), Modeling phase functions for dustlike tropospheric aerosols using a shape mixture of randomly oriented polydisperse spheroids, *J. Geophys. Res.*, 102(D14), 16,831–16,847.

Natraj, V., and R. J. D. Spurr (2007), A fast linearized pseudo-spherical two orders of scattering model to account for polarization in vertically inhomogeneous scattering–absorbing media, *J. Quant. Spectrosc. Rad. Tran.*, 107, 263–293.

Natraj, V., H. Boesch, R. J. D. Spurr, and Y. L. Yung (2008), Retrieval of X_{CO2} from simulated Orbiting Carbon Observatory measurements using the fast linearized R-2OS radiative transfer model, *J. Geophys. Res.*, 113, D11212, doi:10.1029/2007JD009017.

Niro, F., T. von Clarmann, K. Jucks, and J.-M. Hartmann (2005a), Spectra calculations in central and wing regions of CO_2 IR bands between 10 and 20 m. III: atmospheric emission Spectra, J. *Quant. Spectrosc. Radiat. Transfer 90*, 61–76.

Niro, F., K. Jucks, and J.-M. Hartmann (2005b), Spectra calculations in central and wing regions of CO2 IR bands. IV: software and database for the computation of atmospheric spectra, *J. Quant. Spectrosc. & Radiat. Transfer* 95, 469–481.

O'Brien, D. M. and R. M. Mitchell (1992), "Error estimates for retrieval of cloud-top pressure using absorption in the A band of oxygen," *J. of Applied Meteorology*, Vol 31, Isssue 10 (October 1992) pp. 1179–1192 DOI: 10.1175/1520-0450.

Palmer, K. F. and D. Williams (1975), "Optical Constants of Sulfuric Acid; Application to the Clouds of Venus?," *Appl. Opt.* 14, 208-219, doi:10.1364/AO.14.000208.

Predoi-Cross, A., W. Liu, C. Holladay, A.V. Unni, I. Schofield, A. R. W. McKellar, and D. Hurtmans (2007). Line profile study of transitions in the 30012 ← 00001 and 30013 ← 00001 bands of carbon dioxide perturbed by air, *J. Mol. Spectrosc. 246*, 98-112.

Predoi-Cross, A., K. Hambrook, R. Keller, C. Povey, I. Schofield, D. Hurtmans, H. Over, and G. Ch. Mellau (2008a), Spectroscopic lineshape study of the self-perturbed oxygen A-band, *J. Mol. Spectrosc. 248*, 85-110.

Predoi-Cross, A., C. Holladay, H. Heung, J.-P. Bouanich, G. Ch. Mellau, R. Keller, and D. R. Hurtmans (2008b*)*, Nitrogen-broadened lineshapes in the oxygen A-band: Experimental results and theoretical calculations, *J. Mol. Spectrosc. 251,* 159–175.

Predoi-Cross, A., A.R.W. McKellar, D. C. Benner, V. M. Devi, R. R. Gamache, C. E. Miller , R. A. Toth and L. R. Brown (2009), Temperature dependences for air-broadened Lorentz half width and pressure-shift coefficients in the 30013←00001 and 30012←00001 bands of CO_2 near 1600 nm, *Can. J. Phys. (in press).*

Purcell, E. M., and C. R. Pennypacker (1973), Scattering and absorption of light by non-spherical dielectric grains, *Astrophys. J.*, 186, 705–714.

Rayner, P. J. and D. M. O'Brien (2001), "The utility of remotely sensed CO_2 concentration data in surface source inversions," *Geophys. Res. Lett.,* **28***,* 175-178.

Ritter, K. J. (1986). A High-Resolution Spectroscopic Study of Absorption Line Profiles in the A-band of Molecular Oxygen, University of Maryland.

Robichaud, D. J., J. T. Hodges, L. R. Brown, D. Lisak, M. Okumura, and C. E. Miller (2008a), Experimental Intensity and Line Shape Parameters of the Oxygen A-Band Using Frequency-Stabilized Cavity Ring-Down Spectroscopy, *J. Mol. Spectrosc. 248*, 1-13.

Robichaud, D. J., J. T. Hodges, P. Masłowski, L. Y. Yeung, M. Okumura, C. E. Miller, and L. R. Brown (2008b), High-Accuracy Transition Frequencies for the O_2 A-Band, *J. Mol. Spectrosc. 251*, 27-43.

Robichaud, D. J., L. Y. Yeung, D. A. Long, D. K. Havey, J. T. Hodges, M. Okumura, C. E. Miller, and L. R. Brown (2009), Experimental Line Parameters of the $b^1\Sigma_g^+ \leftarrow X^3\Sigma_g^-$ Band of Oxygen Isotopologues at 760 nm Using Frequency-Stabilized Cavity Ring-Down Spectroscopy, *J. Phys. Chem. A,* 2009, *113* (47), pp 13089–13099, doi: 10.1021/jp901127h.

Rodgers, C. (2000) *Inverse Methods for Atmospheric Sounding: Theory and Practice*. World Scientific Publishing Co Pte Ltd.

Rodgers, C. D., and B. J. Connor (2003), Intercomparison of remote sounding instruments, *J. Geophys. Res.*, 108(D3), 4116, doi:10.1029/2002JD002299.

Rodrigues, R., C. Boulet, L. Bonamy, and J. M. Hartmann (1998), Temperature, pressure, and perturber dependencies of line-mixing effects in CO_2 infrared spectra. II. Rotational angular momentum relaxation and spectral shift in $\Sigma \leftarrow \Sigma$ bands, *J. Chem. Phys*., 109, 3037–3047.

Rosenkranz, P. W. (1975), Shape of 5 mm oxygen band in atmosphere, *IEEE Trans. Ant. Prop. AP23*, 498-506.

Rothman, L.S., D. Jacquermart, A. Barbe, D. C. Benner, M. Birk, L. R. Brown, M. R. Carleer, C. Chackerian, Jr., K. Chance, V. Dana, V. M. Devi, J.-M. Flaud, R. R. Gamache, A. Goldman, J. -M. Hartmann, K. W. Jucks, A. G. Maki, J.-Y. Mandin, S. T. Massie, J. Orphal, A. Perrin, C. P. Rinsland, M. A. H. Smith, J. Tennyson, R. N. Tolchenov, R. A. Toth, J. V. Auwera, P. Varanasi, and G. Wagner (2005), The HITRAN 2004 molecular spectroscopic database, *J. Quant. Spectrosc. Radiat. Transfer 96*, 139-204.

Rothman L. S., I. E. Gordon, A. Barbe, D. C. Benner, P. F. Bernath, M. Birk, V. Boudon, L. R. Brown, A. Campargue, J.-P. Champion, K. Chance, L. H. Coudert, V. Dana, V. M. Devi, S. Fally, J.-M. Flaud, R. R. Gamache, A. Goldman, D. Jacquemart, I. Kleiner, N. Lacome, W. J. Lafferty, J.-Y. Mandin, S. T. Massie, S. Mikhailenko, C. E. Miller, N. Moazzen-Ahmadi, O. V. Naumenko, A. Nikitin, J. Orphal, A. Predoi-Cross, V. Perevalov, A. Perrin, C. P. Rinsland, M. Rotger, M. Šimečková, M. A. H. Smith, K. Sung, S. Tashkun, J. Tennyson, R. A. Toth, A. C. Vandaele, and J. Vander Auwera (2009), The HITRAN 2008 molecular spectroscopic database, *J. Quant. Spectrosc. Radiat. Transfer 110*,533-572.

Roujean J. L., D. Tanré, F. M. Bréon, and J. L. Deuzé (1997), Retrieval of land surface parameters from airborne POLDER bidirectional reflectance distribution function during HAPEX-Sahel. *J. Geophys. Res.*, **102**, 11201–11218.

Shettle, E. P., and R. W. Fenn (1979), Models for the aerosols of the lower atmosphere and the effects of humidity variations on their optical properties, AFGL-TR-79-0214, Air Force Geophys. Lab., Hanscom Air Force Base, Mass.

Siewert, C. E. (1982), On the phase matrix basic to the scattering of polarized light, Astron. Astrophys., 109, 195–200.

Šimečková, Marie, David Jacquemart, Laurence S. Rothman, Robert R. Gamache and Aaron Goldman (2006), Einstein A-coefficients and statistical weights for molecular absorption transitions in the HITRAN database. Journal of Quantitative Spectroscopy and Radiative Transfer, Volume 98, Issue 1, March 2006, Pages 130-155.

Spurr, R. J. D., T.P. Kurosu, and K.V. Chance (2001), A linearized discrete ordinate radiative transfer model for atmospheric remote-sensing retrieval, *J. Quant. Spectrosc. Rad. Tran.*, 68(6), 689–735.

Spurr, R. J. D. (2002), Simultaneous derivation of intensities and weighting functions in a general pseudo-spherical discrete ordinate radiative transfer treatment, *J. Quant. Spectrosc. Rad. Tran.*, 75(2), 129–175.

Spurr, R. J. D. (2006), VLIDORT: a linearized pseudo-spherical vector discrete ordinate radiative transfer code for forward model and retrieval studies in multilayer multiple scattering media, *J. Quant. Spectrosc. Rad. Tran.*, 102(2), 316–342.

Spurr, R. J. D., and M. J. Christi (2007), Linearization of the interaction principle: Analytic Jacobians in the "Radiant" model, *J. Quant. Spectrosc. Rad. Tran.*, 103 (3), 431–446.

Sung, K., L. R. Brown, R. A. Toth, and T. J. Crawford (2009), FT-IR measurements of H_2O-broadened half-widths of CO_2 at 4.3 μm, *Can. J. Phys.* (in press).

Takano, Y., and K.-N. Liou (1989), Solar radiative transfer in cirrus clouds. Part I: Single-scattering and optical properties of hexagonal ice crystals, *J. Atmos. Sci.*, 46(1), 3–19.

Tennyson, J., P. F. Bernath, L. R. Brown, A. Campargue, M. R. Carleer, A. G. Csasza, R. R. Gamache, J. T. Hodges, A. Jenouvrier, O. V. Naumenko, O. L. Polyansky, L. S. Rothman, R. A. Toth, A. C. Vandale, N. F. Zobov, L. Daumont, A. Z. Fazliev, T. Furtenbacher, I. E. Gordon, S. N. Mikhailenko, and S. V. Shirin (2009), IUPAC critical evaluation of the rotational–vibrational spectra of water vapor. Part I—Energy levels and transition wavenumbers for $H_2{}^{17}O$ and $H_2{}^{18}O$, *J. Quant. Spectrosc. Rad. Tran., 110*,573-596.

Thuillier, G., M. Hersé, P. C. Simon, D. Labs, H. Mandel, D. Gillotay, and T. Foujols (2003), "The solar spectral irradiance from 200 to 2400 nm as measured by the SOLSPEC spectrometer from the ATLAS 1-2-3 and EURECA missions, Solar Physics, 214(1): 1-22.

Toon, G.C., J.-F. Blavier, B. Sen, R.J. Salawitch, G.B. Osterman, J. Notholt, M. Rex, C.T. McElroy, and J.M. Russell III (1999), Ground-based observations of Arctic O_3 loss during spring and summer 1997, *J. Geophys. Res., 104(D21),* 26497-26510.

Toth, R. A., L. R. Brown, C. E. Miller, V. M. Devi, and D. C. Benner (2006a), Line strengths of $^{12}C^{16}O_2$: 4550-7000 cm^{-1}, *J. Mol. Spectrosc. 239*, 221-242.

Toth, R. A., L.R. Brown, C.E. Miller, V. M. Devi, and D. C. Benner (2006b), Self-broadened widths and shifts of CO_2, *J. Mol. Spectrosc. 239*, 243-271.

Toth, R. A., C. E. Miller, L. R. Brown, V. M. Devi, and D. C. Benner (2007a), Line positions and strengths of $^{16}O^{12}C^{18}O$, $^{18}O^{12}C^{18}O$ and $^{17}O^{12}C^{18}O$ between 2200 and 7000 cm^{-1}, *J. Mol. Spectrosc. 243*, 43-61.

Toth, R. A., C. E. Miller, V. M. Devi, D. C. Benner, and L. R. Brown (2007b), Air-broadened width and pressure shift coefficients of $^{12}C^{16}O_2$: 4700 – 7000 cm^{-1}, *J. Mol. Spectrosc. 246*, 133-157.

Toth, R. A., C. E. Miller, L. R. Brown, V. M. Devi, and D. C. Benner (2008a), Line strengths of $^{16}O^{13}C^{16}O$, $^{16}O^{13}C^{18}O$, $^{16}O^{13}C^{17}O$ and $^{18}O^{13}C^{18}O$ between 2200 and 6800 cm^{-1}, *J. Mol. Spectrosc. 251*, 64-89.

Toth, R. A., L. R. Brown, C. E. Miller, V. M. Devi, and D. C. Benner (2008b), Spectroscopic database of CO_2 line parameters: 4300 – 7000 cm^{-1}, *J. Quant. Spectrosc. Radiat. Transfer 109*, 906-921.

Tran, H., C. Boulet, and J.-M. Hartmann (2006), Line mixing and collision-induced absorption by oxygen in the A band: Laboratory measurements, model, and tools for atmospheric spectra computations, *J. Geophys. Res. 111*, D15210, doi:10.1029/ 2005JD006869.

Tran, H., and J.-M. Hartmann (2008), An improved O_2 A band absorption model and its consequences for retrievals of photon paths and surface pressures, *J. Geophys. Res.113*, D18104, doi:10.1029/2008JD010011.

van de Hulst, H. C. (1957), *Light Scattering by Small Particles*, New York: John Wiley.

Van Flandern, T. C. and K. F. Pulkkinen (1979) "Low precision formulae for planetary positions", *ApJ Supp*. 41, 391-411.

Washenfelder , R. A., P. O. Wennberg and G. C. Toon (2003), Tropospheric methane retrieved from ground-based near-IR solar absorption spectra, *Geophys. Res. Lett.*, 30 (23): art. no. 2226 DEC 13, 2003.

Washenfelder, R. A., G. C. Toon, J.-F. Blavier, Z. Yang, N. T. Allen, P. O. Wennberg, S. A. Vay, D. M. Matross and B. C. Daube (2006), Carbon dioxide column abundances at the Wisconsin Tall Tower site*, J. Geophys. Res. 111*, D22305, doi:10.1029/2006JD007154.

World Climate Research Programme (1986), A preliminary cloudless standard atmosphere for radiation computation, Rep. WCP-112, World Meteorol. Organ., Geneva, Switzerland.

Wunch, D. , G. C. Toon, P. O. Wennberg, S. C. Wofsy, B. B. Stephens, M. L. Fischer, O. Uchino, J. B. Abshire, P. Bernath, S. C. Biraud, J.-F. L. Blavier, C. Boone, K. P. Bowman, E. V. Browell, T. Campos, B. J. Connor, B. C. Daube, N. M. Deutscher, M. Diao, J. W. Elkins, C. Gerbig, E. Gottlieb, D. W. T. Griffith, D. F. Hurst, R. Jim´enez, G. Keppel-Aleks, E. Kort, R. Macatangay, T. Machida, H. Matsueda, F. Moore, I. Morino, S. Park, J. Robinson, C. M. Roehl, Y. Sawa, V. Sherlock, C. Sweeney, T. Tanaka, and M. A. Zondlo, (2010), "Calibration of the total carbon column observing network using aircraft profile data," Atmos. Meas. Tech. Discuss., 3, 2603–2632, doi:10.5194/amtd-3-2603-2010.

Yang, Z., G. C. Toon, J. S. Margolis and P. O. Wennberg (2002), Atmospheric CO_2 retrieved from ground-based near IR spectra, *Geophys. Res. Lett., 29(9),* doi:10.1029/2001GL014537.

Yang, Z., P. O. Wennberg, R. P. Cageao, T. J. Pongetti, G. C. Toon, and S. P. Sander (2005), Ground-based photon path measurements from solar absorption spectra of the O_2 A-band*, J. Quant. Spectrosc. Radiat. Transfer 90,* 309–321.

Young, A.T. (1980), Revised depolarization corrections for atmospheric extinction, *Applied Optics*, **19** (20), 3427-3428.

Appendices

A. Acronyms

ABSCO	Absorption Coefficients
ACS	Attitude Control System
AIRS	Atmospheric Infrared Sounder
AOD	Aerosol Optical Depth
AOPD	Apparent Optical Path Differences
ATB	Algorithm Theoretical Basis
AU	Astronomical Unit
BRDF	Bidirectional Reflectance Distribution Function
CALIPSO	Cloud-Aerosol Lidar and Infrared Pathfinder Satellite Observation
CIA	Collision Induced Absorption
CO	Carbon Monoxide
CO_2	Carbon Dioxide
CPU	Central Processing Unit
CRDS	Cavity Ringdown Spectrometer
DEM	Digital Elevation Model
ECMWF	European Center for Medium Range Weather Forecasting
EOS	Earth Observing System
FOV	Field of View
FP	Full Physics
FPA	Focal Plain Array
FTS	Fourier Transform Spectrometer
FWHM	Full-Width at Half Maximum
GPS	Global Positioning System
H_2O	Water
HWHM	Half-Widths at the Half Maximum
HgCdTe	Mercury Cadmium Telluride
HDF	Hierarchical Data Format
ILS	Instrument Line Shape
km	kilometer

LIDORT	Linearized Discrete Ordinate Radiative Transfer
LISA	Laboratoire Interuniversitaire des Systèmes Atmospheriques (France)
LMDZ	Laboratoire de Météorologie Dynamique general circulation model
LT	Local Time
MLT	Mean Local Time
NASA	National Aeronautics and Space Administration
NIR	Near Infrared
NIST	National Institute of Standards and Technology (Maryland)
NRC	National Research Center (Canada)
O_2	Oxygen
O_3	Ozone
OBC	On-Board Calibrator
OCO	Orbiting Carbon Observatory
ppm	parts per million
RT	Radiative Transfer
RTE	Radiative Transfer Equation
SNR	Signal-to-Noise Ratio
TCCON	Total Carbon Column Observing Network
TES	Tropospheric Emission Spectrometer
TOA	Top of Atmosphere
VLIDORT	Vector LIDORT
VMR	Volume Mix Ratio
WMO	World Meteorological Organization
WRS	World Reference System